OPTICAL ASTROMETRY AND ORBIT DETERMINATION

A Dissertation

Submitted to the Faculty

of

Purdue University

by

Patrick M. Kelly

In Partial Fulfillment of the

Requirements for the Degree

of

Masters of Science in Aeronautics and Astronautics

May 2020

Purdue University

West Lafayette, Indiana

THE PURDUE UNIVERSITY GRADUATE SCHOOL
STATEMENT OF DISSERTATION APPROVAL

Dr. Carolin Frueh, Chair

School of Aeronautics and Astronautics

Dr. Kathleen Howell

School of Aeronautics and Astronautics

Dr. James Garrison

School of Aeronautics and Astronautics

Approved by:

Dr. Gregory Blaisdell

Associate Head of Gambaro Graduate Program of Aeronautics and Astronautics

ACKNOWLEDGMENTS

I would like to thank my advisor, Dr. Carolin Frueh for her support since embarking upon this journey. I have benefited considerably from her commitment to her students and the work that they conduct. Without her guidance this work would not have been possible. I would also like to thank the members of my committee, Professor Kathleen Howell and Professor James Garrison, both of which have provided valuable insight into my work. Additionally, I would like to thank the exceptional faculty of the School of Aeronautics and Astronautics, who have helped me develop as an Aerospace Engineer.

Lastly, I would like to extend my sincerest appreciation to my friends and family who have been a continued source of happiness and support throughout my life. For this, I am forever grateful.

TABLE OF CONTENTS

LIST OF TABLES

Table Page

LIST OF FIGURES

Figure Page

SYMBOLS

$\oplus$	Earth
$\mathbb{C}$	Moon
μ	Gravitational Parameter ($\mu_\oplus = 398{,}600.4415\ km^3/s^2$)
$r_\oplus$	Earth Radius ($6378.137\ km$)
φ	Geodedic Latitude
λ	Geodedic Longitude
α	Right Ascension
δ	Declination
A	Azimuth Angle
E	Elevation Angle

ABBREVIATIONS

SSA	Space Situational Awareness
RSO	Resident Space Object
POGS	Purdue Optical Ground Station
TLE	Two-Line Element
IERS	International Earth Rotation and Reference Systems Service
ICRS	International Celestial Reference System
ITRS	International Terrestrial Reference System
ICRF	International Celestial Reference Frame
ITRF	International Terrestrial Reference Frame
ECI	Earth Centered Inertial
ECEF	Earth Centered Earth Fixed
LUMVE	Linear Unbiased Minimum Variance Estimate
GPS	Global Positioning System
IGS	International GNSS Service

ABSTRACT

Kelly, Patrick M. M.S., Purdue University, May 2020. Optical Astrometry and Orbit Determination. Major Professor: Carolin Frueh.

The resident space object population in the near-Earth vicinity has steadily increased since the dawn of the space age. This population is expected to increase drastically in the near future as the realization of proposed mega-constellations is already underway. The resultant congestion in near-Earth space necessitates the availability of more complete and more accurate satellite tracking information to ensure the continued sustainable use of this environment. This work sets out to create an operational system for the delivery of accurate satellite tracking information by means of optical observation. The state estimates resulting from observation series conducted on a GPS satellite and a geostationary satellite are presented and compared to existing catalog information. The satellite state estimate produced by the system is shown to outperform existing two-line element results. Additionally, the statistical information provided by the processing pipeline is evaluated and found to be representative of the best information available for the satellites true state.

1. INTRODUCTION

Space situational awareness (SSA) has several definitions and may encompass a variety of higher-level objectives [1]. The United States Joint Chiefs of Staff defined SSA in a Joint Publication covering Space Operations as the following:

> *SSA is the requisite foundational, current, and predictive knowledge and characterization of space objects and the OE* [Operational Environment] *upon which space operations depend – including physical, virtual, information and human dimensions – as well as all factors, activities, and events of all entities conducting, or preparing to conduct, space operations* [2].

This definition provides coverage over all of the potential factors that affect the primary goal of SSA: to provide the information necessary for the sustainable use of Near-Earth space. As of this date, United States Strategic Command (USSTRATCOM) tracks a total of 20,598 Earth orbiting satellites of size < 10 cm in LEO and < 1 m in GEO, but even in these size ranges the catalog is incomplete [3, 4]. This only makes up a fraction of the total number of objects in near Earth space, as the estimated number of debris objects of size greater than 1 cm is 900,000 [5]. The population of Earth orbiting satellites is expected to increase significantly in the near future as multiple proposed mega-constellations have entered the early stages of implementation. The projected increase in satellite population poses a significant threat to the space-faring community and necessitates the development of a high-fidelity SSA framework [6, 7].

The aforementioned catalog of resident space objects maintained by USSTRATCOM is a vital asset to the SSA community, but has limitations. Catalog entries are created through observations made by the United States Space Surveillance Network

(SSN) which is composed of 29 sensors distributed worldwide. This network has a limited capacity for observation, which creates problems as far as how to best allocate these finite resources [8, 9]. This limited capacity directly affects the number of maintained objects in the catalog and the regularity with which the objects can be observed. The catalog entries are accessible in two-line element (TLE) format through an online API [3]. In addition to systemic error produced by measurement noise, the orbit determination step, and modeling inconsistencies, this delivery method has a finite amount of significant digits, causing a noticeable truncation error. Additionally, this format does not provide any statistical information or measure of certainty in the provided data. For this reason, the user is blind to any resulting error in the TLE solution, which can be significant when compared to external sources of state information [10]. For this reason, supplemental information to improve the quality of the catalog is necessary to ensure a sustainable future for the use of near-Earth space.

Ground based optical observation has been a means of astronomical data collection for hundreds of years. Telescopes are used to collect light from sources, either active or passively illuminated, which is then focused and magnified for viewing [11]. Historically, the capacity for observation was limited by the capability of the human eye. The Charge-Coupled-Device (CCD) has played a pivotal role in the advancement of optical astronomy over the past four and a half decades since their introduction to the field [12]. These devices allow users to make accurate measurements of extremely faint objects [13, 14]. Using these optical instruments, observations of resident space objects can be performed, either with $a-priori$ position information (follow-up observation), or without. In the presence of $a-priori$ information, one can incorporate the new measurements to improve the information through multiple means, one such example being extended Kalman Filter. When new objects are detected, a number of observations must be performed, followed by an observation association procedure. This procedure allows the user to determine the likelihood that multiple obtained observations are in fact observations of the same object [15]. Once the association step

is complete, the observations can be used to produce angular measurements, which are then used to conduct the orbit determination procedure [4].

Processing pipelines for acquiring SSA information using optical sensors have seen considerable research, much of which has gone unpublished. Some resources do exist for systems such as the ESA Space Debris Telescope [16] and the International Scientific Optical Network (ISON) [17], but the developments are in most cases specific to the indicated systems. Tools for individual components of the processing pipeline do exist, but not for the whole system. In particular, there exist several tools for plate solving [18], however their application to the processing of satellite observations is often limited due to their focus on applications in astronomy. These tools are a blackbox that rarely provide turn-key capability for the production of satellite measurements. For this reason the development of an independent processing pipeline that works with the telescope and observations made at the Purdue Optical Ground Station (POGS) is sought.

This work sets out to create an operational system to deliver accurate SSA information through the use of optical observations. Namely, the full state and associated statistical information of an observed RSO is sought; addressing the needs of the SSA community in light of an ever growing satellite population. This system is realized through the processing of images taken at the Purdue Optical Ground Station, an optical observatory located in Mayhill, NM operated remotely from West Lafayette, IN. Astrometric measurements of satellites are extracted from observation campaigns to produce the desired state estimates. The questions to be addressed by this work are:

- How does the user go about processing images collected at the Purdue Optical Ground Station in order to detect resident space objects?
- How can these images be used to provide precise astrometric measurements of resident space objects?

- Can these measurements be used to produce a reasonably accurate orbit determination solution?
- How does the information provided by the system compare to the publicly available TLE catalog?

The organization of this thesis is as follows. Chapter 2 provides pertinent background material for the understanding of operation in the space environment. The fundamental dynamics governing the motion of spacecraft in the near Earth vicinity are derived. The definition and realization of fundamental reference frames and the role that time plays in them is provided. Classical and contemporary means by which the orbit determination process is conducted are fully derived and all tools necessary for their implementation are provided. To conclude, all of this material is applied comprehensively in a simulated observation scenario of two satellites taken from the TLE catalog.

Chapter 3 provides an overview of optical sensors and how they can be utilized for astronomic observations of spacecraft. This includes full coverage of the hardware being used at the Purdue Optical Ground Station, and some of the expected system parameters that will be used later. Additionally, the operation of the telescope and how observations of a specified satellite can be scheduled are covered.

Chapter 4 covers the image processing algorithms implemented in the processing pipeline. This includes how to detect, position, and classify objects in the image. Objects are classified as stars or potential objects of interest (satellite candidates). This step is essential in the processing pipeline as it extracts usable information from the raw images.

Chapter 5 covers the astrometry and plate solving algorithms developed for the processing pipeline. The primary goal of this step is to take extracted data from the image processing step and transform it to astrometric measurements. This includes a full description of star catalogs used, how a transformation from image coordinates

to astronomical coordinates can be realized, and how to find the best fit for this transformation given observed patterns in the star field of the image.

Chapter 6 presents the results produced by the processing pipelines for observation series conducted for the GPS satellite Navstar 76, and the geostationary satellite Amazonas 3. Results are compared to the best true state information available for each object as well as the TLE solution. The three questions posed above are addressed directly in this chapter.

2. BACKGROUND

2.1 The Two-Body Problem

The two-body problem and its solution are fundamental to understanding the motion of celestial objects; both natural and human-made. The problem formulation is a specific case of the more general N-body problem, which studies the gravitational interaction and subsequent motion of a system of N particles. The two-body problem ($N = 2$) happens to be the only case that presently has a complete solution. References [19–21] are used extensively throughout this subsection. The following two assumptions are made:

1. Each body can be modeled as a point-mass, or particle
2. There are no internal nor external forces acting on the system of particles other than the gravitational attraction between particles contained within the system

Figure 2.1 shows a system of two particles and their positions with respect to an inertial frame $\hat{i}$. The Law of Universal Gravitation states that each particle exerts a force on the other along the line joining the two centers of the bodies, that is directly proportional to the product of the two masses and indirectly proportional to the square of the distance between them. More precisely, the force that particle i exerts on particle j is given by:

$$\vec{F}_i = -G\frac{m_i m_j}{r_{i,j}^2}\hat{r}_{i,j} = -G\frac{m_i m_j}{r_{i,j}^3}(\vec{r}_j - \vec{r}_i) \tag{2.1}$$

Applying Newton's Second Law provides the following equations of motion for each particle with respect to the origin:

$$m_1\ddot{\vec{r}}_1 = -G\frac{m_1 m_2}{r_{2,1}^3}(\vec{r}_1 - \vec{r}_2) \tag{2.2}$$

$$m_2\ddot{\vec{r}}_2 = -G\frac{m_1 m_2}{r_{1,2}^3}(\vec{r}_2 - \vec{r}_1) \tag{2.3}$$

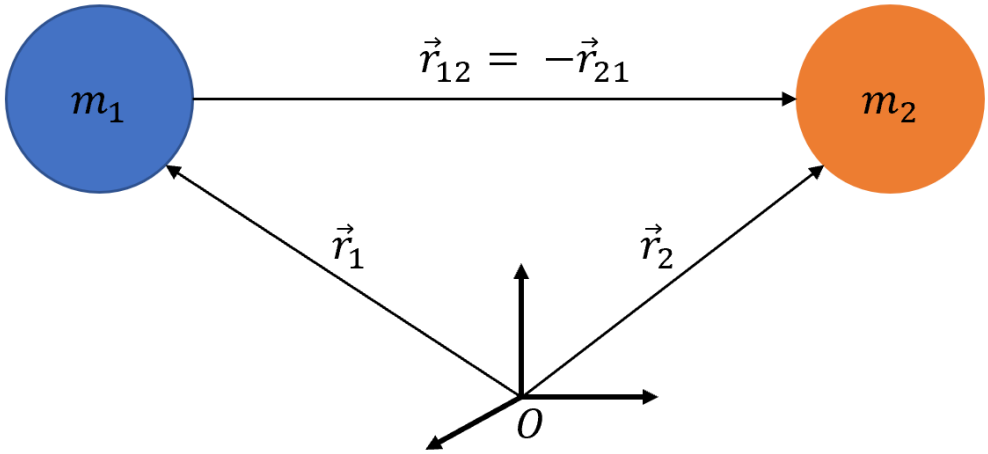

Figure 2.1.. Two bodies of mass m_i shown with position $\vec{r}_i$ in the inertial coordinate frame with origin O.

Because the forces act in opposite directions, along the same line of action, with equal magnitude, they cancel, providing the following:

$$m_1\ddot{\vec{r}}_1 + m_2\ddot{\vec{r}}_2 = \vec{0} \tag{2.4}$$

Which indicates that the center of mass, is not accelerating. For this reason the center of mass of the system can be used as the origin of the inertial frame.

$$m_1\vec{r}_1 + m_2\vec{r}_2 = \vec{0}$$
$$-\frac{m_1}{m_2}\vec{r}_1 = \vec{r}_2$$

Reworking Equations 2.2 and 2.3 to represent the position of each particle with respect to the center of mass yields the following:

$$\ddot{\vec{r}}_1 = -G\frac{(m_1 + m_2)}{r_{2,1}^3}\vec{r}_1 \tag{2.5}$$

$$\ddot{\vec{r}}_2 = -G\frac{(m_1 + m_2)}{r_{1,2}^3}\vec{r}_2 \tag{2.6}$$

Taking the difference between Equation 2.6 and Equation 2.5 provides the relative equation of motion. Defining $\mu = G(m_1 + m_2)$ and the relative position vector $\vec{r} = \vec{r}_2 - \vec{r}_1$, the relative equation of motion for the two-body problem is given as:

$$\ddot{\vec{r}} = -\frac{\mu}{r^3}\vec{r} \tag{2.7}$$

To solve a second order, vector differential equation six integrals of motion are required. To find the integrals of motion several vector operations are conducted on Equation 2.7 to produce what are known as the *orbital elements*. First, by crossing $\vec{r}$ with 2.7:

$$\begin{aligned}
\vec{r} \times \frac{d\vec{v}}{dt} &= \frac{d}{dt}(\vec{r} \times \vec{v}) - \cancelto{0}{\frac{d\vec{r}}{dt} \times \vec{v}} \\
\vec{r} \times -\frac{\mu}{r^3}\vec{r} &= \vec{0} \\
\frac{d}{dt}(\vec{r} \times \vec{v}) &= \vec{0}
\end{aligned}$$

Integrating this provides three constants of integration in vector form, called *specific angular momentum* ($\vec{h}$):

$$\vec{r} \times \vec{v} = \vec{h} \tag{2.8}$$

Because $\vec{h}$ is constant, motion of the particle is restricted to a plane that is orthogonal to $\vec{h}$. Expressing this in polar coordinates gives:

$$\vec{h} = r^2 \frac{d\theta}{dt}\hat{i}_z \tag{2.9}$$

Where $\hat{i}_z$ is collinear with $\vec{h}$, oriented normal to the plane of motion. Next, Equation 2.7 can be crossed with $\vec{h}$:

$$\begin{aligned}
\frac{d\vec{v}}{dt} \times \vec{h} &= -\frac{\mu}{r^3}\vec{r} \times \vec{h} \\
&= -\frac{\mu}{r^2}\hat{i}_r \times h\hat{i}_z \\
&= \frac{\mu h}{r^2}\hat{i}_\theta \\
&= \mu \frac{d\theta}{dt}\hat{i}_\theta \\
&= \mu \frac{d\hat{i}_r}{dt}
\end{aligned}$$

Because $\vec{h}$ is constant, the following relation applies:

$$\frac{d\vec{v}}{dt} \times \vec{h} = \frac{d}{dt}(\vec{v} \times \vec{h}) - \vec{v} \times \cancelto{0}{\frac{d\vec{h}}{dt}}$$
$$\frac{d}{dt}(\vec{v} \times \vec{h}) = \mu \frac{d}{dt}\left(\frac{\vec{r}}{r}\right)$$

Integrating this equation provides a constant of the motion called the *eccentricity vector* ($\vec{e}$):

$$(\vec{v} \times \vec{h}) - \frac{\mu}{r}\vec{r} = \mu\vec{e} \tag{2.10}$$

Although $\vec{e}$ is a vector, it only provides two integrals of the motion. This is because $\vec{e}$ is not independent of $\vec{h}$, and can be shown to exist in the plane of motion. For this reason, one last integral of the motion is required to produce a unique solution to the second order, vector differential equation 2.7. Starting with the following:

$$\dot{\vec{r}} \cdot \ddot{\vec{r}} - \dot{\vec{r}} \cdot \ddot{\vec{r}} = 0$$

A simple manipulation of the product rule of differentiation gives:

$$\frac{d}{dt}(\dot{\vec{r}} \cdot \dot{\vec{r}}) = \dot{\vec{r}} \cdot \ddot{\vec{r}} + \ddot{\vec{r}} \cdot \dot{\vec{r}}$$
$$= 2(\dot{\vec{r}} \cdot \ddot{\vec{r}})$$

which can be substituted into the expression above, along with Equation 2.7:

$$0 = \frac{1}{2}\frac{d}{dt}[\vec{v} \cdot \vec{v}] + \frac{\mu}{r^3}\vec{r} \cdot \dot{\vec{r}}$$
$$= \frac{1}{2}\frac{d}{dt}[v^2] + \frac{\mu}{r^3}\frac{1}{2}\frac{d}{dt}[\vec{r} \cdot \vec{r}]$$
$$= \frac{1}{2}\frac{d}{dt}[v^2] + \frac{\mu}{r^2}\dot{r}$$

Now, the following can be noted to substitute into the given formulation:

$$\frac{d}{dt}\left[-\frac{\mu}{r}\right] = \frac{\mu}{r^2}\dot{r}$$

$$0 = \frac{1}{2}\frac{d}{dt}[v^2] - \frac{d}{dt}\left[\frac{\mu}{r}\right]$$

Integration of this equation generates a constant interpreted as *specific orbital energy* (ϵ). The following equation is known as the *Vis-Viva Equation*:

$$\epsilon = \frac{v^2}{2} - \frac{\mu}{r} \tag{2.11}$$

With all of the integrals of motion accounted for a complete solution for the two-body problem can be found. Equation 2.10 can be used to show that each particular solution to the relative equation of motion is a unique conic. To do this, start by taking the dot product of $\vec{r}$ with Equation 2.10:

$$\begin{aligned}
\vec{r} \cdot (\vec{h} \times \dot{\vec{r}}) &= -\mu \vec{r} \cdot \left(\frac{\vec{r}}{r} + \vec{e} \right) \\
\vec{h} \cdot (\dot{\vec{r}} \times \vec{r}) &= -\mu \left(\frac{1}{r} \vec{r} \cdot \vec{r} + \vec{r} \cdot \vec{e} \right) \\
-\vec{h} \cdot \vec{h} &= -\mu (r + \vec{r} \cdot \vec{e}) \\
\frac{h^2}{\mu} &= r + re\cos(\theta^*)
\end{aligned}$$

This can be rearranged to produce the conic equation in polar coordinates relative to the attracting focus:

$$r(\theta^*) = \frac{p}{1 + e\cos(\theta^*)} \tag{2.12}$$

Where $p = h^2/\mu$ is the *semi-latus rectum* of the conic section, e is the magnitude of the eccentricity vector, and θ^* is called the *true anomaly*: the angle made by $\hat{e}$ and $\hat{r}$. An elliptical orbit in the perifocal frame ($\hat{e},\ \hat{p},\ \hat{h}$) is shown in Figure 2.2.

Although there is a lot more to be said about the two-body problem, this summary is adequate for the scope of this document. The primary conclusions are as follows:

1. The motion of a body with respect to another, governed by two-body dynamics exists on a plane orthogonal to $\vec{h} = \vec{r} \times \vec{v}$.

2. The motion on this plane follows the path of a conic define by Equation 2.12, either closed (circle or ellipse) or open (parabola or hyperbola).

3. The orbit is bound by conservation of specific energy, resulting in the Vis-Viva Equation 2.11.

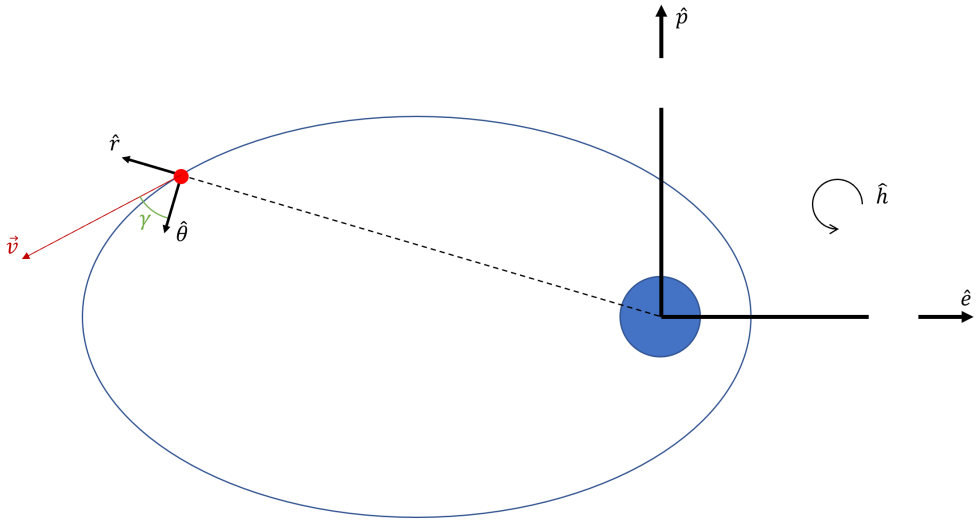

Figure 2.2.. Elliptical orbit shown in the perifocal frame. The angle made by $\hat{r}$ and $\hat{e}$ is known as true anomaly. The angle made between the velocity vector and $\hat{\theta}$ is known as *Flight Path Angle* (γ).

2.2 Coordinate Frames and Time

The developments in this section follow those of References [4,22] closely. To make use of the solution to the two-body problem it is required that an inertial reference frame is defined and realized to the best of our ability. Additionally, because observations are made on the surface of the Earth, an Earth-fixed or Terrestrial reference frame must be defined, and the relationship between the celestial and terrestrial frame must be understood.

The *ecliptic plane* is the orbital plane of the Earth around the sun. The *equatorial plane* is the plane orthogonal to the Earth's spin axis. The intersection of these two planes creates a line, the positive orientation of which defines what is called the *Vernal Equinox* or *Spring Equinox*. In reality, the Earth's orbital plane and spin axis are never constant. External forces and torques on the system are in fact present, and the Earth and sun are not perfect point masses. This means the orientation of

the vernal equinox is constantly changing over time. For this reason, a reference time or *epoch* is used to specify a fixed, instantaneous point of reference. Commonly, the epoch J2000.0 is used, which refers to January 1^{st}, 2000, 12:00, although others may be used as well. By referring back to a specified epoch, a quasi-inertial reference frame can be defined with the following:

- Origin: Center of the Earth
- Fundamental Plane: Equator at a specified reference epoch
- Reference Direction: The vernal equinox at a fixed equinox
- Handedness: Right-handed system

The International Earth Rotation and Reference System Service (IERS) maintains what is called the International Celestial Reference System (ICRS) and International Terrestrial Reference System (ITRS). The ICRS contains the precise positions of thousands of extragalactic radio sources in J2000 using Very Long Baseline Interferometry (VLBI). The positions of these sources do not change significantly over time, and as a result are able to be used as references to orient the International Celestial Reference Frame (ICRF) [23]. The ITRS contains Cartesian measurements taken from stations around the world. These are used to realize the ideal ECEF frame: the ITRF. Updated versions of the ITRF are released every few years to account for variations in Earth modeling parameters [24].
To transform from a J2000.0 ECI frame to an ECEF frame, a rotation matrix can be used for the specified instant in time:

$$\vec{r}_{ECEF} = \mathbf{\Pi}(t)\mathbf{\Theta}(t)\boldsymbol{N}(t)\boldsymbol{P}(t)\vec{r}_{ECI} \tag{2.13}$$

Where each transformation models a specific effect on the Earth's motion:

- $\boldsymbol{P}(t)$: Precession of the Earth's axis of rotation. Precession theory given by Lieske et al. 1977 [25].

- $\boldsymbol{N}(t)$: Nutation of the Earth's axis of rotation. Nutation theory given by Seidelmann 1982 [26].
- $\boldsymbol{\Theta}(t)$: Sidereal Time in UT1, accounting for the Earth's rotation about its axis.
- $\boldsymbol{\Pi}(t)$: Motion of the Earth's pole with respect to the coordinate systems reference pole. Value's for this transformation are released by the IERS Earth Observation Parameters (EOP).

Because each matrix is a function of time, it is important that a well-defined system for timing be derived before the rotation matrix can be implemented.

2.2.1 Time

For a long time, humans have tracked the passage of time through the motion of the sun and other stars. As discussed previously in this section, this is not as consistent as it was once believed to be. Traditionally, when referring to time, the *solar day* is used, which equates to 86400 seconds, or the time between subsequent sun meridian transits. Because the Earth is in fact rotating around the sun and spinning around its own axis, it takes less than one solar day to complete one revolution. This is called a *sidereal day*, and is roughly 23 hours 56 min, 4.1 sec. In addition to this bit of nomenclature, the effect's of Earth precession, nutation, and polar motion shift the apparent vernal equinox and change the length of days. Including the effect's of relativity, one must also account for the position and velocity of the clock with respect to other bodies if seeking a truly accurate representation of atomic time. For these reasons, a uniform time scale that can be actualized is required.

Universal Time (UT1) is the modern version of *Greenwich Mean Sidereal Time (GMST)*, or the Greenwich hour angle of the vernal equinox. This is the primary input to many Earth rotation algorithms, but is not possible to derive analytically due to the unpredictable motion of the Earth. For this reason it is related to *Coordinated Universal Time (UTC)*. UTC is maintained by a network of synchronized

atomic clocks which define *International Atomic Time (TAI)*. These clocks provide TAI time which is offset from UTC by an integer set of seconds, called Leap Seconds, to keep UTC within 1 second of UT1. The number of leap seconds, and additional offset of UTC from UT1 is maintained by the IERS, as UT1 can be actualized by monitoring the quasars used to maintain ICRS. As of January 1^{st} 2020, $TAI - UTC = 37$ leap seconds, and $UT1 - UTC = -0.2$.

GMST can be found using the following empirical relation:

$$\begin{aligned} GMST = {} & 24110.5481 + 8640184.812866T_0 + 1.002737909350795UT1 \\ & + 0.093104T^2 - 0.0000062T^3, \end{aligned} \tag{2.14}$$

where T is Julian centuries since J2000.0 and T_0 is the Julian centuries since J2000.0 at the beginning of the specified day. The output of Equation 2.14 is in seconds. T and T_0 are given by:

$$T = \frac{JD(UT1) - 2451545}{36525} \tag{2.15}$$

$$T_0 = \frac{JD(0\,hr\ UT1) - 2451545}{36525}. \tag{2.16}$$

Because UTC and UT1 are kept within 1 seconds of each other, they can be used interchangeably for an approximation.

2.2.2 Earth Precession, Nutation, and Polar Motion

With the convention for time defined, the motion of the vernal equinox due to Earth precession, nutation, and polar motion can be quantified. With models for the motion due to these effects, and knowledge of the local hour angle, the transformation between ECI and ECEF can be conducted as shown in Equation 2.13 as a function of time.

The transformation due to precession is given as a 313 or $z\,, x\,, z$ rotation:

$$\mathbf{P} = \mathbf{R}_z(-90^\circ - z)\mathbf{R}_x(\theta)\mathbf{R}_z(90^\circ - \zeta) \tag{2.17}$$

$$= \mathbf{R}_z(-z)\mathbf{R}_y(\theta)\mathbf{R}_z(-\zeta). \tag{2.18}$$

Which results in the following rotation matrix:

$$\mathbf{P} = \begin{bmatrix} p_{11} & p_{12} & p_{13} \\ p_{21} & p_{22} & p_{23} \\ p_{31} & p_{32} & p_{33} \end{bmatrix} \tag{2.19}$$

$$\begin{aligned} p_{11} &= \cos(z)\cos(\theta)\cos(\zeta) - \sin(z)\sin(\zeta) \\ p_{12} &= -\cos(z)\cos(\theta)\sin(\zeta) - \sin(z)\cos(\zeta) \\ p_{13} &= -\cos(z)\sin(\theta) \end{aligned} \tag{2.20}$$

$$\begin{aligned} p_{21} &= \sin(z)\cos(\theta)\cos(\zeta) + \cos(z)\sin(\zeta) \\ p_{22} &= -\sin(z)\cos(\theta)\sin(\zeta) + \cos(z)\cos(\zeta) \\ p_{23} &= -\sin(z)\sin(\theta) \end{aligned} \tag{2.21}$$

$$\begin{aligned} p_{31} &= \sin(\theta)\cos(\zeta) \\ p_{32} &= -\sin(\theta)\sin(\zeta) \\ p_{33} &= \cos(\theta) \end{aligned} \tag{2.22}$$

where $(z,\ ,\theta\ ,\zeta)$ are the equatorial precession parameters required to transform the vernal equinox from J2000.0 to mean of date. They are given by the following empirical definitions:

$$\begin{aligned} \zeta &= 2306".2181T + 0".30188T^2 + 0".017998T^3 \\ \theta &= 2004".3109T - 0".42665T^2 - 0".041833T^3 \\ z &= \zeta + 0".79280T^2 + 0".000205T^3 \end{aligned} \tag{2.23}$$

where T is given in Equation 2.15. The transformation due to nutation is given as a 131, or $x\ , z\ , x$ rotation:

$$\mathbf{N} = \mathbf{R}_x(-\epsilon - \Delta\epsilon)\mathbf{R}_z(-\Delta\psi)\mathbf{R}_x(\epsilon). \tag{2.24}$$

Which results in the following rotation matrix:

$$\mathbf{N} = \begin{bmatrix} n_{11} & n_{12} & n_{13} \\ n_{21} & n_{22} & n_{23} \\ n_{31} & n_{32} & n_{33} \end{bmatrix} \tag{2.25}$$

$$
\begin{aligned}
n_{11} &= \cos(\Delta\psi) \\
n_{12} &= -\cos(\epsilon)\sin(\Delta\psi) \qquad (2.26) \\
n_{13} &= -\sin(\epsilon)\sin(\Delta\psi) \\
n_{21} &= \cos(\epsilon')\sin(\Delta\psi) \\
n_{22} &= \cos(\epsilon)\cos(\epsilon')\cos(\Delta\psi) + \sin(\epsilon)\sin(\epsilon') \qquad (2.27) \\
n_{23} &= \sin(\epsilon)\cos(\epsilon')\cos(\Delta\psi) - \cos(\epsilon)\sin(\epsilon') \\
n_{31} &= \sin(\epsilon')\sin(\Delta\psi) \\
n_{32} &= \cos(\epsilon)\sin(\epsilon')\cos(\Delta\psi) - \sin(\epsilon)\cos(\epsilon') \qquad (2.28) \\
n_{33} &= \sin(\epsilon)\sin(\epsilon')\cos(\Delta\psi) + \cos(\epsilon)\cos(\epsilon'),
\end{aligned}
$$

where ϵ and $\epsilon' = \epsilon + \Delta\epsilon$ are the mean and true obliquity of the ecliptic, and $\Delta\psi$ is the periodic shift of the vernal equinox. These parameters account for the small periodic perturbations caused by lunar and solar moments on the Earth. The mean obliquity of the ecliptic is given by the empirical equation:

$$\epsilon = 23^\circ.43929111 - 46".8150T - 0".00059T^2 + 0".001813T^3. \qquad (2.29)$$

The IAU 1980 Nutation model expresses the periodic changes in the angles ϵ and ψ in series form:

$$\Delta\psi = \sum_{i=1}^{106} (\Delta\psi)_i \sin(\phi_i) \qquad (2.30)$$

$$\Delta\epsilon = \sum_{i=1}^{106} (\Delta\epsilon)_i \cos(\phi_i), \qquad (2.31)$$

where $(\Delta\psi)_i$ and $(\Delta\epsilon)_i$ are tabulated values and ϕ_i is made up of tabulated values and various functions of time. This is given as:

$$\phi_i = p_{l,i}l + p_{l',i}l' + p_{F,i}F + p_{D,i}D + p_{\Omega,i}\Omega. \qquad (2.32)$$

The p_i terms are tabulated integer values provided with the IAU 1980 Nutation Theory, and the other terms are as follows:

- l: Moon's Mean Anomaly

- l': Sun's Mean Anomaly
- F: Mean distance of the Moon from the ascending node
- D: Difference between the mean longitudes of the Sun and Moon
- Ω: Mean longitude of the ascending node of the lunar orbit

These are given through empirically defined terms as a function of T:

$$\begin{aligned} l &= 134^\circ 57' 46".733 + 477198^\circ 52' 02".633T + 31".310T^2 + 0".064T^3 \\ l' &= 357^\circ 31' 39".804 + 35999^\circ 03' 01".224T - 0".577T^2 - 0".012T^3 \\ F &= 93^\circ 16' 18".877 + 483202^\circ 01' 03".137T - 13".257T^2 + 0".011T^3 \\ D &= 297^\circ 51' 01".307 + 445267^\circ 06' 41".328T - 6".891T^2 + 0".019T^3 \\ \Omega &= 125^\circ 02' 40".280 - 1934^\circ 08' 10".539T + 7".455T^2 + 0".008T^3. \end{aligned} \tag{2.33}$$

Equation 2.15 takes UT1 and provides the time input for the parameters above. With these, and the known tabulated values for the IAU 1980 Nutation Theory, the nutation transformation ($\mathbf{N}(t)$) can be computed. This transformation applied to the mean of date output from precession theory provides the true of date, which refers to the true vernal equinox at the input time T.

With precession and nutation accounted for, the instantaneous orientation of the Earth's axis of rotation at the specified time T is determined. The transformation to align this frame with the equator and Greenwich meridian is simply a rotation about this axis:

$$\mathbf{\Theta}(t) = \boldsymbol{R}_z(GAST) \tag{2.34}$$

$$= \begin{bmatrix} \cos(GAST) & \sin(GAST) & 0 \\ -\sin(GAST) & \cos(GAST) & 0 \\ 0 & 0 & 1 \end{bmatrix}, \tag{2.35}$$

where $GAST$ is Greenwich Apparent Sidereal Time. It is related to Greenwich Mean Sidereal Time by the Equation of the Equinoxes:

$$GAST - GMST = \Delta\psi \cos(\epsilon), \tag{2.36}$$

which is related to UT1 in Equation 2.14, and the nutation angles in Equations 2.29 and 2.30.

The last transformation to account for is polar motion. Unlike precession and nutation, there exist no models to predict the effects of polar motion. Fortunately the effects can be measured, and incorporated post factum. These parameters are monitored by IERS and released in their associated Bulletin B. This results in the following transformation:

$$\mathbf{\Pi}(t) = \boldsymbol{R}_y(-x_p)\boldsymbol{R}_x(-y_p) \approx \begin{bmatrix} 1 & 0 & x_p \\ 0 & 1 & -y_p \\ -x_p & y_p & 1 \end{bmatrix} \tag{2.37}$$

The small angles associated with x_p and y_p allow for the dismissal of higher order terms, leaving the approximation given above.

2.2.3 Topocentric Reference Frames

In reality, all users of the terrestrial and celestial reference frames described in the previous sections are on the surface of the Earth, not the center. This necessitates the definition of a usable *topocentric frame*: a frame that is centered at an arbitrary location on the surface of the Earth.

To start, an object's geocentric position with respect to an inertial frame can be expressed in spherical coordinates using Right Ascension (α), Declination (δ), and radius (r). The transformation to Cartesian space is given by:

$$\vec{r} = r \begin{bmatrix} \cos(\alpha)\cos(\delta) \\ \sin(\alpha)\cos(\delta) \\ \sin(\delta) \end{bmatrix} \tag{2.38}$$

The origin of the topocenter, or the observer location is generally expressed in geodetic Longitude (λ), Latitude (φ), altitude above reference ellipsoid (h). There exist various sets of parameters to define a reference ellipsoid to model the Earth's surface.

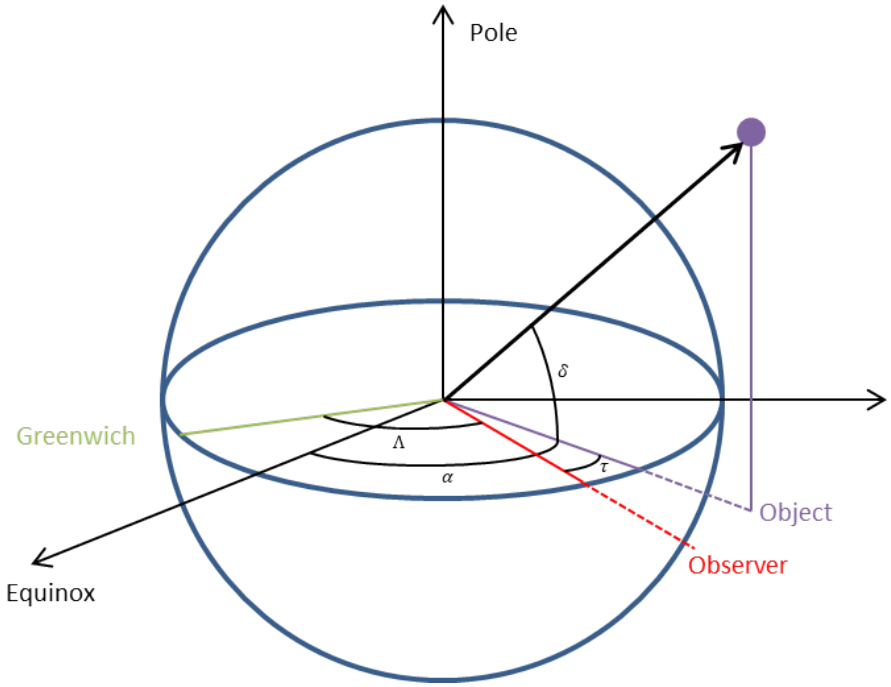

Figure 2.3.. Angles orienting the object position vector in the equatorial plane.

The ITRF defines the reference ellipsoid using two parameters: mean Earth equatorial radius ($R_\oplus = 6378.137$ km) and a flattening parameter ($f = 1/298257222101$). The transformation from geodetic to Cartesian space is given by:

$$\vec{r}_{obs,ECEF} = \begin{bmatrix} (N+h)\cos(\varphi)\cos(\lambda) \\ (N+h)\cos(\varphi)\sin(\lambda) \\ \left((1-f)^2 N + h\right)\sin(\varphi) \end{bmatrix} \tag{2.39}$$

$$N = \frac{R_\oplus}{\sqrt{1 - f(2-f)\sin^2(\varphi)}}$$

The sidereal time (θ) is the right ascension of the observer. This differs from longitude, as longitude is the angular distance of the observer from Greenwich, while right ascension is the angular distance from the vernal equinox, as shown in Figure 2.3.

The hour angle (τ) is the difference between the sidereal time and the right ascension of an object. That is:

$$\tau = \theta - \alpha \tag{2.40}$$

At stellar distances, the change in location of the origin from the center of the Earth to the topocenter has little to no impact on the angles of observation. In the case of Earth orbiting objects, this change has a drastic impact on angular measures. For this reason, the *Topocentric Equatorial System* is defined. This frame uses the same fundamental plane, and reference direction as the ECI frame, but its origin is located at the topocenter on the Earth's surface. Positions are described using topocentric right ascension (α'), declination (δ'), and range (ρ). This produces the following transformation:

$$\vec{r}_{Geo} = \vec{r}_{Topo} + \vec{r}_{obs,ECI} \tag{2.41}$$

$$\rho = ||\vec{r}_{Geo} - \vec{r}_{obs,ECI}|| \tag{2.42}$$

$$r \begin{bmatrix} \cos(\alpha)\cos(\delta) \\ \sin(\alpha)\cos(\delta) \\ \sin(\delta) \end{bmatrix} = \rho \begin{bmatrix} \cos(\alpha')\cos(\delta') \\ \sin(\alpha')\cos(\delta') \\ \sin(\delta') \end{bmatrix} + \Big(\mathbf{\Pi}(t)\mathbf{\Theta}(t)\boldsymbol{N}(t)\boldsymbol{P}(t)\Big)^{-1} \vec{r}_{obs,ECEF}$$

Notice that because the topocenter is located on the surface of the Earth, its position is time dependent. This means that knowledge of the time of observation is required to conduct the transformation.

In general, optical measurements are made with respect to the local horizon defined by the topocenter. Positions are defined by the angles Azimuth (A) and Elevation (E), and the range (ρ). Figure 2.2.3 shows the angular defenitions used here. Note that is also common to see azimuth and elevation defined southward as opposed to the northward configuration shown in the figure. Both frames are left-handed. The

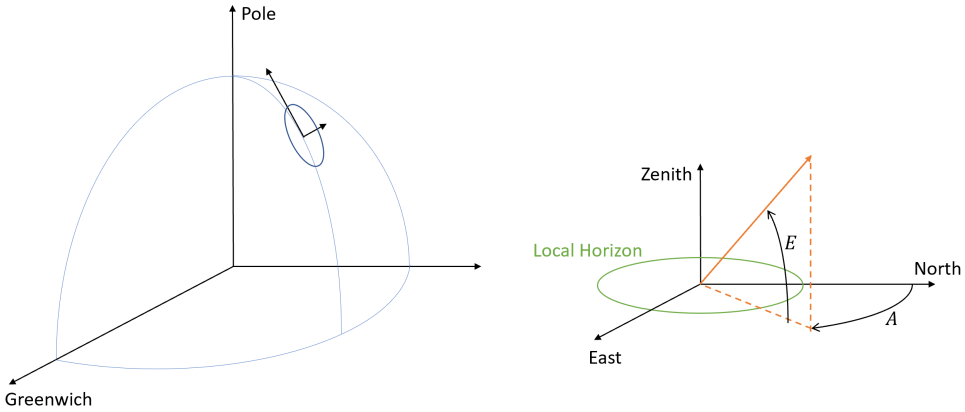

Figure 2.4.. Angular definition in the topocentric local horizon reference frame.

transformation from the local horizon to the topocentric equitorial system can be accomplished with the following rotations and reflection:

$$\begin{bmatrix} \cos(\alpha')\cos(\delta') \\ \sin(\alpha')\cos(\delta') \\ \sin(\delta') \end{bmatrix} = \boldsymbol{S_3 R_3}(\theta)\boldsymbol{R_2}(\varphi + 90^\circ) \begin{bmatrix} \cos(A)\cos(E) \\ \sin(A)\cos(E) \\ \sin(E) \end{bmatrix}. \tag{2.43}$$

$\boldsymbol{R}_i(\theta)$ is the direction cosine matrix associated with a rotation of angle θ about the i axis, and $\boldsymbol{S}_i$ is the reflection matrix which mirrors the orientation of the i axis. The reflection is required because the resultant local-horizon reference system is left-handed. After processing each of these matrices, the transformation can be written in terms of hour angle as:

$$\begin{bmatrix} \cos(\tau')\cos(\delta') \\ \sin(\tau')\cos(\delta') \\ \sin(\delta') \end{bmatrix} = \begin{bmatrix} \cos(\varphi)\sin(E) - \sin(\varphi)\cos(E)\cos(A) \\ -\cos(E)\sin(A) \\ \sin(\varphi)\sin(E) + \sin(\varphi)\cos(E)\cos(A) \end{bmatrix}, \tag{2.44}$$

where $\tau' = \theta - \alpha'$. The inverse transformation is given as:

$$\begin{bmatrix} \cos(E)\cos(A) \\ \sin(A)\cos(E) \\ \sin(E) \end{bmatrix} = \begin{bmatrix} \cos(\varphi)\sin(\delta) - \sin(\varphi)\cos(\delta)\cos(\tau') \\ -\cos(\delta)\sin(\tau') \\ \sin(\varphi)\sin(\delta) + \cos(\varphi)\cos(\delta)\cos(\tau') \end{bmatrix}. \tag{2.45}$$

Note that range has been removed as the two position vectors should have equal magnitude. Additionally, for optical measurements range cannot be observed directly. Azimuth and elevation can be transformed to topocentric right ascension and declination, but the geocentric right ascension and declination cannot be determined directly from a single angles-only measurement.

2.3 Classical Orbit Determination Methods

With the previously shown developments on coordinate frames and time, observations can be made on the surface of the Earth and related back to a quasi-inertial reference frame at a specified epoch. In most cases, users are interested in the full state (position and velocity) at a given reference time in the inertial frame, which is defined at a standard epoch. Optical measurements provide two angles which can be used to determine the line of sight to the object of interest, but do not provide range measurements. For this reason, methods have been developed to use multiple measurements and knowledge of the dynamics to produce a solution to the orbit determination problem using angles-only measurements. Note that even with range measurements, the range-rate and angular rate data are required as well to produce a full-state solution.

The first of these methods was developed by Laplace in 1780. The method assumes that the user has at least three topocentric optical observations $z_i = (\alpha_i, \delta_i)$ of the same object. This gives the following line of sight vector:

$$\hat{l}_i = \begin{bmatrix} \cos(\alpha_i)\cos(\delta_i) \\ \sin(\alpha_i)\cos(\delta_i) \\ \sin(\delta_i) \end{bmatrix}. \tag{2.46}$$

The position of the object is then given by:

$$\vec{r}_i = \vec{r}_{obs,i} + \rho_i \hat{l}_i \tag{2.47}$$

where $\vec{r}_{obs,i}$ is the observers position at time i which is assumed to be known. The magnitude of the objects can be computed as:

$$|\vec{r}_i|^2 = \vec{r}_i \cdot \vec{r}_i = |\vec{r}_{obs,i}|^2 + \rho_i^2 + 2\rho_i\big(\hat{l}_i \cdot \vec{r}_{obs,i}\big) \tag{2.48}$$

Taking the time derivatives of Equation 2.47 gives the object velocity and acceleration:

$$\begin{aligned} \dot{\vec{r}}_i &= \dot{\vec{r}}_{obs,i} + \dot{\rho}_i \hat{l}_i + \rho_i \dot{\hat{l}}_i \\ \ddot{\vec{r}}_i &= \ddot{\vec{r}}_{obs,i} + \ddot{\rho}_i \hat{l}_i + 2\dot{\rho}_i \dot{\hat{l}}_i + \rho_i \ddot{\hat{l}}_i \end{aligned} \tag{2.49}$$

Assuming that the object is governed by two body motion, the acceleration at i can be set equal to Equation 2.7.

$$\ddot{\vec{r}}_{obs,i} + \ddot{\rho}_i \hat{l}_i + 2\dot{\rho}_i \dot{\hat{l}}_i + \rho_i \ddot{\hat{l}}_i = -\frac{\mu}{r_i^3}\vec{r}_i \tag{2.50}$$

Substituting Equation 2.47 into the above allows for the following reduction:

$$\begin{aligned} \ddot{\vec{r}}_{obs,i} + \ddot{\rho}_i \hat{l}_i + 2\dot{\rho}_i \dot{\hat{l}}_i + \rho_i \ddot{\hat{l}}_i &= -\frac{\mu}{r_i^3}\big(\vec{r}_{obs,i} + \rho_i \hat{l}_i\big) \\ \ddot{\rho}_i \hat{l}_i + 2\dot{\rho}_i \dot{\hat{l}}_i + \rho_i \ddot{\hat{l}}_i + \frac{\mu}{r_i^3}\rho_i \hat{l}_i &= -\frac{\mu}{r_i^3}\vec{r}_{obs,i} - \ddot{\vec{r}}_{obs,i} \end{aligned}$$

$$\begin{bmatrix} \hat{l}_i & 2\dot{\hat{l}}_i & \ddot{\hat{l}}_i + \frac{\mu}{r_i^3}\hat{l}_i \end{bmatrix} \begin{bmatrix} \ddot{\rho}_i \\ \dot{\rho}_i \\ \rho_i \end{bmatrix} = -\left(\frac{\mu}{r_i^3}\vec{r}_{obs,i} + \ddot{\vec{r}}_{obs,i}\right), \tag{2.51}$$

where the matrix given on the left is a 3×3. To determine the full-state, the range (ρ_i) and range-rate ($\dot{\rho}_i$) are needed. These can be solved for using Cramer's Rule. This yields the following:

$$\rho_i = \frac{\begin{vmatrix} \hat{l}_i & 2\dot{\hat{l}}_i & -(\mu/r_i^3\vec{r}_{obs,i} + \ddot{\vec{r}}_{obs,i}) \end{vmatrix}}{\begin{vmatrix} \hat{l}_i & 2\dot{\hat{l}}_i & (\ddot{\hat{l}}_i + \mu/r_i^3\hat{l}_i) \end{vmatrix}} \tag{2.52}$$

$$\dot{\rho}_i = \frac{\begin{vmatrix} \hat{l}_i & -(\mu/r_i^3\vec{r}_{obs,i} + \ddot{\vec{r}}_{obs,i}) & (\ddot{\hat{l}}_i + \mu/r_i^3\hat{l}_i) \end{vmatrix}}{\begin{vmatrix} \hat{l}_i & 2\dot{\hat{l}}_i & (\ddot{\hat{l}}_i + \mu/r_i^3\hat{l}_i) \end{vmatrix}} \tag{2.53}$$

where the numerator and denominator of each of the above are determinants of a 3×3 matrix. At this point, r_i is unknown, and the rates of $\hat{l}_i$ are not directly measured. The acceleration of the observer is found using the known rotation rate of the Earth ($\ddot{\vec{r}}_{obs,i} = \vec{\omega}\times\vec{\omega}\times\vec{r}_{obs,i}$). To proceed, estimates of the line of sight rates are produced by interpolation using Lagrange Polynomials.

$$\begin{aligned}
\hat{l}(t) &= \sum_{i=1}^{n}\hat{l}_i\prod_{\substack{j=1\\j\neq i}}^{n}\frac{(t-t_j)}{(t_i-t_j)}\\
\dot{\hat{l}}(t) &= \sum_{i=1}^{n}\hat{l}_i\left(\prod_{\substack{j=1\\j\neq i}}^{n}\frac{(t-t_j)}{(t_i-t_j)}\right)\left(\sum_{\substack{k=1\\k\neq i}}^{n}\frac{1}{(t-t_k)}\right)\\
\ddot{\hat{l}}(t) &= \sum_{i=1}^{n}\hat{l}_i\left(\prod_{\substack{j=1\\j\neq i}}^{n}\frac{(t-t_j)}{(t_i-t_j)}\right)\left[\left(\sum_{\substack{k=1\\k\neq i}}^{n}\frac{1}{(t-t_k)}\right)^2-\sum_{\substack{h=1\\h\neq i}}^{n}\frac{1}{(t-t_h)^2}\right]
\end{aligned}\tag{2.54}$$

Setting $n=3$ produces the following:

$$\begin{aligned}
\hat{l}(t) &= \hat{l}_1\frac{(t-t_2)(t-t_3)}{(t_1-t_2)(t_1-t_3)}+\hat{l}_2\frac{(t-t_1)(t-t_3)}{(t_2-t_1)(t_2-t_3)}+\hat{l}_3\frac{(t-t_1)(t-t_2)}{(t_3-t_1)(t_3-t_2)}\\
\dot{\hat{l}}(t) &= \hat{l}_1\frac{2t-t_3-t_2}{(t_1-t_2)(t_1-t_3)}+\hat{l}_2\frac{2t-t_1-t_3}{(t_2-t_1)(t_2-t_3)}+\hat{l}_3\frac{2t-t_1-t_2}{(t_3-t_1)(t_3-t_2)}\\
\ddot{\hat{l}}(t) &= \hat{l}_1\frac{2}{(t_1-t_2)(t_1-t_3)}+\hat{l}_2\frac{2}{(t_2-t_1)(t_2-t_3)}+\hat{l}_3\frac{2}{(t_3-t_1)(t_3-t_2)}
\end{aligned}\tag{2.55}$$

Note that $n=3$ is the minimum number of measurements needed to produce an estimate for $\ddot{\hat{l}}(t)$. Any number of measurements greater than three can be used to improve the estimate.

To determine the line of sight rates at one of the observation times, set $t=t_i$, in this case $i=2$. For the case of $n>3$ observations, let $i=(n+1)/2$ assuming total number of observations is odd without loss of generality.

$$\begin{aligned}
\dot{\hat{l}}_2 &= \hat{l}_1\frac{t_2-t_3}{(t_1-t_2)(t_1-t_3)}+\hat{l}_2\frac{2t_2-t_1-t_3}{(t_2-t_1)(t_2-t_3)}+\hat{l}_3\frac{t_2-t_1}{(t_3-t_1)(t_3-t_2)}\\
\ddot{\hat{l}}_2 &= \hat{l}_1\frac{2}{(t_1-t_2)(t_1-t_3)}+\hat{l}_2\frac{2}{(t_2-t_1)(t_2-t_3)}+\hat{l}_3\frac{2}{(t_3-t_1)(t_3-t_2)}
\end{aligned}\tag{2.56}$$

The only unknown that remains is the dependence on r in both range and range-rate. Some basic properties of the determinant can be used to isolate terms. Important properties are as follows:

1. The determinant of a matrix is unchanged if a scalar multiple of any one column is added to another.

2. Multiplying any column of a matrix by a nonzero scalar produces a determinant multiplied by that scalar.

3. If a column of a matrix is given by the sum of two vectors, the determinant is given by the sum of the two determinants made by the matrix with a single vector in the corresponding column.

Now, starting with the denominator:

$$\begin{aligned}
\Delta_0 &= \left|\hat{l}_i \quad 2\dot{\hat{l}}_i \quad (\ddot{\hat{l}}_i + \mu/r_i^3\hat{l}_i)\right| \\
&= \left|\hat{l}_i \quad 2\dot{\hat{l}}_i \quad (\ddot{\hat{l}}_i + \mu/r_i^3\hat{l}_i - \mu/r_i^3\hat{l}_i)\right| \\
&= \left|\hat{l}_i \quad 2\dot{\hat{l}}_i \quad \ddot{\hat{l}}_i\right| \\
&= 2\left|\hat{l}_i \quad \dot{\hat{l}}_i \quad \ddot{\hat{l}}_i\right|.
\end{aligned}$$

Next, the numerator for Equation 2.52:

$$\begin{aligned}
\Delta_0\rho &= \left|\hat{l}_i \quad 2\dot{\hat{l}}_i \quad -(\mu/r_i^3\vec{r}_{obs,i} + \ddot{\vec{r}}_{obs,i})\right| \\
&= -2\left|\hat{l}_i \quad \dot{\hat{l}}_i \quad (\mu/r_i^3\vec{r}_{obs,i} + \ddot{\vec{r}}_{obs,i})\right| \\
&= -2\left|\hat{l}_i \quad \dot{\hat{l}}_i \quad \ddot{\vec{r}}_{obs,i}\right| - 2\left|\hat{l}_i \quad \dot{\hat{l}}_i \quad \mu/r_i^3\vec{r}_{obs,i}\right| \\
&= -2\left|\hat{l}_i \quad \dot{\hat{l}}_i \quad \ddot{\vec{r}}_{obs,i}\right| - 2\frac{\mu}{r_i^3}\left|\hat{l}_i \quad \dot{\hat{l}}_i \quad \vec{r}_{obs,i}\right| \\
&= -2\Delta_1 - 2\frac{\mu}{r_i^3}\Delta_2.
\end{aligned}$$

And lastly, the numerator for Equation 2.53:

$$\begin{aligned}
\Delta_0\dot{\rho} &= \left|\hat{l}_i \quad -(\mu/r_i^3\vec{r}_{obs,i} + \ddot{\vec{r}}_{obs,i}) \quad (\ddot{\hat{l}}_i + \mu/r_i^3\hat{l}_i)\right| \\
&= -\left|\hat{l}_i \quad (\mu/r_i^3\vec{r}_{obs,i} + \ddot{\vec{r}}_{obs,i}) \quad (\ddot{\hat{l}}_i + \mu/r_i^3\hat{l}_i - \mu/r_i^3\hat{l}_i)\right| \\
&= -\left|\hat{l}_i \quad (\mu/r_i^3\vec{r}_{obs,i} + \ddot{\vec{r}}_{obs,i}) \quad \ddot{\hat{l}}_i\right| \\
&= -\left|\hat{l}_i \quad \ddot{\vec{r}}_{obs,i} \quad \ddot{\hat{l}}_i\right| - \mu/r_i^3\left|\hat{l}_i \quad \vec{r}_{obs,i} \quad \ddot{\hat{l}}_i\right| \\
&= -\Delta_3 - \frac{\mu}{r_i^3}\Delta_4.
\end{aligned}$$

With these simplifications, Equations 2.52 and 2.53 can be rewritten as:

$$\rho_i = -2\left(\frac{\Delta_1}{\Delta_0}\right) - 2\frac{\mu}{r_i^3}\left(\frac{\Delta_2}{\Delta_0}\right) \tag{2.57}$$

$$\dot{\rho}_i = -\left(\frac{\Delta_3}{\Delta_0}\right) - \frac{\mu}{r_i^3}\left(\frac{\Delta_4}{\Delta_0}\right) \tag{2.58}$$

where:

$$\begin{aligned}
\Delta_0 &= 2\begin{vmatrix} \hat{l}_i & \dot{\hat{l}}_i & \ddot{\hat{l}}_i \end{vmatrix} \\
\Delta_1 &= \begin{vmatrix} \hat{l}_i & \dot{\hat{l}}_i & \ddot{\vec{r}}_{obs,i} \end{vmatrix} \\
\Delta_2 &= \begin{vmatrix} \hat{l}_i & \dot{\hat{l}}_i & \vec{r}_{obs,i} \end{vmatrix} \\
\Delta_3 &= \begin{vmatrix} \hat{l}_i & \ddot{\vec{r}}_{obs,i} & \ddot{\hat{l}}_i \end{vmatrix} \\
\Delta_4 &= \begin{vmatrix} \hat{l}_i & \vec{r}_{obs,i} & \ddot{\hat{l}}_i \end{vmatrix}
\end{aligned} \tag{2.59}$$

The Lagrange Polynomials have provided all of the line of sight rates to compute each of the Δ's above. Now the reduced range and range-rate equations can be substituted into Equation 2.48.

$$|\vec{r}_i|^2 = |\vec{r}_{obs,i}|^2 + \left(-2\left(\frac{\Delta_1}{\Delta_0}\right) - 2\frac{\mu}{r_i^3}\left(\frac{\Delta_2}{\Delta_0}\right)\right)^2 + 2\left(-2\left(\frac{\Delta_1}{\Delta_0}\right) - 2\frac{\mu}{r_i^3}\left(\frac{\Delta_2}{\Delta_0}\right)\right)\left(\hat{l}_i \cdot \vec{r}_{obs,i}\right)$$

Which can be rearranged to produce:

$$\begin{aligned}
r_i^8 &+ \left(4\frac{\Delta_1}{\Delta_0}(\hat{l}\cdot\vec{r}_{obs,i}) - 4\left(\frac{\Delta_1}{\Delta_0}\right)^2 - r_{obs,i}^2\right)r_i^6 \\
&+ \left(4\mu\frac{\Delta_2}{\Delta_0}(\hat{l}\cdot\vec{r}_{obs,i}) - 8\mu\frac{\Delta_1\Delta_2}{\Delta_0^2}\right)r_i^3 - 4\mu^2\left(\frac{\Delta_2}{\Delta_0}\right)^2 = 0
\end{aligned} \tag{2.60}$$

So, using the measurements (z_i) to produce the estimates of the line of site rates in Equation 2.56, the Δ functions can be produced to solve for r_2 using the 8^{th} order polynomial above. This can then be used in Equations 2.52 and 2.53 to ultimately obtain estimates for $\vec{r}_2$ and $\vec{v}_2$. Equation 2.60 can be solved numerically using a simple Newton-Raphson method. The equation provides 8 solutions, 6 of which will be imaginary, one of which will be negative real, and the desired solution will be

positive real. The following method is run until a sufficiently small update step ($\Delta r_{2,n}$) is produced:

$$r_{2,(n+1)} = r_{2,n} - \Delta r_{2,n} \tag{2.61}$$

$$\Delta r_{2,n} = \frac{r_{2,n}^8 + a r_{2,n}^6 + b r_{2,n}^3 + c}{8 r_{2,n}^7 + 6 a r_{2,n}^5 + 3 b r_{2,n}^2} \tag{2.62}$$

$$a = 4\frac{\Delta_1}{\Delta_0}(\hat{l} \cdot \vec{r}_{obs,i}) - 4\frac{\Delta_1^2}{\Delta_0^2} - r_{obs,i}^2$$

$$b = 4\mu\frac{\Delta_2}{\Delta_0}(\hat{l} \cdot \vec{r}_{obs,i}) - 8\mu\frac{\Delta_1 \Delta_2}{\Delta_0^2}$$

$$c = 4\mu^2\frac{\Delta_2^2}{\Delta_0^2}$$

Once the numerical result for r_2 is obtained, the position and velocity can be computed using the following:

$$\rho_2 = -2\left(\frac{\Delta_1}{\Delta_0}\right) - 2\frac{\mu}{r_2^3}\left(\frac{\Delta_2}{\Delta_0}\right) \tag{2.63}$$

$$\dot{\rho}_2 = -\left(\frac{\Delta_3}{\Delta_0}\right) - \frac{\mu}{r_2^3}\left(\frac{\Delta_4}{\Delta_0}\right) \tag{2.64}$$

$$\vec{r}_2 = \vec{r}_{obs,2} + \rho_2 \hat{l}_2 \tag{2.65}$$

$$\dot{\vec{r}}_2 = \dot{\vec{r}}_{obs,2} + \dot{\rho}_2 \hat{l}_2 + \rho_2 \dot{\hat{l}}_2 \tag{2.66}$$

2.4 Orbit Improvement

Although a solution for the state of an RSO at a given time can be produced, it is often necessary to incorporate additional measurements to improve the estimate. Classical orbit determination procedures can be used to initialize an iterative least squares procedure, which is outlined below. Starting with a brief detour, the minimum variance estimate is examined, followed by the non-linear least squares procedure required to implement this estimate in the orbit determination problem. The following developments follow those of References [4, 27, 28].

2.4.1 Linear Unbiased Minimum Variance Estimate: LUMVE

The objective here is to provide a state-estimate of the linear discrete-time system:

$$\vec{x}_i = \mathbf{\Phi}(t_i, t_k)\vec{x}_k, \tag{2.67}$$

given some set of observations:

$$\vec{y}_i = \widetilde{\boldsymbol{H}}\vec{x}_i + \nu_i \tag{2.68}$$

where ν_i is Gaussian white noise ($E[\nu_i] = 0$, $E[\nu_i\nu_j] = R_{ii}\delta_{i,j}$),. $\widetilde{\boldsymbol{H}}$ is a measurement matrix mapping the state space to the measurement space. The measurements can be expressed in matrix from more compactly as:

$$\vec{y} = \boldsymbol{H}\vec{x}_k + \vec{\nu} \tag{2.69}$$

$$\vec{y} = \begin{bmatrix} y_1 \\ y_2 \\ \vdots \\ y_n \end{bmatrix} \quad \boldsymbol{H} = \begin{bmatrix} \widetilde{\boldsymbol{H}}_1\mathbf{\Phi}(t_1, t_k) \\ \widetilde{\boldsymbol{H}}_2\mathbf{\Phi}(t_2, t_k) \\ \vdots \\ \widetilde{\boldsymbol{H}}_n\mathbf{\Phi}(t_n, t_k) \end{bmatrix} \quad \vec{\nu} = \begin{bmatrix} \nu_1 \\ \nu_2 \\ \vdots \\ \nu_n \end{bmatrix}, \tag{2.70}$$

where $\boldsymbol{H}$ is an $m \times n$ matrix mapping state space into measurement space. Additionally $\boldsymbol{R}$ will be used as the measurement noise covariance matrix. The goal is to find the linear, unbiased, minimum variance estimate ($\hat{x}_k$) of the state $\vec{x}_k$. Linear meaning the estimate is a linear combination of the received measurements. Unbiased meaning that the expectation of the estimate is equal to the true state. Minimum variance meaning the smallest possible error covariance. In a more mathematically rigorous sense:

$$Linear: \qquad \hat{x}_k = \boldsymbol{M}\vec{y} \tag{2.71}$$

$$Unbiased: \qquad E[\hat{x}_k] = x_k \tag{2.72}$$

$$Min.\,Var.: \qquad min\{P_k\} = min\{E[(x_k - \hat{x}_k)(x_k - \hat{x}_k)^T]\}. \tag{2.73}$$

Expanding upon the condition given in Equation 2.71 and applying the condition given in Equation 2.72:

$$\begin{aligned} E[\hat{x}_k] &= E[\boldsymbol{M}(\boldsymbol{H}\vec{x}_k + \nu_k)] \\ E[\hat{x}_k] &= \boldsymbol{M}\boldsymbol{H}\ E[\vec{x}_k] + \boldsymbol{M}\ E[\nu_k] \\ \vec{x}_k &= \boldsymbol{M}\boldsymbol{H}\vec{x}_k \end{aligned}$$

This implies the following important outcome:

$$\boldsymbol{M}\boldsymbol{H} = \boldsymbol{I} \tag{2.74}$$

or the rows of $\boldsymbol{M}$ are orthogonal to the columns of $\boldsymbol{H}$. Now, proceeding with the minimum variance condition given in Equation 2.73, $\boldsymbol{P}_k$ can be written as:

$$\begin{aligned} \boldsymbol{P}_k &= E[(\vec{x}_k - \hat{x}_k)(\vec{x}_k - \hat{x}_k)^T]] \\ &= E[(\vec{x}_k - \boldsymbol{M}\boldsymbol{H}\vec{x}_k - \boldsymbol{M}\vec{\nu})(\vec{x}_k - \boldsymbol{M}\boldsymbol{H}\vec{x}_k - \boldsymbol{M}\vec{\nu})^T]. \end{aligned}$$

From the relation given in 2.74, this can be rewritten as:

$$\begin{aligned} &= E[(\vec{x}_k - \vec{x}_k - \boldsymbol{M}\vec{\nu})(\vec{x}_k - \vec{x}_k - \boldsymbol{M}\vec{\nu})^T] \\ &= \boldsymbol{M}\ E[\vec{\nu}\vec{\nu}^T]\ \boldsymbol{M}^T \end{aligned}$$

$$\boldsymbol{P}_k = \boldsymbol{M}\boldsymbol{R}\boldsymbol{M}^T \tag{2.75}$$

Which reduces the problem to selecting the value of $\boldsymbol{M}$ that produces the minimum value of $\boldsymbol{P}_k$ and satisfies the constraint given in Equation 2.74. The method of Lagrange multipliers can be used to find the optimal $\boldsymbol{M}$. This provides the following:

$$\begin{aligned} \boldsymbol{P}_k &= \boldsymbol{M}\boldsymbol{R}\boldsymbol{M}^T + \boldsymbol{\Lambda}^T[\boldsymbol{I} - \boldsymbol{M}\boldsymbol{H}]^T + [\boldsymbol{I} - \boldsymbol{M}\boldsymbol{H}]\boldsymbol{\Lambda} \\ \nabla_{\boldsymbol{M}}\boldsymbol{P}_k &= \boldsymbol{R}\boldsymbol{M}^T + \boldsymbol{M}\boldsymbol{R} - \boldsymbol{\Lambda}^T\boldsymbol{H}^T - \boldsymbol{H}\boldsymbol{\Lambda} = \boldsymbol{0} \\ \boldsymbol{0} &= (\boldsymbol{R}\boldsymbol{M}^T - \boldsymbol{H}\boldsymbol{\Lambda}) + (\boldsymbol{R}\boldsymbol{M}^T - \boldsymbol{H}\boldsymbol{\Lambda})^T. \end{aligned}$$

The optimal solution is found under the following condition for $\boldsymbol{M}$ and $\boldsymbol{\Lambda}$:

$$\boldsymbol{R}\boldsymbol{M}^T - \boldsymbol{H}\boldsymbol{\Lambda} = \boldsymbol{0}. \tag{2.76}$$

Combining Equation 2.74 and 2.76, the following solution is obtained:

$$\boldsymbol{M} = \boldsymbol{\Lambda}^T \boldsymbol{H}^T \boldsymbol{R}^{-1} \tag{2.77}$$

$$\boldsymbol{\Lambda}^T = (\boldsymbol{H}^T \boldsymbol{R}^{-1} \boldsymbol{H})^{-1} \tag{2.78}$$

$$\boldsymbol{M} = (\boldsymbol{H}^T \boldsymbol{R}^{-1} \boldsymbol{H})^{-1} \boldsymbol{H}^T \boldsymbol{R}^{-1} \tag{2.79}$$

This can then be used to determine the covariance matrix. Note that $\boldsymbol{\Lambda}$ is symmetric.

$$\begin{aligned}
\boldsymbol{P}_k &= [(\boldsymbol{H}^T \boldsymbol{R}^{-1} \boldsymbol{H})^{-1} \boldsymbol{H}^T \boldsymbol{R}^{-1}] \boldsymbol{R} [(\boldsymbol{H}^T \boldsymbol{R}^{-1} \boldsymbol{H})^{-1} \boldsymbol{H}^T \boldsymbol{R}^{-1}]^T \\
&= [(\boldsymbol{H}^T \boldsymbol{R}^{-1} \boldsymbol{H})^{-1} \boldsymbol{H}^T \boldsymbol{R}^{-1}] \boldsymbol{R} [\boldsymbol{R}^{-1} \boldsymbol{H} (\boldsymbol{H}^T \boldsymbol{R}^{-1} \boldsymbol{H})^{-1}] \\
&= (\boldsymbol{H}^T \boldsymbol{R}^{-1} \boldsymbol{H})^{-1} (\boldsymbol{H}^T \boldsymbol{R}^{-1} \boldsymbol{H}) (\boldsymbol{H}^T \boldsymbol{R}^{-1} \boldsymbol{H})^{-1}
\end{aligned}$$

$$\boldsymbol{P}_k = (\boldsymbol{H}^T \boldsymbol{R}^{-1} \boldsymbol{H})^{-1} \tag{2.80}$$

And the estimate is given by:

$$\hat{x}_k = (\boldsymbol{H}^T \boldsymbol{R}^{-1} \boldsymbol{H})^{-1} \boldsymbol{H}^T \boldsymbol{R}^{-1} \vec{y} \tag{2.81}$$

This development does in fact produce the linear, unbiased, minimum variance estimate of the state at time t_k, but does not allow for the inclusion of *a priori* state information. The method can be expanded through a similar procedure to include this essential component. The *a priori* state estimate is given as the following:

$$\hat{x}_a = \vec{x}_k + \vec{w}, \tag{2.82}$$

where $\vec{w}$ is a zero mean random vector with known covariance $E[\vec{w}\vec{w}^T] = \boldsymbol{Q}$. This random vector is assumed to be uncorrelated with the measurement error $\vec{\nu}$. Now, With this, the estimate can be rewritten as a linear combination of the measurements ($\vec{y}$) and the *a priori* state knowledge:

$$\hat{x}_k = \boldsymbol{M} \vec{y} + \boldsymbol{N} \hat{x}_a \tag{2.83}$$

Just as in the previous case, this can be expanded, and the unbiased condition given in Equation 2.72 can be applied.

$$\begin{aligned}
\hat{x}_k &= \boldsymbol{M}(\boldsymbol{H}\vec{x}_k + \vec{\nu})+] = \boldsymbol{N}(\vec{x}_k + \vec{w}) \\
&= (\boldsymbol{MH} + \boldsymbol{N})\vec{x}_k + \boldsymbol{M}\vec{\nu} + \boldsymbol{N}\vec{w} \\
E[\hat{x}_k] &= (\boldsymbol{MH} + \boldsymbol{N})E[\vec{x}_k] + \boldsymbol{M}E[\vec{\nu}] + \boldsymbol{N}E[\vec{w}] \\
\vec{x}_k &= (\boldsymbol{MH} + \boldsymbol{N})\vec{x}_k
\end{aligned}$$

$$\boldsymbol{MH} + \boldsymbol{N} = \boldsymbol{I} \tag{2.84}$$

This can then be used to express the error covariance as a function of $\boldsymbol{M}$ and $\boldsymbol{N}$.

$$\begin{aligned}
\boldsymbol{P}_k &= E[(\vec{x}_k - \hat{x}_k)(\vec{x}_k - \hat{x}_k)^T] \\
&= E[(\vec{x}_k - (\boldsymbol{MH} + \boldsymbol{N})\vec{x}_k - \boldsymbol{M}\vec{\nu} - \boldsymbol{N}\vec{w})(\vec{x}_k - (\boldsymbol{MH} + \boldsymbol{N})\vec{x}_k - \boldsymbol{M}\vec{\nu} - \boldsymbol{N}\vec{w})^T] \\
&= E[(-\boldsymbol{M}\vec{\nu} - \boldsymbol{N}\vec{w})(-\boldsymbol{M}\vec{\nu} - \boldsymbol{N}\vec{w})^T] \\
&= \boldsymbol{M}E[\vec{\nu}\vec{\nu}^T]\boldsymbol{M}^T + \boldsymbol{N}E[\vec{w}\vec{w}^T]\boldsymbol{N}^T
\end{aligned}$$

$$\boldsymbol{P}_k = \boldsymbol{MRM}^T + \boldsymbol{NQN}^T \tag{2.85}$$

Using Lagrange multipliers, as in the previous case and applying the constraint found above, the optimal $\boldsymbol{M}$ and $\boldsymbol{N}$ can be found:

$$\begin{aligned}
\boldsymbol{P}_k &= \boldsymbol{MRM}^T + \boldsymbol{NQN}^T + \boldsymbol{\Lambda}^T(\boldsymbol{I} - \boldsymbol{MH} - \boldsymbol{N})^T + (\boldsymbol{I} - \boldsymbol{MH} - \boldsymbol{N})\boldsymbol{\Lambda} \\
\nabla_{\boldsymbol{M}}\boldsymbol{P}_k &= \boldsymbol{RM}^T + \boldsymbol{MR} - \boldsymbol{\Lambda}^T\boldsymbol{H}^T - \boldsymbol{H}\boldsymbol{\Lambda} \\
&= (\boldsymbol{RM}^T\boldsymbol{H}\boldsymbol{\Lambda}) + (\boldsymbol{RM}^T\boldsymbol{H}\boldsymbol{\Lambda})^T = \boldsymbol{0} \\
\nabla_{\boldsymbol{N}}\boldsymbol{P}_k &= \boldsymbol{QN}^T + \boldsymbol{NQ} - \boldsymbol{\Lambda}^T - \boldsymbol{\Lambda} \\
&= (\boldsymbol{QN}^T\boldsymbol{\Lambda}) + (\boldsymbol{QN}^T\boldsymbol{\Lambda})^T = \boldsymbol{0}
\end{aligned}$$

These constraint equations, along with Equation 2.84 provide the optimal solution for the minimum variance estimator:

$$\boldsymbol{M} = \boldsymbol{\Lambda}^T\boldsymbol{H}^T\boldsymbol{R}^{-1} \tag{2.86}$$

$$\boldsymbol{N} = \boldsymbol{\Lambda}^T\boldsymbol{Q}^{-1} \tag{2.87}$$

$$\boldsymbol{\Lambda}^T\boldsymbol{H}^T\boldsymbol{R}^{-1}\boldsymbol{H} + \boldsymbol{\Lambda}^T\boldsymbol{Q}^{-1} = \boldsymbol{I}$$
$$\boldsymbol{\Lambda}^T(\boldsymbol{H}^T\boldsymbol{R}^{-1}\boldsymbol{H} + \boldsymbol{Q}^{-1}) = \boldsymbol{I}$$

$$\boldsymbol{\Lambda}^T = (\boldsymbol{H}^T\boldsymbol{R}^{-1}\boldsymbol{H} + \boldsymbol{Q}^{-1})^{-1} \tag{2.88}$$

$$\boldsymbol{M} = (\boldsymbol{H}^T\boldsymbol{R}^{-1}\boldsymbol{H} + \boldsymbol{Q}^{-1})^{-1}\boldsymbol{H}^T\boldsymbol{R}^{-1} \tag{2.89}$$
$$\boldsymbol{N} = (\boldsymbol{H}^T\boldsymbol{R}^{-1}\boldsymbol{H} + \boldsymbol{Q}^{-1})^{-1}\boldsymbol{Q}^{-1}. \tag{2.90}$$

Substituting these values back into the estimate and covariance equation provides:

$$\hat{x}_k = (\boldsymbol{H}^T\boldsymbol{R}^{-1}\boldsymbol{H} + \boldsymbol{Q}^{-1})^{-1}(\boldsymbol{H}^T\boldsymbol{R}^{-1}\vec{y} + \boldsymbol{Q}^{-1}\hat{x}_a) \tag{2.91}$$
$$\boldsymbol{P}_k = (\boldsymbol{H}^T\boldsymbol{R}^{-1}\boldsymbol{H} + \boldsymbol{Q}^{-1})^{-1} \tag{2.92}$$

2.4.2 Non-Linear Least Squares using LUMVE

With a method to determine the minimum variance estimate using *a priori* state knowledge and a set of measurements, a least squares procedure can be developed for improving the state estimate found using the classical orbit determination technique. This procedure is valid for any number of measurements and provides the minimum variance estimate for the associated measurement set. A few important notes before developing this method. First, the dynamic system described by Equation 2.7 are continuous and nonlinear. Second, the angular measurements are a nonlinear continuous function of the state, taken at discrete intervals. This provides the following:

$$\begin{aligned} \dot{\vec{x}}(t) &= f(\vec{x}(t)) \\ \vec{y_i} &= h(\vec{x}(t_i)) + \nu_i \end{aligned} \tag{2.93}$$

where ν_i is Gaussian white noise ($E[\nu_i] = 0$, $E[\nu_i\nu_j] = R_{ii}\delta_{i,j}$). The standard least squares procedure and the LUMVE equations are capable of providing an analytical solution for linear systems. In the case of nonlinear systems, a linearization procedure is conducted iteratively until satisfactory results are produced. For this procedure, a

reference trajectory is defined, which can be used to generate a reference measurement set:

$$\begin{aligned} \dot{\vec{x}}^*(t) &= f(\vec{x}^*(t)) \\ \vec{y}_i^* &= h(\vec{x}^*(t_i)). \end{aligned} \tag{2.94}$$

This provides the following deviation equations:

$$\begin{aligned} \delta\vec{x}(t) &= \vec{x}(t) - \vec{x}^*(t) \\ \delta\vec{y}_i &= \vec{y}_i - \vec{y}_i^*. \end{aligned} \tag{2.95}$$

Using a first order Taylor series, and the state transition matrix to descritize the dynamics, the deviation equations are given as follows:

$$\delta\vec{x}_i = \boldsymbol{\Phi}(t_i, t_k)\delta\vec{x}_k \tag{2.96}$$

$$\delta\vec{y}_i = \widetilde{\boldsymbol{H}}(\vec{x}(t_i))\delta\vec{x}(t_i) + \vec{\nu}_i. \tag{2.97}$$

The first order deviation equations are in the same form as the LUMVE solution was developed for. This allows for the estimation of the deviation from the reference trajectory:

$$\hat{x}_k = (\boldsymbol{H}^T\boldsymbol{R}^{-1}\boldsymbol{H} + \boldsymbol{Q}^{-1})^{-1}(\boldsymbol{H}^T\boldsymbol{R}^{-1}\delta\vec{y} + \boldsymbol{Q}^{-1}\delta\hat{x}_k) \tag{2.98}$$

$$\boldsymbol{P}_k = (\boldsymbol{H}^T\boldsymbol{R}^{-1}\boldsymbol{H} + \boldsymbol{Q}^{-1})^{-1} \tag{2.99}$$

where the measurements are expressed compactly in matrix form as:

$$\delta\hat{x}_k = \hat{x}_k - \vec{x}^*(t_k) \tag{2.100}$$

$$\delta\vec{y} = \begin{bmatrix} \vec{y}_1 - h(\vec{x}^*(t_1)) \\ \vec{y}_2 - h(\vec{x}^*(t_2)) \\ \vdots \\ \vec{y}_n - h(\vec{x}^*(t_n)) \end{bmatrix} \quad \boldsymbol{H} = \begin{bmatrix} \widetilde{\boldsymbol{H}}(\vec{x}^*(t_1))\boldsymbol{\Phi}(t_1, t_k) \\ \widetilde{\boldsymbol{H}}(\vec{x}^*(t_2))\boldsymbol{\Phi}(t_2, t_k) \\ \vdots \\ \widetilde{\boldsymbol{H}}(\vec{x}^*(t_n))\boldsymbol{\Phi}(t_n, t_k) \end{bmatrix} \quad \boldsymbol{R} = \begin{bmatrix} \boldsymbol{R}_{11} & \boldsymbol{0} & \dots \\ \boldsymbol{0} & \boldsymbol{R}_{22} & \dots \\ \vdots & \vdots & \ddots \end{bmatrix}.$$

Each $\boldsymbol{R}_{ii}$ is a square, diagonal matrix with dimension equal to the length of $\vec{y}_i$, or the number of measurements at each instant t_i. In the case of angles, this is two (right ascension and declination).

The LUMVE update is applied iteratively until a sufficiently small update is produced. Within this iterative solution, the terms in $\delta\vec{y}$ and $\boldsymbol{H}$ must be accumulated, which requires numerical integration from one time index to the next along the reference trajectory. The accumulation step can be accomplished more efficiently using the following notation:

$$\boldsymbol{\Lambda}^{-1}\hat{x}_k = \boldsymbol{\lambda} \tag{2.101}$$

$$\boldsymbol{\lambda} = \boldsymbol{H}^T\boldsymbol{R}^{-1}\delta\vec{y} + \boldsymbol{Q}^{-1}\delta\hat{x}_k \tag{2.102}$$

$$\boldsymbol{\Lambda}^{-1} = \boldsymbol{H}^T\boldsymbol{R}^{-1}\boldsymbol{H} + \boldsymbol{Q}^{-1}. \tag{2.103}$$

Each of these can be computed in the accumulation loop as the following:

$$\boldsymbol{\lambda} = \boldsymbol{Q}^{-1}\delta\hat{x}_k + \sum_{i=1}^{m}\left[\widetilde{\boldsymbol{H}}(\vec{x}^*(t_i))\boldsymbol{\Phi}(t_i,t_k)\right]^T\boldsymbol{R}_{ii}^{-1}\left[\vec{y}_i - h(\vec{x}^*(t_i))\right] \tag{2.104}$$

$$\boldsymbol{\Lambda}^{-1} = \boldsymbol{Q}^{-1} + \sum_{i=1}^{m}\left[\widetilde{\boldsymbol{H}}(\vec{x}^*(t_i))\boldsymbol{\Phi}(t_i,t_k)\right]^T\boldsymbol{R}_{ii}^{-1}\left[\widetilde{\boldsymbol{H}}(\vec{x}^*(t_i))\boldsymbol{\Phi}(t_i,t_k)\right]. \tag{2.105}$$

Which completes the derivation for all needed equations to implement the non-linear least squares batch estimator.

2.4.3 Implementation of Non-Linear Least Squares to the Orbit Determination Problem

With the statistical method to determine a minimum variance estimate, and an iterative procedure to to solve the non-linear least squares problem, everything can be brought together to improve the classical orbit determination solution using follow-up observations. In Cartesian space, the desired state is given as:

$$\vec{x} = \begin{bmatrix} x & y & z & \dot{x} & \dot{y} & \dot{z} \end{bmatrix}^T. \tag{2.106}$$

In the case of ground based optical observations azimuth and elevation angles are observed, which are directly converted to topocentric equatorial, which are given in Equation 2.41. These are nonlinear functions of the state which yields:

$$\begin{aligned}\vec{y}_i &= \begin{bmatrix}\alpha_i & \delta_i\end{bmatrix} \\ &= \begin{bmatrix}\tan^{-1}\left(\frac{y_i - Y_{obs}}{x_i - X_{obs}}\right) & \sin^{-1}\left(\frac{z_i - Z_{obs}}{\rho_i}\right)\end{bmatrix},\end{aligned} \tag{2.107}$$

where X_{obs}, Y_{obs}, Z_{obs} is the observer position in Cartesian space. The method to acquire this was produced in the previous section, and is independent of the objects position. To use the non-linear least squares procedure, the Jacobian of the measurement function is needed.

$$\boldsymbol{H} = \begin{bmatrix}\frac{\partial\alpha}{\partial x} & \frac{\partial\alpha}{\partial y} & \frac{\partial\alpha}{\partial z} & \frac{\partial\alpha}{\partial \dot{x}} & \frac{\partial\alpha}{\partial \dot{y}} & \frac{\partial\alpha}{\partial \dot{z}} \\ \frac{\partial\delta}{\partial x} & \frac{\partial\delta}{\partial y} & \frac{\partial\delta}{\partial z} & \frac{\partial\delta}{\partial \dot{x}} & \frac{\partial\delta}{\partial \dot{y}} & \frac{\partial\delta}{\partial \dot{z}}\end{bmatrix} \tag{2.108}$$

$$\begin{aligned}\frac{\partial\alpha}{\partial x}_i &= -\frac{y_i - Y_{obs}}{(x_i - X_{obs})^2 + (y_i - Y_{obs})^2} \\ \frac{\partial\alpha}{\partial y}_i &= \frac{x_i - X_{obs}}{(x_i - X_{obs})^2 + (y_i - Y_{obs})^2} \\ \frac{\partial\alpha}{\partial z}_i &= 0 \\ \frac{\partial\alpha}{\partial \vec{v}}_i &= \vec{0}\end{aligned} \tag{2.109}$$

$$\begin{aligned}\frac{\partial\delta}{\partial x}_i &= -\frac{(x_i - X_{obs})(z_i - Z_{obs})}{\rho^2\sqrt{(x_i - X_{obs})^2 + (y_i - Y_{obs})^2}} \\ \frac{\partial\delta}{\partial y}_i &= -\frac{(y_i - Y_{obs})(z_i - Z_{obs})}{\rho^2\sqrt{(x_i - X_{obs})^2 + (y_i - Y_{obs})^2}} \\ \frac{\partial\delta}{\partial z}_i &= \frac{\sqrt{(x_i - X_{obs})^2 + (y_i - Y_{obs})^2}}{\rho^2} \\ \frac{\partial\delta}{\partial \vec{v}}_i &= \vec{0}\end{aligned} \tag{2.110}$$

Now, assuming the observed objects motion is governed by Equation 2.7, linearized state matrix, can be derived.

$$\boldsymbol{A} = \frac{\partial \dot{\vec{x}}}{\partial \vec{x}} = \begin{bmatrix} \mathbf{0} & \boldsymbol{I} \\ \boldsymbol{A}_{21} & \mathbf{0} \end{bmatrix} \tag{2.111}$$

$$\boldsymbol{A}_{21} = \begin{bmatrix} -\frac{\mu}{r^3} + \frac{3\mu x^2}{r^5} & \frac{3\mu xy}{r^5} & \frac{3\mu xz}{r^5} \\ \frac{3\mu xy}{r^5} & -\frac{\mu}{r^3} + \frac{3\mu y^2}{r^5} & \frac{3\mu yz}{r^5} \\ \frac{3\mu xz}{r^5} & \frac{3\mu yz}{r^5} & -\frac{\mu}{r^3} + \frac{3\mu z^2}{r^5} \end{bmatrix} \tag{2.112}$$

Where $\boldsymbol{I}$ is a 3×3 identity matrix, and the $\boldsymbol{A}$ matrix is 6×6. This matrix can be used to propagate the state transition matrix along with the reference trajectory during the accumulation loop. The differential equation governing this is given by:

$$\dot{\boldsymbol{\Phi}}(t_i, t_j) = \boldsymbol{A}\boldsymbol{\Phi}(t_i, t_j) \tag{2.113}$$

This allows for the state transition matrix to be determined at any time, knowing that $\boldsymbol{\Phi}(t_i, t_i) = \boldsymbol{I}$. So, starting from t_0, the reference trajectory and state transition matrix are propagated from the estimated initial conditions and the identity matrix. This is all that is required to conduct the orbit improvement step. The $\boldsymbol{R}$ matrix varies by sensor and must be acquired empirically. To conclude the following steps are conducted over a finite set of iterations to estimate the initial position:

1. Conduct classical OD method on three observations from set: $(\vec{y}_i,\ t_i);\ i \in \{0, 1, 2, ...n\},\ n \geqslant 3$.

2. Back propagate the classical OD output from the middle point to the t_0. This initializes the reference trajectory $\vec{x}_0^*$.

3. Initialize the deviation $(\delta\vec{x}_0)$ and error covariance (P_0). Set $n = 1$ to begin the iteration loop.

   (a) Set $l = 1$ and initialize the accumulation loop

$$t_{l-1} = t_0 \qquad \vec{x}^*(t_{l-1}) = \vec{x}_0^*$$

$$\boldsymbol{\lambda} = \boldsymbol{P}_0^{-1}\delta\vec{x}_0 \qquad \boldsymbol{\Lambda} = \boldsymbol{P}_0^{-1}$$

where $\boldsymbol{\lambda} = \boldsymbol{\Lambda} = \mathbf{0}$ for $n = 1$. This is because there is no prior estimate for $n = 1$.

i. Numerically integrate reference trajectory and state transition matrix from $t_{l-1} \longrightarrow t_l$, providing $\vec{x}^*(t_l)$ and $\boldsymbol{\Phi}(t_l,\, t_{l-1})$.

ii. Compute the reference measurement function $h(\vec{x}^*(t_l))$ and measurement Jacobian $\widetilde{\boldsymbol{H}}(\vec{x}^*(t_l))$.

iii. Accumulate $\boldsymbol{\lambda}$ and $\boldsymbol{\Lambda}$ using Equations 2.104 and 2.105.

iv. Iterate over all l.

(b) Solve for the minimum variance estimate: $\delta\hat{x}_0 = \boldsymbol{\Lambda\lambda}$ and the covariance $P_0 = \Lambda$.

(c) If the process has converged to specified tolerance, exit the iteration loop. If not, $n = n + 1$, and update with the following:

$$\vec{x}_0^* = \vec{x}_0^* + \delta\hat{x}_0$$

To follow, a numerical demonstration of this algorithm will be conducted.

2.5 Two-Line Elements

There exist a small number of publicly available satellite catalogs, the most accessible of which is published by the United States Strategic Command (USSTRATCOM) [3]. The catalog is composed of several thousand two-line element sets (TLE's). A TLE contains information required to identify and propagate a satellite position using the Simplified General Perturbation model (SGP, SGP4, SDP4, SGP8, SDP8) [29]. Figure 2.5 shows the format of a TLE. Data is compiled into two lines each 69 characters in length. The TLE includes the following, separated by spaces:

1. Line 1

```
0 AMAZONAS 3
1 39078U 13006A   20031.50216022 -.00000276 +00000-0 +00000-0 0  9997
2 39078 000.0540 254.1823 0003221 025.5482 330.2171 01.00274256021532
```

Figure 2.5.. Two-line element for Amazonas 3, international designator 13006A. This object is in a geostationary orbit and was the sixth catalog entry of 2013, given by the international designator.

(a) Line number

(b) Satellite catalog number

(c) International designator

(d) Observation epoch

i. First two digits are the year

ii. Remaining digits are the day (with ten significant figures for time)

(e) First derivative of the mean motion (rev/day / 2)

(f) Second derivative of the mean motion (rev/day2 / 6)

(g) Bstar (Adjusted ballistic coefficient)

(h) Ephemeris time (internal use only, should always be zero)

(i) Element set number

(j) Checksum

2. Line 2

(a) Line number

(b) Satellite catalog number

(c) Inclination (degrees)

(d) Right ascension of the ascending node (degrees)

(e) Eccentricity

(f) Argument of perigee (degrees)

(g) Mean Anomaly (degrees)

(h) Mean Motion (rev / day) (11 digits), revolution number at epoch (5 digits), and checksum (1 digit)

Note that the TLE does not contain any statistical information, so there is no way to quantify the certainty in this information. TLE's are not all equally accurate [10], as some objects are affected more significantly by non-conservative perturbations [30,31]. Additionally some objects are not regularly observable, leaving large gaps between TLE epoch's.

2.6 Simulated Observation Scenario

To conclude the background material, the developments made up to this point can be rigorously applied in a simulated observation scenario of two satellite's using their respective TLE's. Simulated observations are to be made from an observation site in West Lafayette, Indiana ($\varphi = 40.4259^\circ\, N,\ \lambda = 86.9081^\circ\, W,\ h = 187\, m$) on the date of March 25^{th}, 2020.

Two objects have been selected for observation in this scenario. The first is Amazonas 3, which has a TLE shown in Figure 2.5. Amazonas 3 is an active communication satellite located in the 61° W orbital position in GEO. The second is the Ariane 5 Rocket Body jettisoned while Amazonas 3 was in transit to GEO. That leaves the rocket body in GTO with a relatively high eccentricity of 0.7214235, according to the TLE. Both TLE's are included below for in Figure 2.6. Note that both objects are from the same launch vehicle, indicated by the "A" and "C" suffix in the international designator.

Each TLE is back propagated to the designated starting epoch (11:00 AM March 25^{th}, 2020), which are each used as the truth value for $\vec{x}_0$ in this simulation. Using this, the true value is propagated forward using SGP4 to produce a time history of the motion in twenty second time intervals for an arbitrary length of time. Knowing the station and satellite locations at each time, the relative position vector can be

```
0 AMAZONAS 3
1 39078U 13006A   20085.06577149 -.00000290  00000-0  00000+0 0  9992
2 39078   0.0352 229.1912 0001485 111.0412 165.4397  1.00272285 26159
0 ARIANE 5 R/B
1 39080U 13006C   20085.13906902  .00000221  00000-0  14775-3 0  9997
2 39080   6.1925 267.2968 7214235 189.7331 139.0742  2.34857339 60311
```

Figure 2.6.. TLEs for Amazonas 3 and Ariane 5 Rocket Body to be used in the simulated observation scenario. TLEs were taken from [3] on 3/26/2020.

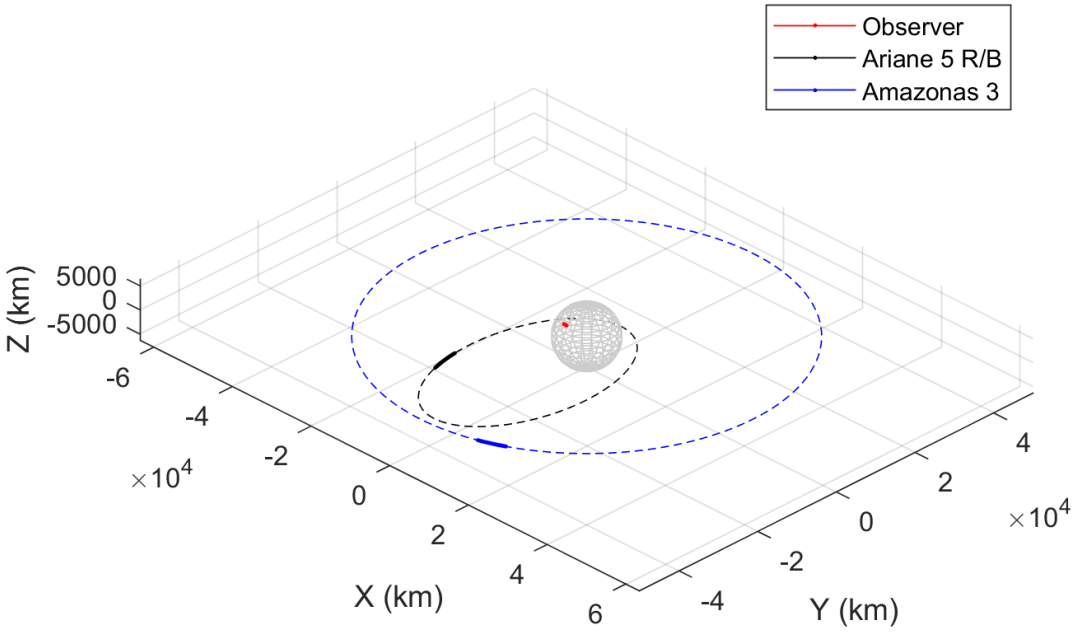

Figure 2.7.. Amazonas 3 and Ariane 5 Rocket Body orbits propagated over a 30 minute observation series (solid line) and for one full orbit (dotted line). Observer location shown on the surface of Earth at each observation time in red.

found and Equation 2.41 can be used to produce the noiseless angular measurements. Gaussian noise can then be added to each measurement ($\sigma = 2.5$ arcseconds in both right ascension and declination) to create simulated measurements. Figure 2.7 shows each object's orbit, and the arc traversed during the 30 minute simulated observation scenario.

Table 2.1.. Initial conditions from Each TLE at epoch of 11:00 March 25, 2020.

	x_0 (km)	y_0 (km)	z_0 (km)	$\dot{x}_0$ (km/s)	$\dot{y}_0$ (km/s)	$\dot{z}_0$ (km/s)
Amazonas 3	12593	-40236	38.33	2.9345	0.91885	0.000937
Ariane 5 R/B	-14213	-19270	-1430.1	0.51755	-4.0355	0.078448

With the simulated measurements the orbit determination procedure outlined thus far can be applied. First, Laplace's method is applied using the first, middle, and last observation made in the series. The solution provides the state at the middle observation, which is back propagated to provide an estimate of the initial state. It will be shown that this provides an adequate first guess in these cases, but an improvement is needed. For this reason, it is used to initialize the nonlinear least squares procedure.

Four observation series of length: 10 min, 30 min, 45 min, and 60 min, are tested on each object with 20 second spacing between measurements. The state estimates for each object given each observation scenario are presented in Tables 2.2 and 2.3. The least-squares orbit improvement step, conducted after the IOD, consistently provides a better result for the position and velocity estimate. The estimates deviation from the true state values and the associated error bounds are provided in Tables 2.4 and 2.5. The standard deviation of each state (given as the square root of the i^{th} diagonal element of $\boldsymbol{P}_0$) decreases with more measurements. This means that over a longer observation series, the confidence in the state estimate increases. This is intuitive, because as more measurements that agree with the estimate are incorporated, the

certainty in said estimate increases. The component-wise deviations in the state estimate from the truth values fall within the 3σ bounds given in the covariance matrix. This is to be expected, as the estimate has a 99.7% likelihood of falling within the 3 standard deviations of the mean. The orbit prediction given Laplace's method and post-improvement are given in Figures 2.8 and 2.9 for the 30 minute observation series.

Table 2.2.. Results for Laplace IOD and orbit improvement using nonlinear least squares over 4 different observation sets of Amazonas 3.

		x (km)	y (km)	z (km)	$\dot{x}$ (km/s)	$\dot{y}$ (km/s)	$\dot{z}$ (km/s)	Δr (km)	Δv (km/s)
10 Minute	Laplace IOD	12137	-38811	84.067	2.8424	0.85583	-0.00098	1496.7	0.11162
	Orbit Improvement	12715	-40558	-0.17211	2.9453	0.95773	0.004259	347.02	0.040485
30 Minute	Laplace IOD	12507	-39785	-32.25	2.9022	0.90529	0.001064	464.02	0.035081
	Orbit Improvement	12598	-40247	36.739	2.9335	0.92263	0.001489	12.684	0.003936
45 Minute	Laplace IOD	12638	-40118	-72.358	2.9237	0.91581	0.000368	167.31	0.011216
	Orbit Improvement	12575	-40188	43.726	2.9317	0.916	0.00101	50.845	0.003988
60 Minute	Laplace IOD	12586	-39959	-54.085	2.9141	0.90179	-8.88E-05	291.76	0.026631
	Orbit Improvement	12574	-40185	44.149	2.9316	0.91566	0.000973	54.585	0.004316

Table 2.3.. Results for Laplace IOD and orbit improvement using nonlinear least squares over 4 different observation sets of Ariane 5 R/B.

		x (km)	y (km)	z (km)	$\dot{x}$ (km/s)	$\dot{y}$ (km/s)	$\dot{z}$ (km/s)	Δr (km)	Δv (km/s)
10 Minute	Laplace IOD	-14097	-19016	-1497.2	0.50257	-4.0174	0.079489	287.18	0.023543
	Orbit Improvement	-14203	-19259	-1426	0.52503	-4.0251	0.081414	15.07	0.013156
30 Minute	Laplace IOD	-14081	-18957	-1498.2	0.5017	-4.0567	0.086629	346.48	0.027645
	Orbit Improvement	-14209	-19266	-1428.7	0.52058	-4.0323	0.079647	5.5261	0.004588
45 Minute	Laplace IOD	-14075	-18867	-1507.8	0.50285	-4.0973	0.09392	433.13	0.065351
	Orbit Improvement	-14210	-19267	-1428.9	0.51977	-4.0337	0.079296	4.9333	0.003013
60 Minute	Laplace IOD	-14013	-18668	-1500.1	0.49536	-4.138	0.10005	638.51	0.10704
	Orbit Improvement	-14208	-19265	-1428.3	0.51972	-4.0333	0.079314	7.2044	0.003233

Table 2.4.. Component-wise deviation from true trajectory and 3σ bounds of each dimension for Amazonas 3.

		x (km)	y (km)	z (km)	$\dot{x}$ (km/s)	$\dot{y}$ (km/s)	$\dot{z}$ (km/s)
10 Minute	$\Delta\vec{x}_i$	122.16	322.52	38.502	0.010788	0.038879	0.003321
	$3\sigma_i$	2707	7155.2	850.79	0.49173	0.30124	0.014195
30 Minute	$\Delta\vec{x}_i$	4.5461	11.734	1.5917	0.000967	0.003775	0.000552
	$3\sigma_i$	175.43	463.55	54.843	0.030038	0.02337	0.000935
45 Minute	$\Delta\vec{x}_i$	17.925	47.274	5.3953	0.002787	0.002852	7.25E-05
	$3\sigma_i$	63.522	167.7	19.703	0.010296	0.0095	0.000357
60 Minute	$\Delta\vec{x}_i$	19.257	50.743	5.8186	0.002898	0.003198	3.56E-05
	$3\sigma_i$	31.331	82.582	9.6126	0.004773	0.005164	0.00019

Table 2.5.. Component-wise deviation from true trajectory and 3σ bounds of each dimension for Ariane 5 R/B.

		x (km)	y (km)	z (km)	$\dot{x}$ (km/s)	$\dot{y}$ (km/s)	$\dot{z}$ (km/s)
10 Minute	$\Delta\vec{x}_i$	9.9759	10.521	4.1102	0.007486	0.010404	0.002966
	$3\sigma_i$	335.98	357.6	141.2	0.02427	0.11734	0.011698
30 Minute	$\Delta\vec{x}_i$	3.698	3.8474	1.4355	0.003035	0.003225	0.001199
	$3\sigma_i$	28.118	29.927	11.652	0.001783	0.008447	0.000907
45 Minute	$\Delta\vec{x}_i$	3.2663	3.477	1.2567	0.002227	0.001844	0.000848
	$3\sigma_i$	11.85	12.633	4.8327	0.000846	0.003149	0.000364
60 Minute	$\Delta\vec{x}_i$	4.7616	5.0708	1.8755	0.002174	0.00223	0.000866
	$3\sigma_i$	6.6551	7.1191	2.665	0.000556	0.00156	0.000196

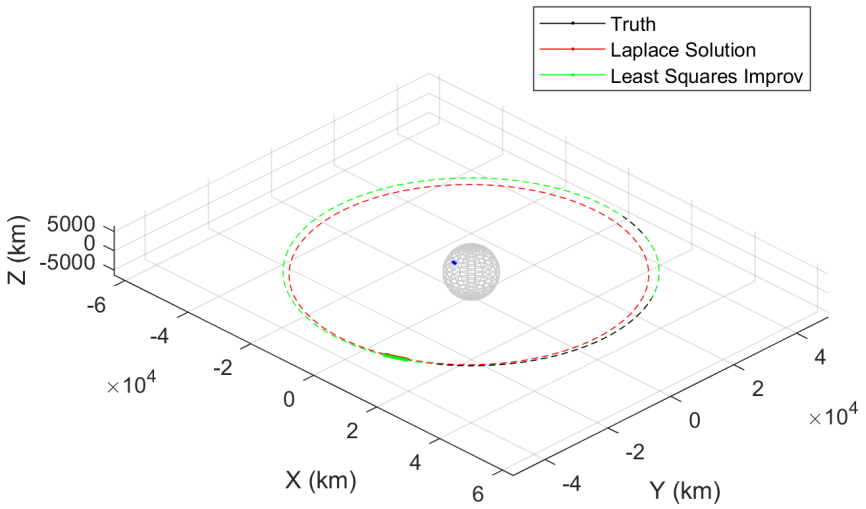

Figure 2.8.. True orbit, Laplace estimated orbit, and least squares improved estimate of orbit for the Amazonas 3 satellite given a 30 minute observation series.

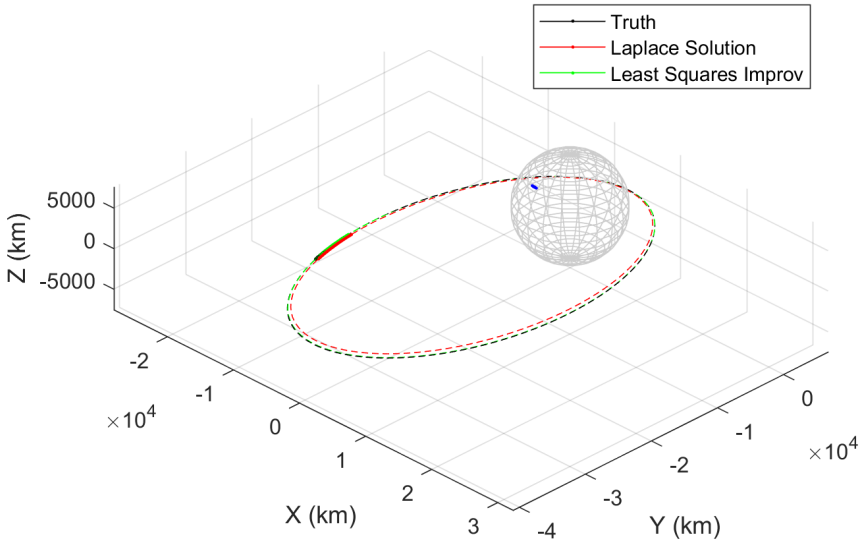

Figure 2.9.. True orbit, Laplace estimated orbit, and least squares improved estimate of orbit for the Ariane 5 R/B given a 30 minute observation series.

3. OBSERVATIONS AND THE PURDUE OPTICAL GROUND STATION

The focus of this study is on astrometry and orbit determination using ground based optical sensors. Before observations can be made, it is important to understand the signal environment, measurements being taken, and the instruments measurements are being taken with. The following is a review of the fundamental signal model for observation of passively illuminated objects, instrumentation used for observation, and utilized observation modes. The developments presented follow Reference [4] closely.

3.1 Fundamentals of Optical Sensors

3.1.1 Optical Signal

Electro-optical sensors are a class of sensors that measure the intensity of incident light rays. These light rays can originate from active illumination sources, such as stars, or can be reflected off of another body before being measured by the detector. These objects are called passively illuminated objects, as light from an active illumination source is not received directly, but rather reflected off of an otherwise non-radiating body. The irradiance of an observed passively illuminated object depends on how much light is incident to the reflective surface; which is dependant on how bright the source of illumination is. For Earth orbiting objects, this is the sun, which has an associated *radiant flux density* (I): the power emitted from a source, divided by the area over which the emitted power is spread. As the distance from the source becomes larger, the area it is spread over becomes larger, thus decreasing the radiant flux density. At 1 AU (mean Earth distance from the sun), the radiant

flux density can be integrated over the visible waveband to produce an average value of $I_{0,sun} = 1366.1 W/m^2$. The power emitted from the sun is not constant, and the distance of the Earth from the sun is not always 1 AU, so this only provides a nominal value.

When the radiant flux is incident to an opaque surface of area A, a portion of that signal is reflected. The expected radiant flux density resulting from reflection, received at a distance r from the surface is given by:

$$I_{obj}(\lambda) = \int I_{0\lambda,sun} \frac{A}{r^2} \Psi(\lambda) d\lambda \tag{3.1}$$

$$= I_{0,sun} \frac{A}{r^2} \Psi(\bar{\lambda}) \tag{3.2}$$

Ψ is called the reflection phase function, and accounts for the orientation of the surface with respect to the incident light from the sun, and the reflected light directed toward the observer, as well as surface material properties. λ is the wavelength of the incident light. The determination of the phase function for a given object is not a trivial task, as it is dependent on the shape and attitude of the object. Using light measurements to determine shape or attitude is an ongoing area of research [32–34]. The received radiant flux from the reflective surface can be used to determine the expected signal strength:

$$S_{obj} = \int (D - d) \frac{\lambda}{hc} e^{-\tau(\lambda) R(\zeta)} I_{obj}(\lambda) d\lambda \tag{3.3}$$

$$\approx (D - d) \frac{\bar{\lambda}}{hc} e^{-\tau(\bar{\lambda}) R(\zeta)} I_{obj}(\bar{\lambda}) \tag{3.4}$$

where D is the area of the aperture, d is the obstructed area of the aperture, h is Planck's constant, c is the speed of light, $\tau(\lambda)$ is the atmospheric extinction coefficient, R is the atmospheric function, which is a function of the zenith angle ζ. This signal strength is given in units of photons / second. The total number of photons caught by the sensor is given by the *count rate*, and is dependent on the exposure time, which is determined using the time integral:

$$E(S_{obj}) = \int S_{obj} Q(\lambda) dt \approx S_{obj} Q(\bar{\lambda}) \Delta t, \tag{3.5}$$

where Q is the quantum efficiency and is sensor dependent.

3.1.2 Measuring Optical Signals

The most common detector presently used in astronomy is the Charge-Coupled Device (CCD). This device is made up of a series of electrically isolated elements that collect charge. These elements are called pixels, and are arranged in a grid of arbitrary size $n \times n$, though it need not be square. As the pixels are illuminated over a finite amount of time, they collect incident photons, which causes the release of photo electrons. Once the collection is complete the pixels readout this analog photo electron count value, which is converted to some digital unit which is correlated to incident light intensity at the specified location on the pixel grid [12].

Light is directed onto the CCD using an optical assembly, which can be categorised as a *refractor* or a *reflector*. Refractor's use a series of lenses to focus light rays and produce an image. Because large lenses are sensitive, difficult to fabricate, and lose light due to the transit through the medium, reflectors are presently used for professional astronomy. Reflectors use mirrors to produce an image, typically a primary and a secondary. The first telescope of this kind was developed by Issac Newton in 1668; resulting in the configuration being named the Newtonian telescope [11]. Since then, several configurations have been popularized. The Cassegrain telescope is a popular configuration that has produced several sub-varieties. A general model for this configuration, and how it is used to direct light onto a CCD array is shown in Figure 3.1.

The telescope is directed at a specified portion of the sky, receiving an incident wavefront. In an idealized observations setting, the incident wavefront has a one-to-one correspondence to the celestial sphere. This incident wavefront passes through the optical assembly before being projected onto the CCD array. This relation between CCD coordinates and celestial sphere coordinates is the primary mode of astronometric observation. In this idealized observation setting, with idealized instruments, the map between the two is deterministic; in reality this is not the case. The portion of the celestial sphere being viewed on the CCD is called the *field of view*. The the-

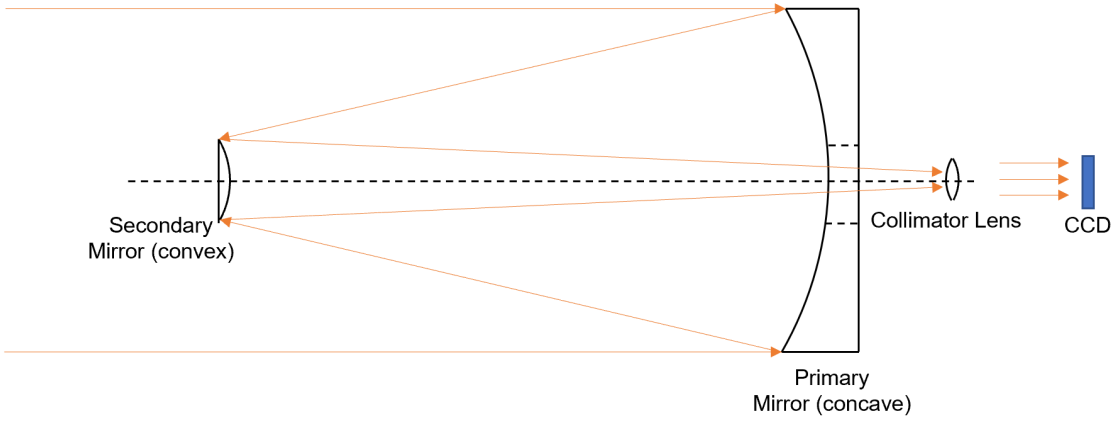

Figure 3.1.. General configuration of Cassegrain telescope. One concave primary mirror directs incident light onto a convex secondary mirror which then directs light through the eyepiece. Elements in the figure and their respective distances are not to scale.

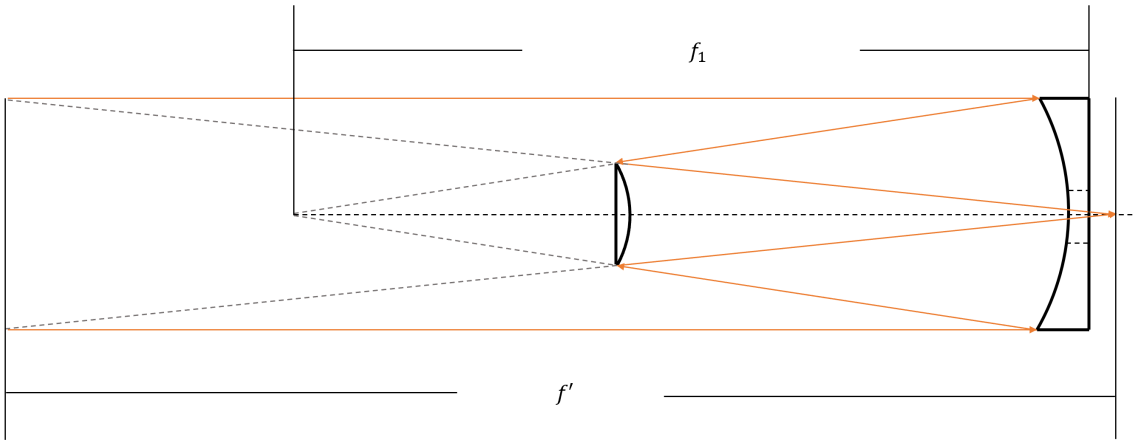

Figure 3.2.. The effective focal length (f') of a Cassegrain telescope is determined by the both the primary and the secondary mirrors. The focal length is oriented behind the collimator lens.

oretical field of view is a function of the focal length of the telescope and the CCD scale, and is given by:

$$FOV = 2\tan^{-1}\left(\frac{d}{2f'}\right) \tag{3.6}$$

where d is the dimension of the CCD array and f' is the effective focal length. Each optical component (primary and secondary mirror) has its own focal length. The combination of these two components, arranged in the configuration given in Figure 3.2 produces an instrument that has an associated effective focal length (f'). The Cassegrain telescope leverages this fact, producing a large effective focal length using relatively small optical components. The dimension of the CCD array can be taken as the horizontal, the vertical, or the diagonal. For most applications, the pixel grid is square of side length n uniformly sized pixels. The *pixel scale* (τ) is the angular coverage of a single pixel on the CCD. For a square pixel grid this is given as:

$$\tau = \frac{FOV}{n} = \frac{2}{n} \tan^{-1}\left(\frac{d_s}{2f'}\right), \tag{3.7}$$

where d_s is the side length of the pixel grid. It is common to see d_s and f' in millimeters. The resultant pixel scale is commonly given in arceconds / pixel, but this depends on the FOV and the number of pixels in the CCD.

3.1.3 Noise in Optical Observations

In reality, optical measurements are corrupted by noise from external stellar sources, charged particles from extraterrestrial and terrestrial sources, atmospheric conditions as the signal passes through the atmosphere, optical distortion in the optical assembly, and electronic noise in the CCD. Each of these sources makes a contribution to the electron count in a pixel, and ultimately the digital signal readout by the computer. If the contribution of these external light sources is of a similar magnitude to that of the source being observed, it is hard to isolate what the contribution from the observed sources is.

Starting with external light sources, the sun has the largest impact on the darkness of the sky. Astronomical sunset occurs at a sun elevation of -9°. Once the sun has set, the next brightest object in the sky is the moon. Observations within 15° of the moon halo can have background level contributions from moon light. The next brightest background source is: Zodiac light. This is the sunlight that is scattered by

the dust in the ecliptic. It is bright enough to see with the naked eye and appears as a large white triangle in the night sky oriented along the ecliptic. The values needed to determine the magnitude of its contribution can be found in lookup tables. Lastly, the contribution of light given by other stars and galactic sources in the night sky contribute to the observed celestial background level.

Two primary sources contribute to the background level of the image are due to the atmosphere. The first is airglow spectral radiation, which is the brightness of the atmosphere itself. The light is due to chemiluminescent reactions in the upper atmosphere. The second is atmospherically scattered light. This is the sum of terrestrially sourced light that is scattered by the atmosphere. These contributions are expected to vary little over the image, but do add to the overall background level.

The CCD itself has its own instrument noise. There exists a low level of current supplied through the detector, even when no incident photons are present. This is called dark current. The readout process requires that current be supplied; electrons provided for the readout process can contribute to the measurement. Lastly, as is the case with any analog to digital conversion, a truncation can be expected resulting in the loss of incident photons.

The brightness of a source with respect to the background sources is quantified by the Signal-to-Noise ratio (SNR). The SNR is given as the expected signal value divided by the standard deviation of the noise:

$$SNR = \frac{E\{S_{obj}\}}{\sigma_N}. \tag{3.8}$$

The objects signal is, in most cases, spread over n pixels. This means the objects total signal (S_{obj}) is the sum of its contribution over all n pixels. The background signal due to external sources over all n pixels is given as (S_b). The electron emittance after absorption, and in turn the object and background signals, can be modelled as a Poisson random variable. The variance of the readout noise, truncation effect, and dark current are given by N_R^2, N_U^2, N_D^2, respectively. The readout noise and truncation effect can be modeled as Gaussian random variables, while the contribution of the

dark current is modeled as a Poisson random variable. This results in the following, called the classical CCD equation:

$$SNR = \frac{S_{obj}}{\sqrt{S_{obj} + S_b + N_R^2 + N_U^2 + N_D^2}}. \tag{3.9}$$

3.2 Hardware and Observation Site

Optical observations for this study have been made at the Purdue Optical Ground Station (POGS), located at New Mexico Skies Observatory in Mayhill, New Mexico. The telescope is remotely operated from Armstrong Hall in West Lafayette, Indiana. The telescope uses a Corrected Dall-Kirkham optical assembly, which is a subcategory of Cassegrain. The optical assembly is mounted on a robotic German equatorial mount, allowing for remote operation. A 4096 × 4096, 16-bit, monochrome CCD camera is used to capture images. Observation times are recorded using the TM2000A time server, which maintains accurate time synchronization with GPS time. Relevant observatory specifications are provided in Table 3.1.

These values can be used to produce the expected field of view and pixel scale:

$$d_s = \sqrt{\frac{d^2}{2}} = \sqrt{\frac{52.1^2}{2}} \approx 36.8403 \tag{3.10}$$

$$FOV = 2\tan^{-1}\left(\frac{d_s}{2f'}\right) = 2\tan^{-1}\left(\frac{36.804}{2(2563)}\right) \approx 49.4129\ arcmin \tag{3.11}$$

$$\tau = \frac{FOV}{n} = \frac{0.8235}{4096} \approx 0.7238\ arcsec/pix \tag{3.12}$$

These are given as approximate values as they have been calculated using product specifications and not measurements of the hardware in use. The theoretical field of view and pixel scale also differ from that of the observed field of view and pixel scale based on observation conditions and temperature.

Each image is output as a FITS file, or Flexible Image Transport System, designed for multi-dimensional arrays such as images or tables. Each FITS file contains the image taken from the camera, as well as a table of observation data called the header.The FITS header contains information used to provide an astrometric solu-

Table 3.1.. Location of the POGS as well as relevant hardware specifications for the telescope being operated.

Parameter	**Value**	**Unit**
Latitude	32° 54' N	Deg : Min
Longitude	105° 32' W	Deg : Min
Altitude	2225	m
Aperture	356	mm
Effective Focal Length	2563	mm
Focal Ratio	7.2	
Central Obstruction by Area	23.5	Percent
CCD Diagonal	52.1	mm
Pixel Size	9	micron
Pixel Array	4096 × 4096	

tion, such as: observation time, exposure time, desired azimuth and elevation, and desired tracking rate.

3.3 Observation Scenarios

As discussed in Chapter 2, Two-Line Element sets provide information needed to propagate satellite state information over a reasonable window of time. If an observer would like to schedule an observation series of a specific satellite, the expected position of the satellite with respect to the observation site is required. Propagating the TLE to the desired observation time provides the observer with the expected satellite position and velocity. Knowing the observation location and time, the observers position and velocity in ECI can be determined using the Earth precession and nutation models

given in Chapter 2. This allows for the computation of the expected topocentric equatorial coordinates of the object as shown in Equation 2.41. This can then be converted to azimuth and elevation angles using Equation 2.45, which provides the observer with the pointing direction for the observation. Every observation site has obstructions in the local horizon that prevent observation. This restricts the allowable values for elevation as a function of azimuth to make observations. At the POGS the elevation mask varies between 10 and 25 degrees.

When using a CCD, a nonzero exposure time is required to collect incident light. This means that over the course of the exposure both the observer and the object being observed are in motion. If the pointing direction were to remain fixed in the local horizon over the exposure the signal received from imaged stars and satellites would be distributed over several pixels in a streaked pattern. For this reason, the azimuth and elevation can be varied over the exposure to maintain an objects position relative to the pointing direction. This is process is called tracking. The user requires a tracking rate $(\dot{A}, \dot{E})$ to accomplish this:

$$\rho = ||\vec{r}_{obj} - \vec{r}_{obs}||$$

$$\hat{l} = \frac{\vec{r}_{obj} - \vec{r}_{obs}}{\rho} = \begin{bmatrix} \cos(E)\cos(A) \\ \cos(E)\sin(A) \\ \sin(E) \end{bmatrix}$$

$$\frac{d}{dt}[\hat{l}] = \left[\rho(\vec{v}_{obj} - \vec{v}_{obs}) - \dot{\rho}(\vec{r}_{obj} - \vec{r}_{obs})\right]\frac{1}{\rho^2} \tag{3.13}$$

$$= \begin{bmatrix} -\sin(E)\cos(A)\dot{E} - \cos(E)\sin(A)\dot{A} \\ -\sin(E)\sin(A)\dot{E} + \cos(E)\cos(A)\dot{A} \\ \cos(E)\dot{E} \end{bmatrix} \tag{3.14}$$

$$= \begin{bmatrix} -\sin(E)\cos(A) & -\cos(E)\sin(A) \\ -\sin(E)\sin(A) & \cos(E)\cos(A) \\ 0 & \cos(E) \end{bmatrix} \begin{bmatrix} \dot{E} \\ \dot{A} \end{bmatrix} \tag{3.15}$$

$$\dot{\rho} = \frac{1}{2\rho}\Big[2(\vec{r}_{obj} - \vec{r}_{obs}) \cdot (\vec{v}_{obj} - \vec{v}_{obs})\Big]$$
$$= \hat{l} \cdot (\vec{v}_{obj} - \vec{v}_{obs}).$$

The matrix given in Equation 3.15 is rank 2, thus a unique solution for the tracking rate exists. For typical exposure times used in this study (6-8 seconds) the azimuth and elevation angle can be linearly varied with respect to time:

$$A(t) = \dot{A}(t - t_0) + A(t_0) \tag{3.16}$$

$$E(t) = \dot{E}(t - t_0) + E(t_0), \tag{3.17}$$

where t_0 is the time at the beginning of the exposure and t is the time at the end of the exposure.

Two tracking modes are used to adjust the pointing direction throughout the exposure to keep imaged objects in fixed pixel coordinates. The first is *sidereal tracking mode*, where the pointing direction is synced with the Earth's rotation such that the same portion of the celestial sphere is imaged over the full exposure. Over the time sale of the exposure, stars remain inertially fixed and as a result, appear as points in the image. Satellites would appear as streaks in this mode. The second is *satellite tracking mode*, where the pointing direction is synced with the motion of a particular satellite. In this mode the stars appear as streaks of length determined by the tracking rate, and the satellites appear as points on the CCD array. An accurate estimate of the satellites velocity is required to be able to achieve this. This mode is used almost exclusively in this study, as it is desirable to have as much signal from faint objects integrated over a small cell of pixels. This allows for a higher SNR per pixel, which results in a higher probability of detection.

The mount used at the POGS is integrated with software capable of determining required tracking rates. This allows the user to provide a TLE, specify observation times and obtain images of a desired object. As shown in Equation 3.13, the tracking rate is determined by the position and velocity of the object. This means that the accuracy of the tracking is highly dependent on the accuracy of the TLE data, which varies significantly by object.

4. IMAGE PROCESSING

Image processing is a crucial step in the object positioning procedure as it takes in raw instrument output and produces star and satellite position information. The user is provided with instrument output in the form of an $n \times n$ grid of pixel intensity values scaled based on hardware limitations. From this, the goal of the image processing step is to obtain the number of objects in frame, the location of these objects in the frame, and what type of object each one is. For this statement, and the remainder of the chapter the word *object* is assigned the more abstract definition: any pixel or a continuous group of pixels that has been marked given some criteria based on brightness or shape. It is important to note this distinction and it's disconnect from the physical definition of the word. An object picked up on frame does not necessarily have a physical counterpart in space, as it could be noise or a fault in the electronic system. Naturally, all pixels that are not associated with an object are a part of the *background*. The background is the base level by which it is determined if a pixel should be flagged as a detection.

Image processing has several steps that are described in detail below. The first of these steps is to obtain an estimate of the background level. With a background level determined, the image can be scanned for detections. If a pixel has an intensity level that is sufficiently large when compared to the background level, then it is marked as a detection. Once all detections have been found, adjacent pixels can be grouped to form objects and their shape can be used to determine if they are likely to be stars or an RSO.

4.1 Initial Background Determination

The first step is to determine the background level, or the intensity level of the frame when looking at the empty sky. The background is not uniform because of noise and other optical effects discussed in the previous section. There are several ways to go about doing this. The first and simplest would be to take the average intensity value across the whole frame. This does not provide good results because the mean is sensitive to outliers. Additionally, before the objects are detected in frame, the bright pixels that will later be detected will drive up the mean. Another way to proceed would be to take the median of all of the values on frame. This is better than the mean, but does not provide any information about the variance. This makes it hard to define how much deviation is required to qualify a pixel as a detection. One way to get around this is to select a specified number of pixels around the median and use the mean and variance of these pixel intensities to determine a background level. This would not be sensitive to outliers like the mean filter would be, and would provide information to create a threshold with. This option has been shown to produce sufficient results, however is still sensitive to the uneven background levels throughout a single image. Thus a technique that divides the image into subframes is employed: the *median* & $sfrm$ algorithm. This method has been shown to produce good results in the initial estimation of the background [35].

The first step in the process of determining the background level is to divide the frame into m^2 subframes. Each subframe is given its own local background value, as it is incorrect to assume that the background is uniform across the entire field of view. Bright sources will diffuse into other adjacent pixels, thus raising the background level of the local field, creating bright pixels that we do not want incorporated into the object.

Each subframe is scanned with a square *swath* of specified pixel dimension. The mean value of each swath is taken, and the swath moves row-wise to the next unique set of pixels until the entire subframe is scanned. At this point the median of the

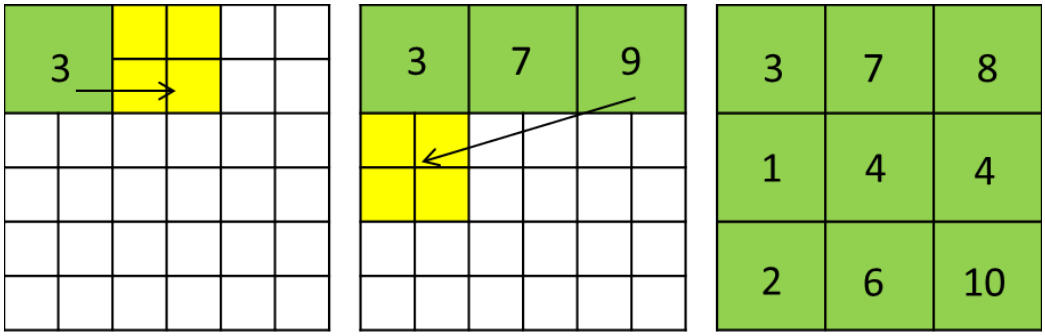

Figure 4.1.. The subframe shown above is scanned with a 2x2 pixel swath. The averaged value of the 4 pixels contained within the swath is stored before moving onto the next set of unique pixels. The background value of this subframe would be the median of all of the stored swath values, which in this case is 4.

mean swath values is determined. This value is then used as the background level of the subframe. Note that at this point, no detection's have been made, so all pixels are included in the process of determining the background level. What this means is that pixels that we know will be contained in objects are being included in the initial background determination. Ideally, the median operation will negate an overestimation, but more times than not, the background will need to be refined. What this translates to is, our first scan for objects will be conservative, as our approximated background value is higher than it is supposed to be. This will become clearer once detection criteria are defined.

4.2 Object Detection

Once the background level of each subframe has been approximated, the subframes can be scanned for objects. Each pixel in each subframe is scanned and run through the detection criteria, given by:

$$d(i) = b(i) + C\sigma(i), \quad i \in \{1, 2, ...m^2\} \tag{4.1}$$

Where *d(i)* is the detection threshold, *b(i)* is the background level and $\sigma(i)$ is the standard deviation of the i^{th} subframe. C is a user specified constant that allows the thresholding procedure to be tuned. The standard value for C is 2.0, but this can be tuned for a set of observations.

When a pixel's intensity is greater than *d(i)*, it is considered a detection. Detection's are stored in what is called a *Symbolic Image of Object (SIO)*. This is a binary array composed of detections as 1's and background pixels as 0's. This is written as:

$$SIO(x, y, i) = \begin{cases} 1 & p(x, y) > d(i) \\ 0 & else \end{cases},$$

where x and y are the pixel coordinates on the image, and *p(x,y)* is the pixel intensity value corresponding to the given pixel coordinates. Note that *(x,y)* $\rightarrow i$ for all $(x, y) \in \{0, 1, 2, \ ... \ , \ n\}$.

4.3 Iterative Background Refinement and Object Detection

With the first detection step complete and the high intensity detections flagged, the background determination step can be applied once again with a new condition. Values that have been flagged as detections are not incorporated in the determination of the background level. This causes a lower background level to be found because the high intensity detected pixels are not included in the background calculation. The object detection step is then conducted again with the new values $b(i)$ and $\sigma(i)$. This process is conducted iteratively until no new pixels are added to the SIO, which coincides with convergence to the approximate true background.

4.4 Object Recognition

After the background and object pixels have been distinguished from one another, the program needs a way to determine which collections of pixels belong to a single object. Remember that a continuous, closed cell of pixels is considered a singular

object. To begin this process, the SIO subframes are reconstructed into original image coordinates: *SIO(x,y,i)* → *SIO(x,y)*. Once this SIO is reconstructed the image can be scanned row-wise for detected pixels. Once a detected pixel is found the *border and fill algorithm* is applied [16]. The border and fill algorithm is made up of two steps, aptly named *border* and *fill*.

The border step creates a shell of pixels valued -1 around a neighborhood of adjacent detected pixels. To do this an algorithm is defined to take a walk around the detected neighborhood. Cardinal directions (north, south, east, and west) are used to indicate absolute direction, while up, down, left, and right are used to indicate direction based on orientation determined from the current and previous pixel. Starting directly north of the initially discovered pixel, the walk begins by investigating the pixels directly adjacent to the pixel we are located on. Starting to the left of where we are facing pixels are checked in clockwise order: left, forward, then right, and finally, backwards. The first pixel found that is not a detection pixel is the one the search is moved to. Note that to accomplish this, a direction must be defined, meaning the next pixel the search is moved to is a function of the current pixel, and the previous pixel. The pixel that is moved to is assigned a value of -1. The algorithm continues until the walk returns to the initial position (directly north of the first detected pixel). What this means is that all pixels around a cluster of adjacent detected pixels is defined as the objects border, creating a closed cell of detected pixels.

Once the border around the detected object is created, the program can execute the fill step, starting with the originally discovered detection pixel. This step implements the well documented *flood fill algorithm*. This is a recursive algorithm that reads the value of the selected pixel and determines if it is not the desired value, or the border value. If both conditions are met it changes it to the desired value and applies it to all adjacent and diagonal pixels. Once the algorithm has come up on border pixels it unwinds back to the starting value and concludes the fill process. To accomplish this task efficiently the procedure is applied to the *clipped object*. This decreases the

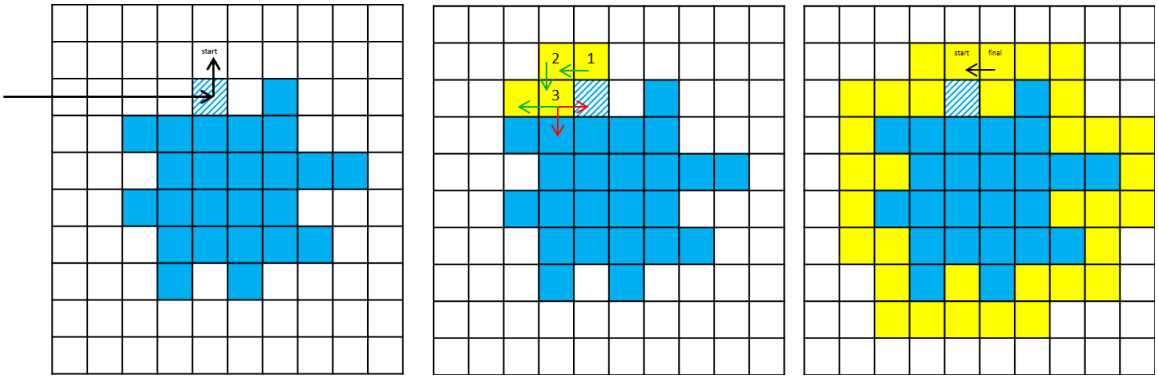

Figure 4.2.. Once a detection pixel is found (hatched pixel) the border algorithm starts. The starting position is directly above the first pixel (provided it is not a detection pixel itself). Next the algorithm will search adjacent pixels starting left, then front, then right, then it will go backwards. This is conducted until the starting pixel is discovered.

memory requirement by passing a smaller image in the recursive procedure. Define the clipped object as:

$$\begin{aligned} x_{clip} &= [min(x_{bdr}),\ max(x_{bdr})] \\ y_{clip} &= [min(y_{bdr}),\ max(x_{bdr})] \end{aligned} \tag{4.2}$$

Where x_{clip} and y_{clip} define a rectangle of all pixels between the minimum and maximum value of each coordinate contained in the border of the object. Once the flood fill algorithm has been completed, the clipped image is reinserted back into its corresponding location in the whole image.

Once completed, the algorithm inserts a well-defined object of known pixel size back into the SIO. At this point, an arbitrary minimum object pixel area can be selected as a basis by which false detections can be rejected. If the object is below the minimum pixel area, the object is rejected and the border and detection pixels are set to zero in the SIO. If the object is of an acceptable size, it is assigned a number, counting up from 1 to the number of accepted objects. The border is assigned the negative value of this number, while the object area is assigned the positive value. The search is then continued until the end of the image is reached. Pixels that have

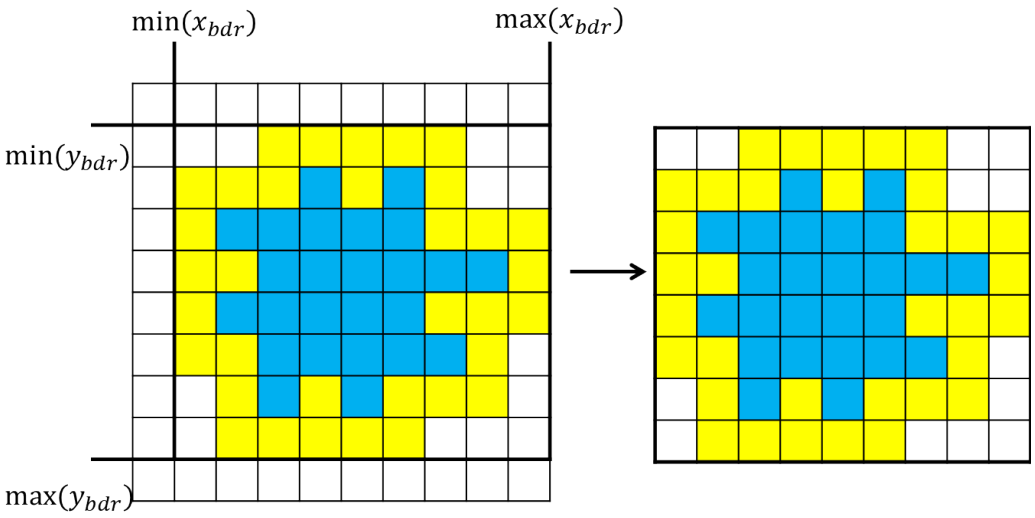

Figure 4.3.. The pixels contained within the domain defined in Equations 4.2 are extracted and stored as the clipped image of object.

already been incorporated into an object are not searched again, as they have already been accounted for. The minimum pixel area is kept as a user input that can be modified if it expected that faint RSOs are being rejected. In most cases, given the hardware used for this work, the streaks and points occupy a sufficiently large area to incorporate this procedure and not reject desired objects.

4.5 Object Position in Frame

To determine the precise position of objects that span several pixels in the frame, the *center of light* is defined. This can be interpreted as the direct analog of the center of mass, or first moment of inertia of the object, except instead of infinitesimal mass elements the object is composed of discrete pixel intensity elements. This method determines the sub-pixel level, brightness weighted position of an object in the frame. The center of light for an object made up of N pixel elements is defined as:

$$x_c = \frac{1}{I}\sum_{i=1}^{N} p(x_i, y_i)x_i, \tag{4.3}$$

$$y_c = \frac{1}{I}\sum_{i=1}^{N} p(x_i, y_i)y_i, \tag{4.4}$$

$$I = \sum_{i=1}^{N} p(x_i, y_i). \tag{4.5}$$

Where I is the total object intensity and the coordinates of the center of light of an object are given by the ordered pair $COL(x, y) = (x_c,\ y_c),\ x = \{x_i \mid i \in \{1, 2,\ \ldots, N\}\},\ y = \{y_i \mid i \in \{1, 2,\ \ldots, N\}\}$. Note that a streaked object's center of light provides its location on frame at the middle of the exposure. For example, if a 2 minute exposure was taken at 12:00, then the center of light of a streaked object would indicate its position at 12:01. Additionally, the border is not included in the center of light calculation, as it is not a detection pixel and as a result, does not contribute to the object.

4.6 Object Categorization

It is not enough to simply know the location of the object, it is also required to be able to categorize the type of object under investigation. As stated in the previous chapter, there are two tracking modes used in the system: sidereal tracking and RSO tracking. In either case two types of objects are expected: points and streaks. In sidereal tracking mode stars appear as points and an RSO appears as a streak. In RSO tracking mode the stars appear as streaks and the tracked RSO appears as a point, depending on the quality of the TLE. Additionally, other satellites with different line of sight rates will appear as streaks, as they require different tracking rates. The tracking mode is a user input, the program can use this to differentiate stars and RSOs by determining which objects are streaks and which objects are points.

Assuming that an object has a clipped image spanning N rows and M columns then the center of light can be rewritten as the following:

$$x_c = \frac{1}{I}\sum_{i=1}^{N}\sum_{j=1}^{M} p(x_i, y_j) x_i \, S(x_i, y_j), \tag{4.6}$$

$$y_c = \frac{1}{I}\sum_{i=1}^{N}\sum_{j=1}^{M} p(x_i, y_j) y_j \, S(x_i, y_j), \tag{4.7}$$

where $S(x_i, y_j)$ is the symbolic image of object containing only the binary values for detection pixels. It's contribution makes it so that only pixels associated with the object are incorporated in the calculation. This is the first moment of intensity, or in statistical terms: the expectation of the object position weighted by intensity. The second moment of intensity is analogous to the moments of inertia, or the second statistical moment: variance. Much like the covariance matrix, the *Tensor of Light* (TOL) is defined as:

$$\boldsymbol{K}_{xx} = \frac{1}{L}\sum_{i=1}^{n}\sum_{j=1}^{m} p(x_i, y_j)(x_i - x_c)^2 \, S(x_i, y_j) \tag{4.8}$$

$$\boldsymbol{K}_{xy} = \frac{1}{L}\sum_{i=1}^{n}\sum_{j=1}^{m} p(x_i, y_j)(x_i - x_c)(y_j - y_c) \, S(x_i, y_j) \tag{4.9}$$

$$\boldsymbol{K}_{yx} = K_{xy} \tag{4.10}$$

$$\boldsymbol{K}_{yy} = \frac{1}{L}\sum_{i=1}^{n}\sum_{j=1}^{m} p(x_i, y_j)(y_j - y_c)^2 \, S(x_i, y_j) \tag{4.11}$$

$$\boldsymbol{K} = \begin{bmatrix} K_{xx} & K_{xy} \\ K_{yx} & K_{yy} \end{bmatrix}. \tag{4.12}$$

The tensor of light is sensitive to the shape of the object. An object that is perfectly symmetric about the center of light would be expected to have equal main diagonal elements and off diagonal elements equal to zero. If the distribution becomes stretched in any one principal direction, the diagonal element associated with that direction should become larger. If the streak is angled with respect to the x-y frame, then the

magnitude of the off diagonal elements should increase until the streak reaches a 45° angle, at which point the magnitude of all elements of $\boldsymbol{K}$ should be approximately equal. With all of this in mind, the following streak categorization criteria can be defined:

$$\textit{Stretched in } X: \qquad \boldsymbol{K}_{xx}/\boldsymbol{K}_{yy} > \Delta \tag{4.13}$$

$$\textit{Stretched in } Y: \qquad \boldsymbol{K}_{yy}/\boldsymbol{K}_{xx} > \Delta \tag{4.14}$$

$$\textit{Stretched Diagonal}: \qquad |\boldsymbol{K}_{xy}/\boldsymbol{K}_{xx}| + |\boldsymbol{K}_{xy}/\boldsymbol{K}_{yy}| > \delta, \tag{4.15}$$

where Δ and δ are two constants that must be tuned based on the expected length of streaks and system intensity range (taken from the hardware). The first two conditions apply for near horizontal and near vertical streaks respectively. The third condition covers any streaks that are not aligned with the x or y axis. When the streak makes a small angle with respect to a given axis, the associated ratio of off diagonal to main diagonal element will be very low, while the ratio with the other axis will be high. For this reason the two are summed. If the light is uniformly distributed along the *length* of the streak then the third condition should reach a minimum value of 2 at 45 degrees. This is a reasonable assumption because the airy disk is integrated over the length of the streak at a constant tracking rate. All should receive roughly uniform intensity excluding the end caps which are symmetric. This allows for a theoretical value of $\delta = 2$.

Below, two simulated object of uniform intensity are used to provide intuition regarding the behavior of the TOL. The first is a streak and the second is a point. Both objects have uniform intensity value of 1. Both are shown at an angle of 0° in Figure 4.4. Each object is rotated 180° in intervals of 0.1° and the resultant TOL is calculated.

The resulting ratios of main-diagonal elements and off-diagonal elements of $\boldsymbol{K}$ are shown in Figures 4.5 and 4.6. As expected for the streaked object, for angles near $\frac{n\pi}{2}$ the ratio of main-diagonal elements blows up and the ratio of off-diagonal elements to main-diagonal elements drops to zero. For angles in between the sum of the ratio of

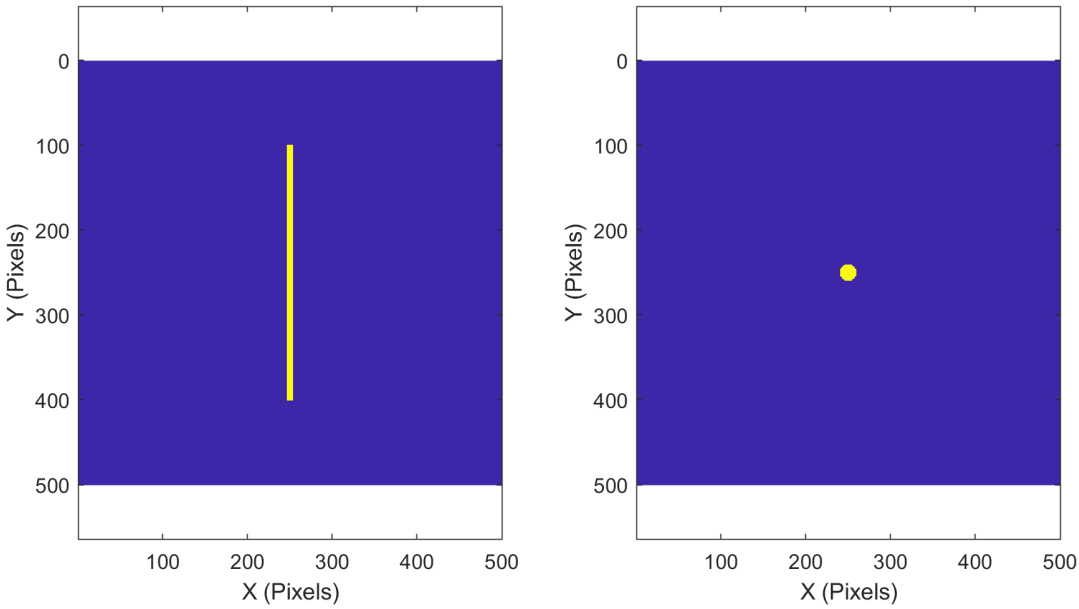

Figure 4.4.. Two simulated objects: streak (left) and point (right). Each figure is shown with an angle of 0° in the figure. The TOL is rotated through 180 degrees to examine the resultant TOL.

the off-diagonal element and the two main-diagonal elements produces a value whose minimum is two. For the point object the ratio of main-diagonal elements is always approximately one, while the sum of off-diagonal to main-diagonal ratios is near zero. Note that the discontinuities in the plots exist because as the point is rotated in the discrete pixel grid it becomes marginally unsymmetrical, in the order of 1 to 2 pixels.

To calibrate Δ and δ, objects taken from observations at the POGS have been clipped and the TOLs computed. The resulting ratios can vary based on the tracking mode, tracking rate, and exposure time. It has been found for satellite tracked mode with a range of exposure time of 6-8 seconds the values $\Delta = 75$ and $\delta = 2$ are able to successfully discriminate between streaks and points. These values are used as default for the purposes of the processing pipeline, but in the event that a different set of observation parameters were required, these values could be calibrated given a few observations.

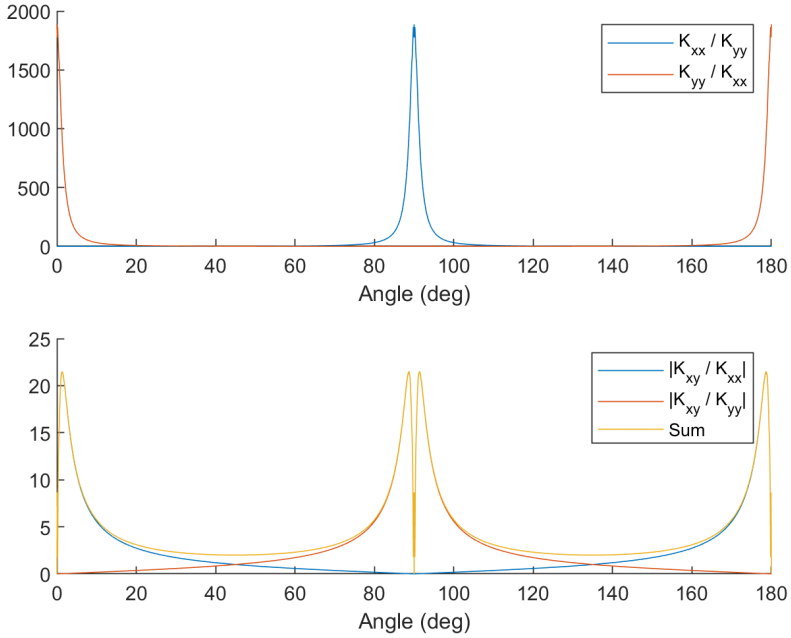

Figure 4.5.. Ratios of elements of $\boldsymbol{K}$ for the streak object. The top figure shows the ratio of main-diagonal elements while the bottom shows the ratio of off-diagonal elements to main-diagonal elements.

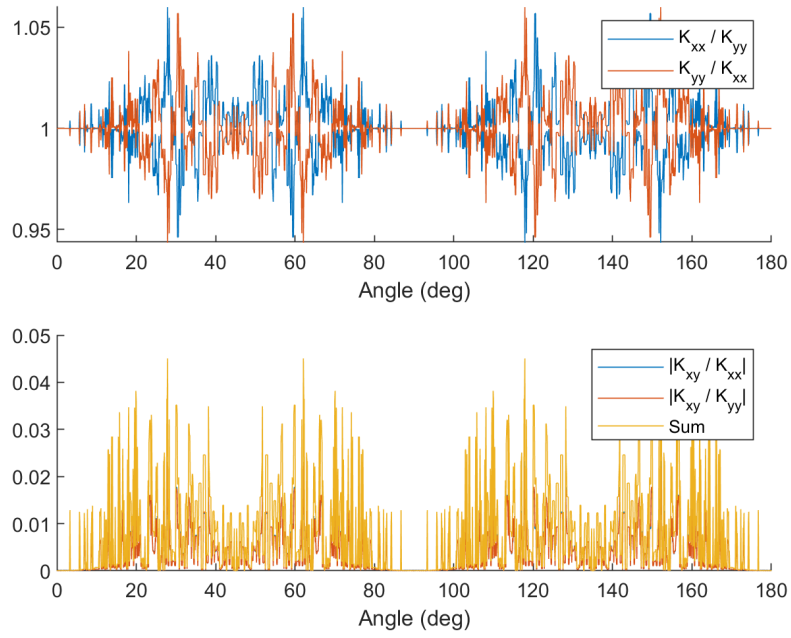

Figure 4.6.. Ratios of elements of $\boldsymbol{K}$ for the point object. The discrete nature of the pixels causes the object to become unsymmetrical by one or two pixels throughout the rotation.

4.7 Reconstructing Disintegrated Streaks

The procedure outlined thus far provides the program the capability to autonomously group clusters of pixels, locate them in the frame, and decide if they are potential RSOs or stars. In the default tracking mode stars appear as long streaks. It is possible that stars have a sufficiently low signal to noise ratio that the threshold technique cannot pick up the object from the background level. In some cases the technique can pick up parts of the streak but not a continuous cluster of pixel, which results in a series of small objects on top of the streak. This is defined as a *disintegrated streak*: one that should belong to a single object but has been broken into several smaller ones. This is undesirable for two reasons, the first being that a potential star to conduct astrometry with is lost. The second is that several anomalous objects are fed down the pipeline. Figure 4.9 shows an example of a disintegrated streak in an observation made at the POGS. The red $\times$'s are the solved COL's. The object on the left of the frame shows a well defined streak, while the cluster of objects on the right make up a disintegrated steak.

Knowing that these can be present in any image, the goal is to reconstruct the disintegrated streak to be associated as one continuous group of pixel using information from the post processed image. To proceed, it is assumed that *at least* one good detection has been made on frame. If this is not the case it is recommended that the threshold parameters be reevaluated. If at least one good detection is made, then a streak model can be produced.

4.7.1 Streak Model

Figure 4.7 shows the expected distribution of a streak created by a point source. The point source is a bi-variate Gaussian distribution of intensity, which is then translated at a constant rate in the image plane. Along the direction of the translation, the intensity should be uniform, excluding the ends, which will still be Gaussian. These can be neglected as they take up a small portion of the length-wise component.

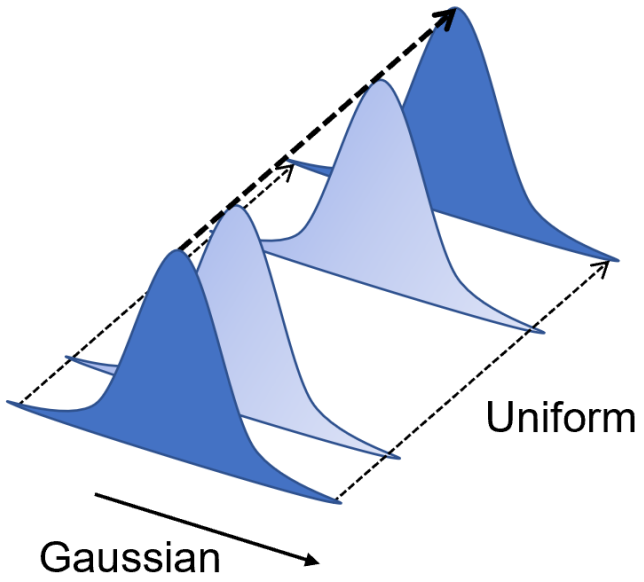

Figure 4.7.. Expected distribution of intensity for a streak. Note that as the point source is translated on the frame, a uniform distribution is expected along the length of the streak, excluding the ends.

Knowing the expected distribution of intensity, the eigenvalues and eigenvectors of the TOL should provide insight to the size and orientation of the streak. Knowing that the width of the streak is Gaussian, the width-wise eigenvalue of the TOL can be used to approximate the width of the streaks, as it is the variance of the intensity. The length-wise eigenvalue does not give a good approximation of the streaks length because the intensity is not normally distributed along the length of the streak. Despite this, information from the fits-header can be used to provide a streak length for the model:

$$L = \sqrt{\dot{\alpha}^2 + \dot{\delta}^2}\left(\frac{T}{\tau}\right), \tag{4.16}$$

where $\dot{\alpha}$ and $\dot{\delta}$ are the right ascension and declination tracking rate, T is the exposure time, and τ is the pixel scale. With values computed for the length and width of the streak, and the eigenvectors providing orientation, a model can be created to fit

potentially disintegrated streaks to. The length-wise eigenvector is called $\hat{l}$, and the total length of the streak in this direction is given as L in Equation 4.16. The width-wise orientation is given by $\hat{\lambda}$ and the half-width magnitude is given by $\lambda = 3\sigma$. This is shown on the left in Figure 4.8.

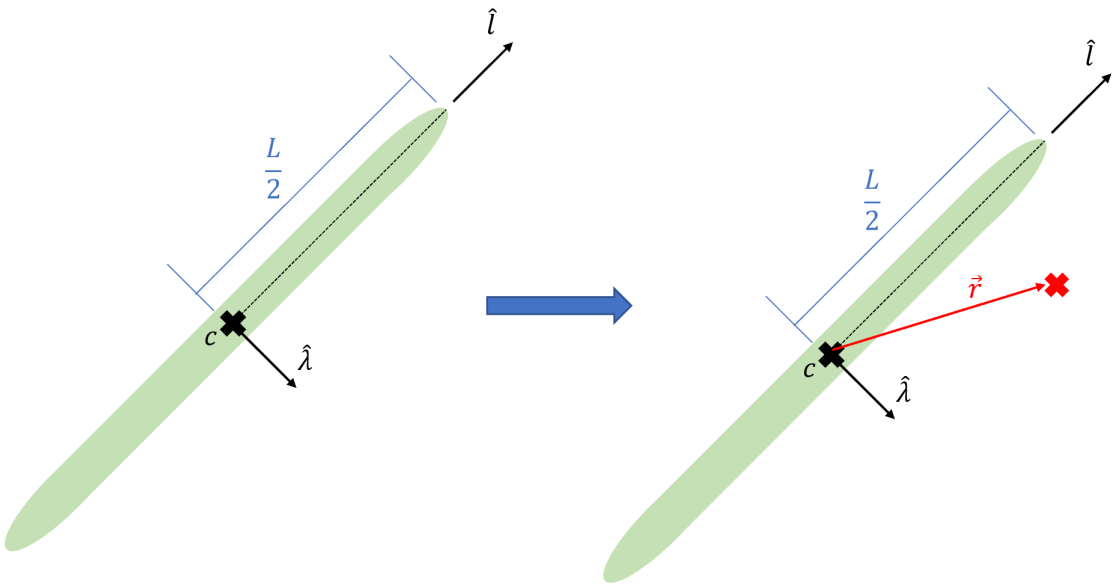

Figure 4.8.. A given well-defined streak is shown in green. On the left, the unit vectors $\hat{l}$ and $\hat{\lambda}$ are shown, centered on the COL, c. On the right, another COL is shown as a red $\times$ at an arbitrary distance $\vec{r}$ from c.

The TOL is taken from the brightest streak found in the post-processed image and used to compute the model parameters. With a model defined, it can be used to determine if a streak is disintegrated. To do this the model is fixed at a specified COL. The distance between it and another COL can then be computed. The projections of this distance can then be evaluated against the known length and width of the streak model. If the projections are less than both of these quantities, then the COL is contained within the model.

$$\vec{r}_l = \vec{r} \cdot \hat{l} < L/2 \qquad \vec{r}_\lambda = \vec{r} \cdot \hat{\lambda} < \lambda \tag{4.17}$$

This procedure is conducted with each COL as the center. For each COL, $\vec{r}$ is computed for every other COL, and conditions in Equation 4.17 are evaluated. If these criteria are met, the COL fits within the streak model and the two COLs are to be reunified.

4.7.2 Reunifying Streaks

When the criteria given in Equation 4.17 are met, then the objects must be combined into a single object, which will generate a new COL and TOL. To do this, the SIO needs to be updated to "bridge the gap" between the two objects. A simple way to do this that has proven successful is to fill in the interpolated pixels along the vector $\vec{r}$ as detections. What this means is that the border algorithm from the object recognition step will see this as one continuous cell of pixels, group it as one object, and determine the COL for the whole thing. The object recognition step is conducted for a second time after all COLs have been used as the center for the model. Figure 4.10 below shows the result of the procedure on the disintegrated streak shown in Figure 4.9.

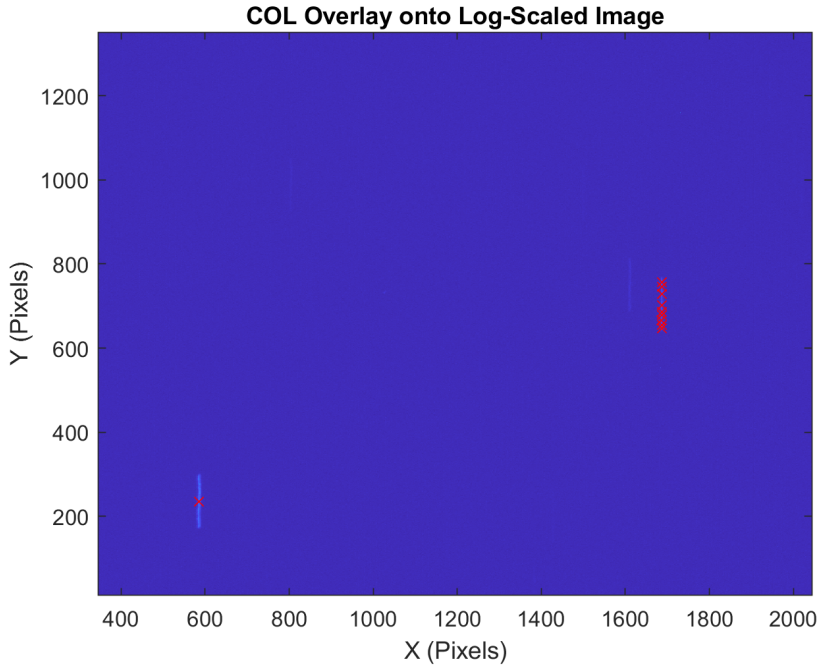

Figure 4.9.. Clipped observation taken from the POGS showing a well-defined streak (left) and a disintegrated steak (right). The red ×'s on the frame are the computed COL of the object. The disintegrated streak is made up of several objects, which is undesirable.

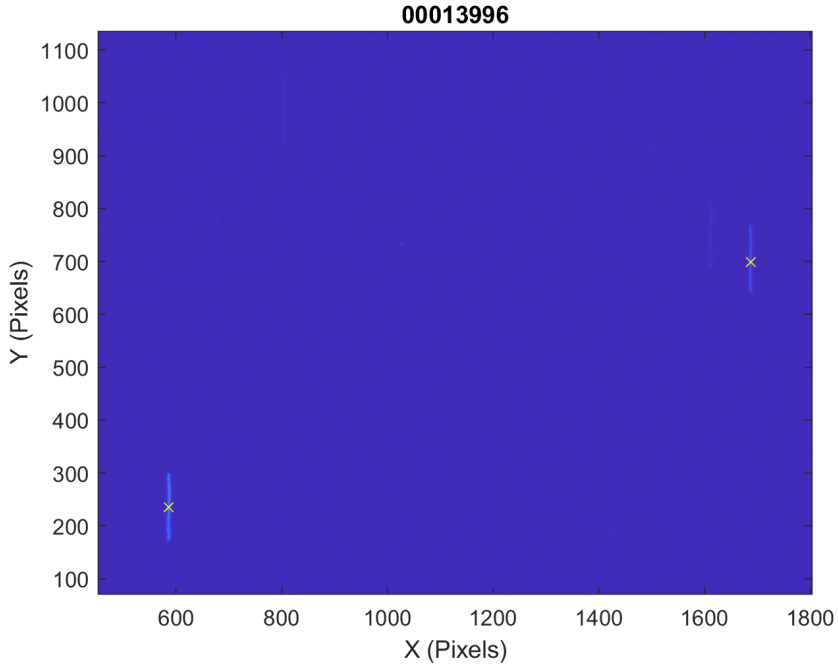

Figure 4.10.. Clipped observation after the streak reconstruction procedure is applied.

5. ASTROMETRY AND PLATE SOLVING

The output of a successful image processing procedure provides the user with categorized objects and their centroids in pixel coordinates. The astrometry step bridges the gap between the object pixel coordinates and the astronomical topocentric coordinates used to position RSOs. To do this, an accurate transformation between pixel grid coordinates (x, y) and astronomical coordinates (α, δ) must be obtained.

The calibrated telescope home position provides a crude approximation relating pixel coordinates to astronomical topocentric coordinates. The true pointing direction is hardware dependent and prone to offsets from desired pointing direction, which are expected to grow as angular distance from the home position increases. Mount models are employed to offset systematic long term, stable errors. Despite this, short periodic errors as well as vibrations due to wind even after the telescope settle time at a specific direction lead to significant errors of the order of several tenths of an arcsecond or more. Perhaps most importantly, atmospheric refraction is varies significantly with time and offsets the imaged field from the expected theoretical field, even when an accurate pointing direction is provided. For all of these reasons, a plate solving procedure is developed, which employs the use of star catalogs to provide transformation from pixel coordinates to astronomical coordinates that is orders of magnitude more accurate than using raw instrument readout.

An in-depth description of the astrometric procedure that has been implemented is provided. This includes the selection of a star catalog, the definition of a usable transformation from pixel coordinates to astronomical coordinates, a procedure used for star identification, and the determination of the optimal fit for a pixel to astronomical transformation. In addition to software developed for this work, an existing tool for plate solving and the options that it makes available is examined and applied.

5.1 Star Catalogs

There exist several star catalogs of variable accuracy and completeness, each of which provide a variety of information. In 1989 the European Space Agency launched the Hipparcos satellite star mapper, which collected astronometric data for over three years [36]. Since termination of satellite observations, the data has been used to produce several star catalogs, including Hipparcos (1 and 2) and Tycho (1 and 2). The Tycho-2 catalog was released in 2000, and contains the position and proper motions of more than 2.5 million stars [37]. The catalog is accurate to roughly 7 mas and is well covered for stars with magnitudes less than 11.5. It contains the position and proper motion of stars in ICRS at epoch J2000.0. This catalog has been selected for use due to its completeness and accuracy of bright star positions. The catalog has a mean stellar density ranging from 150 stars per square degree ($b = 0$) to 25 stars per square degree ($b = 90$), where b is the galactic latitude. An expected minimum of 25 stars per square degree is adequate to attempt the plate solving procedure to be outlined below. Since the Hipparcos mission, the Gaia mission has begun and has generated two data releases with significant improvements in the accuracy and completeness for faint stars. This catalog is not currently being used as it contains far more entries than are needed to conduct the plate solving procedure. Note that any star catalog that provides position, proper motion, and magnitude can be used with little to no modification to the program.

As the star catalog contains more than 2.5 million entries, it helps to narrow down candidates that may be in view. The pointing direction is read out from the telescope mount and transformed to topocentric astronomical coordinates using Equation 2.45. The theoretical field of view determined by the telescope optical assembly can then be used to select candidate stars in a given window.

$$S' = \left\{ S_i \;\middle|\; \cos^{-1}\left(\cos(\alpha_i - \alpha_0)\cos(\delta_i - \delta_0) \right) < \left(\frac{1}{2} FOV + \varepsilon \right) \right\} \; \forall \; i \in \{1, 2, \; \ldots, N_{cat}\}$$

where S' is a subset of the star catalog S that meets the provided condition: the angular distance from the expected field center (α_0, δ_0) to the catalog star coordinates is less than half the field of view, plus a buffer (ε). This buffer accounts for the uncertainty in pointing direction due to model inaccuracy and measurement noise, atmospheric effect, and field rotation. N_{cat} is the number of entries in the star catalog.

Once the catalog has been filtered, the catalog stars must be propagated to their apparent positions on the date of the observation. The catalog contains each star's observed proper motion in right ascension and declination ($\mu_{\alpha*}$, μ_δ), which can be used to propagate the stars. A simplified treatment for how to do this is given in the official documentation for the Hipparcos and Tycho catalog release [38]. It is noted in the documentation that this model only varies slightly from the more rigorous model for the majority of cases, especially over the time scales of this study. The model is given by the following:

$$\alpha(T) = \alpha(T_0) + (T - T_0)\mu_{\alpha_0^*} \sec\left(\delta(T_0)\right) \tag{5.1}$$

$$\delta(T) = \delta(T_0) + (T - T_0)\mu_{\delta_0} \tag{5.2}$$

where T is the time of observation and T_0 is the catalog epoch. Note that $\mu_{\alpha*}$ and μ_δ are each given in units of milli-arcseconds / year, or arcseconds / century. If stars in frame have large values for proper motion, a larger ε can be used before the propagation, followed by a second filtering based on expected FOV to account for a star moving into or out of the window.

5.2 Transformation from Focal Plane to Astronomical Coordinates

As discussed in Chapter 3, the focal plane can be imagined as a tangent plane to the celestial sphere, with tangent point located at the field center. The domain of the plane is defined by the field of view, which is dependent on observation instrumentation as well as atmospheric disturbance. In this domain, the tangent plane only touches the celestial sphere at one location: the field center. For this reason,

the celestial sphere must be projected onto the focal plane. Figure 5.1 shows two common projections: Gnomonic and Orthographic. The two projections are given by the following:

$$Gnomonic: \qquad d(\theta) = \tan(\theta) \tag{5.3}$$

$$Orthographic: \qquad d(\theta) = \sin(\theta) \tag{5.4}$$

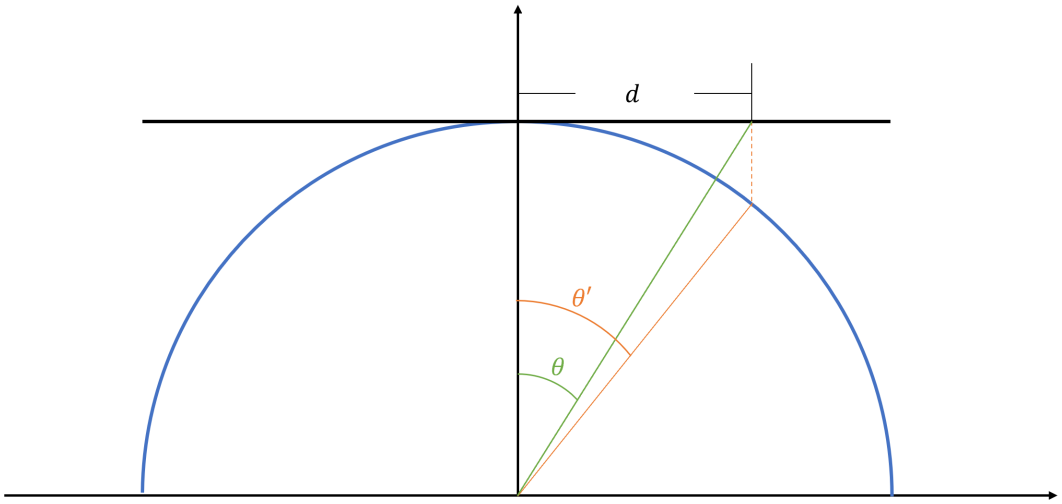

Figure 5.1.. Cross section of the tangent focal plane to the celestial sphere. The two angles depicted show the Gnomonic projection in green and the orthographic projection in orange.

Both of these projections provide a nonlinear map from a specified angular value on the celestial sphere to the focal plane. It is also well known that at small angles these functions behave approximately linearly. Figure 5.2 shows the two functions for values of $0 \leqslant \theta \leqslant \pi/4$ radians.

The plot shows that in the region near the origin, the functions do behave linearly. The error for the linear transformation can be taken as the difference between θ

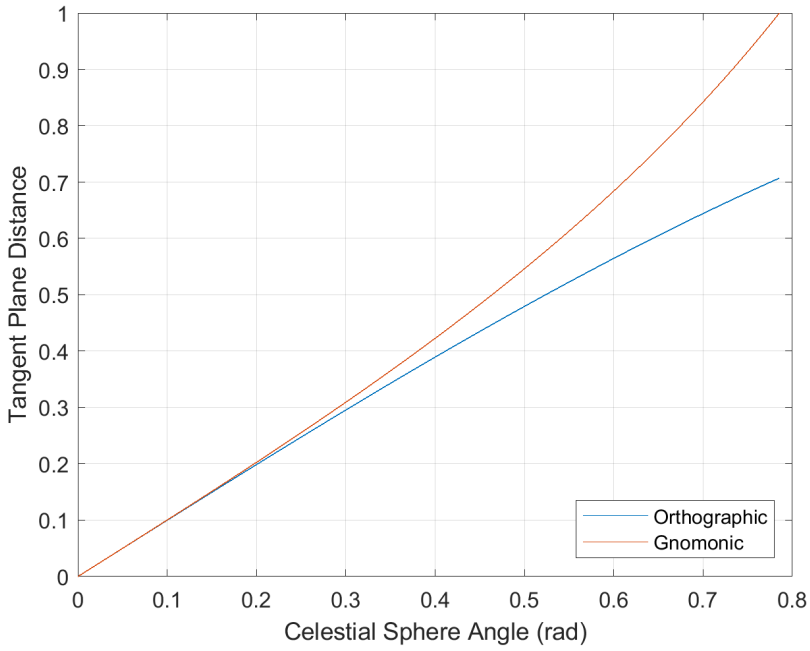

Figure 5.2.. Resultant distance on the tangent plane from the origin produced using the two discussed projections. Both behave linearly in the vicinity of the origin.

and $d(\theta)$. To put this in terms of field of view, the maximum expected error for approximating the transformation as linear is given by the following:

$$\Delta_1 = \frac{\sqrt{2}}{2}FOV - \sin\left(\frac{\sqrt{2}}{2}FOV\right)$$
$$\Delta_2 = \frac{\sqrt{2}}{2}FOV - \tan\left(\frac{\sqrt{2}}{2}FOV\right).$$

For the theoretical field of view computed in Chapter 3 ($FOV = 49.4129$ arcmin) the maximum expected error is computed as:

$$\Delta_1 \approx 0.0361 \; arcseconds$$
$$\Delta_2 \approx 0.0722 \; arcseconds.$$

The pixel scale computed from the theoretical field of view and the 4096×4096 pixel grid for the CCD being used is approximately $\tau \approx 0.7238$ arcsec/pixel. The larger

error computed from Δ_2 equates to an error of 0.0997 pixels. This is far lower than the error expected from the centroiding procedure conducted in the image processing step. For this reason, the field of view is considered sufficiently small to apply a linear transformation from asronomical coordinates to pixel coordinates (and vice versa).

With a linear map justified, the transformation from pixel coordinates to astronomical topocentric coordinates can be produced. The tangent frame is, in most cases, not aligned with the astronomical topocentric frame. For this reason, a rotation by some angle (θ) is applied in in the transformation. Additionally, the raw image places the origin in the corner of the frame, so it is shifted to the field center before the rotation and scaling is applied. All of this produces the following:

$$\vec{s} = \tau \begin{bmatrix} \cos(\theta) & -\sin(\theta) \\ \sin(\theta) & \cos(\theta) \end{bmatrix} \left(\vec{p} - \vec{p_0} \right) + \vec{s_0} \tag{5.5}$$

$$\vec{s} = \begin{bmatrix} \alpha & \delta \end{bmatrix}^T \qquad \vec{s_0} = \begin{bmatrix} \alpha_0 & \delta_0 \end{bmatrix}^T \tag{5.6}$$

$$\vec{p} = \begin{bmatrix} x & y \end{bmatrix}^T \qquad \vec{p_0} = \begin{bmatrix} 2048 & 2048 \end{bmatrix}^T \tag{5.7}$$

where τ is the pixel scale, θ is the angle by which the field is rotated, $\vec{p_0}$ is the pixel coordinate vector of the field center, and $\vec{s_0}$ is the astronomical coordinate vector of the field center. For any pixel coordinate $\vec{p}$ a distinct transformation to topocentric right ascension and declination can be produced, provided the field rotation (θ) and astronomical topocentric coordinates for the field center ($\vec{s_0}$) can be determined.

5.3 Star Identification and Pattern Matching

The observed stars must be matched with those in the local star catalog; constructed using the pointing direction with stars from the catalog that meet the condition given in Equation 5.1. If the observed stars can be positively matched to stars contained in the local star catalog, the precise positions from said catalog can be

used to determine the field rotation and astronomical coordinates of the field center such that the difference between the transformed positions and catalog positions is minimal. If the field rotation is stable, prior solutions for the angle can be used to employ a localized matching technique for star identification. In order to avoid this constraint, an algorithmic framework used for star trackers and the lost in space problem is employed [39, 40]. This method has been selected to remain independent of prior estimates and to ensure robustness in the presence of larger deviations from expected field center locations.

To match the observed stars with those in the local catalog, a pattern set must be constructed. This pattern set provides a quantitative way to compare the orientation of groups of stars. As covered in the previous section, the small field of view used in this study allows for a linear map from the celestial sphere to the pixel grid. For the same reason, the planar triangle pattern set using area and polar moment proposed by Cole and Crassidis is used [39]. This pattern set has been shown to be usable in small field of view applications, as the deviation from the spherical geometry is negligible. To start, three stars are selected (s_1, s_2, s_3). The stars astronomical position is given as: $\vec{s_i} = [\alpha_i, \delta_i]^T$. Using this, the angular distance that make up the three sides of the triangle are given as:

$$a = ||\vec{s}_1 - \vec{s}_2|| \tag{5.8}$$

$$b = ||\vec{s}_2 - \vec{s}_3|| \tag{5.9}$$

$$c = ||\vec{s}_1 - \vec{s}_3||. \tag{5.10}$$

Heron's formula can then be used to compute the angular area of the planar triangle using only its side lengths:

$$s = 1/2(a + b + c) \tag{5.11}$$

$$A = \sqrt{s(s-a)(s-b)(s-c)}. \tag{5.12}$$

Next, the polar moment of area can be found as a function of the triangles area:

$$J = \frac{A}{36}(a^2 + b^2 + c^2). \tag{5.13}$$

These two patterns form the pattern set by which the observed star triangles and the local catalog triangles can be compared. The pattern set is computed for every permutation of three stars from the local catalog. This creates the local catalog pattern set defined by:

$$P_{i,j,k}(\vec{s}_i, \vec{s}_j, \vec{s}_k) = \begin{bmatrix} A_{i,j,k} & J_{i,j,k} \end{bmatrix}, \qquad \forall \left[i,j,k \in \{ l \in \mathbb{Z} |\ 0 < l \leqslant N_{ref} \} \right]_{i \neq j \neq k}. \quad (5.14)$$

The star positions given in the local catalog are assumed to have zero error and are used as truth values. As a result the pattern set generation is completely deterministic. The observed star positions on the other hand are known to have some error. This same procedure can be used to produce the observed triangle pattern set, but some additional statistical information must be provided to define a window over which the pattern set can reasonably be expected to exist. This starts with the following observed star position:

$$\vec{p}_i = \begin{bmatrix} x_i \\ y_i \end{bmatrix} + \vec{\nu}_i, \quad (5.15)$$

where $\vec{\nu}_i$ is zero-mean Gaussian noise ($E\{\vec{\nu}_i\} = \vec{0}$, $E\{\vec{\nu}_i \vec{\nu}_i^T\} = \boldsymbol{R}_p$). To produce the pattern set the measured star positions must be represented in angular positions. Although the absolute positions of the measured stars have yet to be determined, the pattern set is only dependent on *relative* star positions. Meaning, regardless of the field rotation (θ) and astronomical topocentric coordinates of the field center ($\vec{s}_0$), the observed triangles will have the same area and polar moment. Because of this, the pattern set can be generated by setting both of these parameters to zero. With this, the reduced transformation for pattern generation is given by:

$$\begin{aligned} \widetilde{s}_i &= \tau(\vec{p}_i - \vec{p}_0) \\ &= \tau\left(\begin{bmatrix} x_i \\ y_i \end{bmatrix} - \begin{bmatrix} 2048 \\ 2048 \end{bmatrix} + \vec{\nu}_i \right) \\ &= \tau\left(\begin{bmatrix} x_i \\ y_i \end{bmatrix} - \begin{bmatrix} 2048 \\ 2048 \end{bmatrix} \right) + \vec{\xi}_i, \end{aligned} \quad (5.16)$$

where $\vec{\xi}_i = \tau\vec{\nu}_i$. This is also zero-mean Gaussian noise ($E\{\vec{\xi}_i\} = \vec{0}$, $E\{\vec{\xi}_i\vec{\xi}_i^T\} = \boldsymbol{R}$). The measurement covariance is denoted as $\boldsymbol{R}$ here as it is often more natural to discuss measurement error in angular values than in pixel units. With this, the pattern set can be computed using each of the transformed star positions $\widetilde{s}_i$ for all observed triangles.

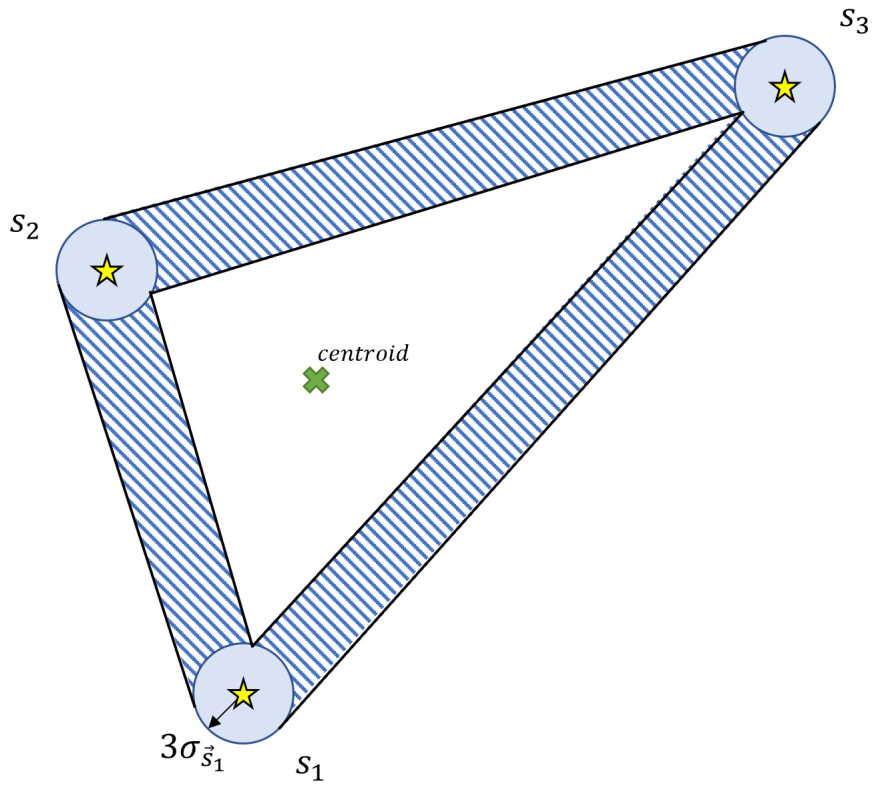

Figure 5.3.. Three measured stars, each with associated position error. The error in position is used to define a window of possible triangle areas, given by the hatched region.

Next, the variance of each pattern can be computed. The area and polar moment are each a nonlinear function of $\widetilde{s}_i$, which has measurement covariance that is assumed to be known ($\boldsymbol{R}$). Figure 5.3 shows the position of three stars as a random variable. The blue circles define 3σ bounds, which are a region that the observer is 99.7% certain the stars are contained in. The hatched area is the resultant region that

contains all possible triangles. If a candidate triangle from the local triangle set were to fit within this region it would be flagged as a potential match. The way this is determined is if the difference between the candidate triangle's pattern set and the observed triangle's pattern set fits within the computed 3σ bounds of the observed triangle's pattern set.

Knowing that the functions are nonlinear, a linearization procedure to determine the variance is conducted. This procedure is very similar to that conducted in [39]. The area linearization is given by:

$$\boldsymbol{H}_A = \begin{bmatrix} \frac{\partial A}{\partial \widetilde{s}_1} & \frac{\partial A}{\partial \widetilde{s}_2} & \frac{\partial A}{\partial \widetilde{s}_3} \end{bmatrix} \tag{5.17}$$

$$\frac{\partial A}{\partial \widetilde{s}_1} = \frac{\partial A}{\partial a}\frac{\partial a}{\partial \widetilde{s}_1} + \frac{\partial A}{\partial c}\frac{\partial c}{\partial \widetilde{s}_1}, \qquad \frac{\partial A}{\partial \widetilde{s}_2} = \frac{\partial A}{\partial a}\frac{\partial a}{\partial \widetilde{s}_2} + \frac{\partial A}{\partial b}\frac{\partial b}{\partial \widetilde{s}_2}, \qquad \frac{\partial A}{\partial \widetilde{s}_3} = \frac{\partial A}{\partial b}\frac{\partial b}{\partial \widetilde{s}_3} + \frac{\partial A}{\partial c}\frac{\partial c}{\partial \widetilde{s}_3}.$$

Expanding the area function results in:

$$\begin{aligned} A &= \sqrt{s(s-a)(s-b)(s-c)} \\ &= \sqrt{\frac{1}{2}\left(a+b+c\right)\left(\frac{1}{2}(a+b+c)-a\right)\left(\frac{1}{2}(a+b+c)-b\right)\left(\frac{1}{2}(a+b+c)-c\right)} \\ &= \frac{1}{4}\sqrt{(a+b+c)(-a+b+c)(a-b+c)(a+b-c)}. \end{aligned}$$

This allows for the computation of the partial derivatives with respect to a, b, c:

$$\begin{aligned} \frac{\partial A}{\partial a} &= \frac{1}{2A}\left(\frac{1}{16}\right)\frac{\partial}{\partial a}\Big[(a+b+c)(-a+b+c)(a-b+c)(a+b-c)\Big] \\ \frac{\partial A}{\partial b} &= \frac{1}{2A}\left(\frac{1}{16}\right)\frac{\partial}{\partial b}\Big[(a+b+c)(-a+b+c)(a-b+c)(a+b-c)\Big] \\ \frac{\partial A}{\partial c} &= \frac{1}{2A}\left(\frac{1}{16}\right)\frac{\partial}{\partial c}\Big[(a+b+c)(-a+b+c)(a-b+c)(a+b-c)\Big] \end{aligned}$$

$$\frac{\partial A}{\partial a} = \frac{a(-a^2+b^2+c^2)}{8A} \tag{5.18}$$

$$\frac{\partial A}{\partial b} = \frac{b(a^2-b^2+c^2)}{8A} \tag{5.19}$$

$$\frac{\partial A}{\partial c} = \frac{c(a^2+b^2-c^2)}{8A} \tag{5.20}$$

Now, all that is needed is the partial derivatives of a, b, and c with respect to $\widetilde{s}_i$. Rewrite Equations 5.8, 5.9, and 5.10:

$$a = \sqrt{(\widetilde{s}_1 - \widetilde{s}_2) \cdot (\widetilde{s}_1 - \widetilde{s}_2)} \tag{5.21}$$

$$b = \sqrt{(\widetilde{s}_2 - \widetilde{s}_3) \cdot (\widetilde{s}_2 - \widetilde{s}_3)} \tag{5.22}$$

$$c = \sqrt{(\widetilde{s}_1 - \widetilde{s}_3) \cdot (\widetilde{s}_1 - \widetilde{s}_3)}. \tag{5.23}$$

This results in the following partial derivatives:

$$\frac{\partial a}{\partial \widetilde{s}_1} = \frac{\widetilde{s}_1 - \widetilde{s}_2}{a} \qquad \frac{\partial a}{\partial \widetilde{s}_2} = -\frac{\widetilde{s}_1 - \widetilde{s}_2}{a} \tag{5.24}$$

$$\frac{\partial b}{\partial \widetilde{s}_2} = \frac{\widetilde{s}_2 - \widetilde{s}_3}{b} \qquad \frac{\partial b}{\partial \widetilde{s}_3} = -\frac{\widetilde{s}_2 - \widetilde{s}_3}{b} \tag{5.25}$$

$$\frac{\partial c}{\partial \widetilde{s}_1} = \frac{\widetilde{s}_1 - \widetilde{s}_3}{c} \qquad \frac{\partial c}{\partial \widetilde{s}_3} = -\frac{\widetilde{s}_1 - \widetilde{s}_3}{c}. \tag{5.26}$$

Now, $\boldsymbol{H}_A$ can be computed using the provided partials. The result is a 6 length row vector. This results in the following equation for the linearization for the variance of area:

$$\sigma_A^2 = \boldsymbol{H}_A \boldsymbol{R} \boldsymbol{H}_A^T. \tag{5.27}$$

The same procedure can be applied to polar moment. Recall that polar moment is a function of a, b, and c, as well as A. This results in the following:

$$\boldsymbol{H}_J = \begin{bmatrix} \frac{\partial J}{\partial \widetilde{s}_1} & \frac{\partial J}{\partial \widetilde{s}_2} & \frac{\partial J}{\partial \widetilde{s}_3} \end{bmatrix} \tag{5.28}$$

$$\frac{\partial J}{\partial \widetilde{s}_1} = \frac{\partial J}{\partial a}\frac{\partial a}{\partial \widetilde{s}_1} + \frac{\partial J}{\partial c}\frac{\partial c}{\partial \widetilde{s}_1} + \frac{\partial J}{\partial A}\frac{\partial A}{\partial \widetilde{s}_1}, \qquad \frac{\partial J}{\partial \widetilde{s}_2} = \frac{\partial J}{\partial a}\frac{\partial a}{\partial \widetilde{s}_2} + \frac{\partial J}{\partial b}\frac{\partial b}{\partial \widetilde{s}_2} + \frac{\partial J}{\partial A}\frac{\partial A}{\partial \widetilde{s}_2},$$

$$\frac{\partial J}{\partial \widetilde{s}_3} = \frac{\partial J}{\partial b}\frac{\partial b}{\partial \widetilde{s}_3} + \frac{\partial J}{\partial c}\frac{\partial c}{\partial \widetilde{s}_3} + \frac{\partial J}{\partial A}\frac{\partial A}{\partial \widetilde{s}_3}.$$

Seeing as most of these have been computed to determine the variance of area, all that is needed is the partial derivatives of J with respect to a, b, c, and A. These can simply be computed using Equation 5.13.

$$\frac{\partial J}{\partial a} = \frac{aA}{18} \qquad \frac{\partial J}{\partial b} = \frac{bA}{18} \qquad \frac{\partial J}{\partial c} = \frac{cA}{18} \tag{5.29}$$

$$\frac{\partial J}{\partial A} = \frac{1}{36}(a^2 + b^2 + c^2) \tag{5.30}$$

These, along with the partials derived to determine the area variance can now be used to compute $\boldsymbol{H}_J$, which is also a row vector or length 6. This results in the variance of polar moment given as:

$$\sigma_J^2 = \boldsymbol{H}_J \boldsymbol{R} \boldsymbol{H}_J^T. \tag{5.31}$$

With the variance computed for the patterns of the observed triangles, the observed pattern set can be defined as:

$$\begin{aligned} \widetilde{P}_{i,j,k}(\widetilde{s}_i, \widetilde{s}_j, \widetilde{s}_k) = \Big[& A_{i,j,k} \quad J_{i,j,k} \quad \sigma^2_{A;i,j,k} \quad \sigma^2_{J;i,j,k} \Big], \\ & \forall \left[i,j,k \in \{ l \in \mathbb{Z} |\, 0 < l \leqslant N_{obs} \} \right]_{i \neq j \neq k}. \end{aligned} \tag{5.32}$$

With this, the criteria defining a match between a triangle in the local catalog pattern set and the observed triangle pattern set can be defined mathematically. Given the triangle formed by three observed stars $(\widetilde{s}_i, \widetilde{s}_j, \widetilde{s}_k)$ and a triangle formed by three stars in the local catalog $(\vec{s}_p, \vec{s}_q, \vec{s}_r)$, the following match criteria are defined:

$$\begin{aligned} |A_{i,j,k} - A_{p,q,r}| &< 3\sigma_{A;i,j,k} \\ |J_{i,j,k} - J_{p,q,r}| &< 3\sigma_{J;i,j,k}. \end{aligned} \tag{5.33}$$

If both criteria are satisfied, the observed triangle $\triangle ijk$ and the local catalog triangle $\triangle pqr$ are matching.

Now, the algorithmic framework by which the observed stars are identified can be produced. The procedure is shown in the flowchart given in Figure 5.4 for clarity. To start, an observed star $(\widetilde{s}_i)$ is selected to be identified. Next, another observed star $(\widetilde{s}_j)$ is selected, such that $i \neq j$. And lastly, a third star $(\widetilde{s}_k)$ is selected such that $i \neq k$ and $j \neq k$. The observed pattern set $(\widetilde{P}_{i,j,k})$ is computed for the observed star combination. The matching criteria given in Equation 5.33 are then evaluated for all permutations (p, q, r) such that $p \neq q \neq r$. All unique combinations (p, q, r) that satisfy the conditions are stored. If there exists one possible combination, then a unique match $(i, j, k) \longrightarrow (p, q, r)$ has been found. This is unlikely for the first

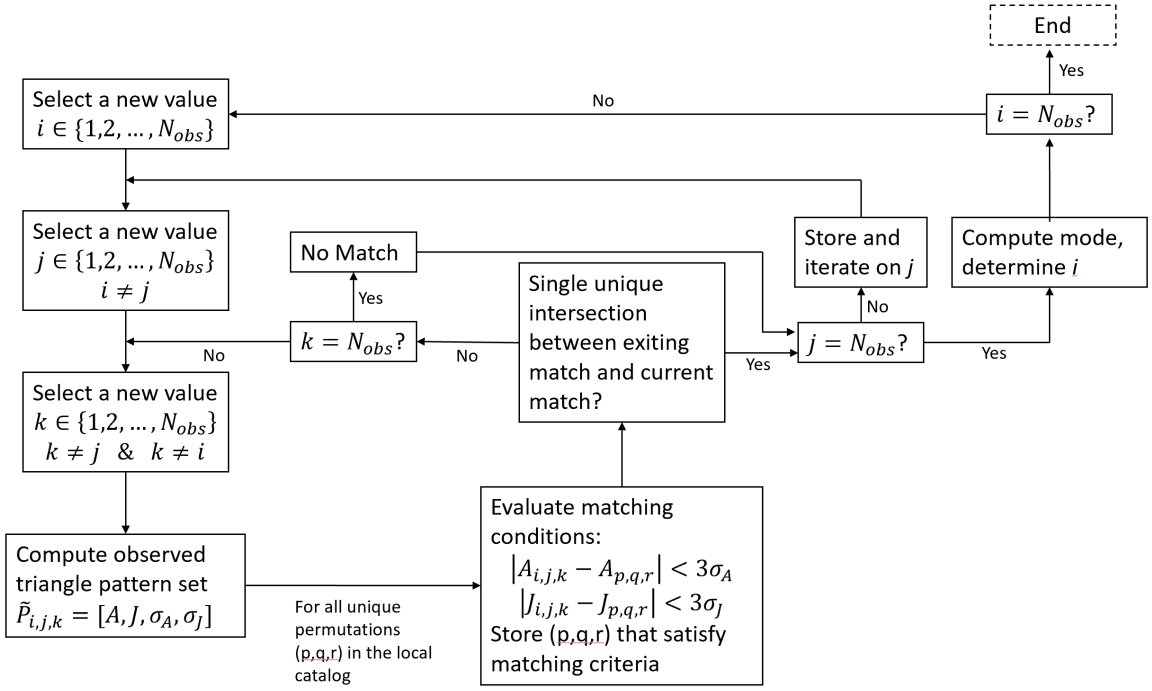

Figure 5.4.. Flowchart of the star identification algorithm. This procedure is conducted given a set of observed stars and a local star catalog containing candidate stars in the expected field of view.

attempt, so in the vast majority of cases, a *pivot* is required. This pivot is a new triangle formed by the same value (i, j), but a new $k = k'$. This is shown in Figure 5.5. The same procedure is conducted with the pivot, and a new set of unique combinations (p', q', r') that satisfy the matching criteria is formed. The intersection of the new set and the previous set is determined and fed forward. Because the new k' corresponds to a different observed star, it is expected that the intersection should contain pairs: $(i, j) \longrightarrow (p, q)$, as (i, j) remains fixed. This procedure is conducted iteratively until a unique match $(i, j) \longrightarrow (p, q)$ is found. Once a unique match is found, or all pivots have been exhausted, j is stepped forward and the procedure is conducted again. Once all $j \neq i$ have been evaluated for a given star i the most likely match can be determined. The mode of the set formed by all unique pairs (p, q) for a fixed value of i over the range of all possible j is used as the best match to the local catalog. It is

beneficial to install a minimum value for the mode to define a match. Positive results have been found using a cutoff of $\geqslant N_{obs}/2$.

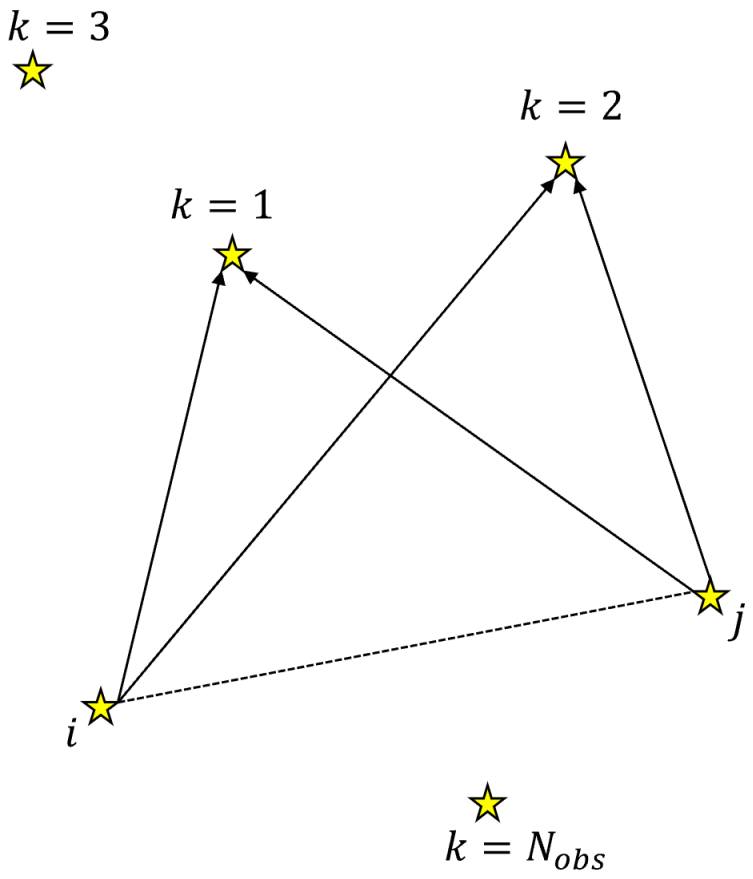

Figure 5.5.. A pair of stars i, j generates two pivots shown above for $k = 1$ and $k = 2$. Pivots may be generated for all $k \neq i$ and $k \neq j$ until the number of observed stars is reached.

5.4 Determination of the Optimal Transformation

With at least three observed stars identified, the optimal transformation from pixel coordinates to astronomical topocentric coordinates can be determined. Equation 5.5 defines the transformation, and shows that any position in pixel coordinates can be transformed to topocentric right ascension and declination, provided a field rotation

(θ) and the astronomical topocentric coordinates of the field center can be determined. In this step, the optimal estimate of these parameters will be found, such that the square difference between the transformed measured star positions and the matched local catalog star positions is minimized. The full transformation (including the rotation) is nonlinear, so an iterative procedure using the LUMVE solution provided in Chapter 2 is used. The parameter set to be estimated is defined as:

$$\hat{x} = \begin{bmatrix} \hat{\theta} \\ \hat{\alpha}_0 \\ \hat{\delta}_0 \end{bmatrix} \tag{5.34}$$

where $\hat{\theta}$ is the field rotation estimate, and $\hat{s}_0 = [\alpha_0 \ \delta_0]^T$ is the astronomical coordinate estimate of the field center. This makes the resultant estimated position of the i^{th} observed star:

$$\hat{s}_i = \begin{bmatrix} \hat{\alpha}_i \\ \hat{\delta}_i \end{bmatrix} = \tau \begin{bmatrix} \cos(\hat{\theta}) & -\sin(\hat{\theta}) \\ \sin(\hat{\theta}) & \cos(\hat{\theta}) \end{bmatrix} \left(\begin{bmatrix} x_i \\ y_i \end{bmatrix} - \begin{bmatrix} 2048 \\ 2048 \end{bmatrix} \right) + \begin{bmatrix} \hat{\alpha}_0 \\ \hat{\delta}_0 \end{bmatrix} \tag{5.35}$$

in astronomical topocentric coordinates. It is worth noting that the estimate being produced is for a uniform pixel grid with a linear mapping produced from the theoretical pixel scale. More complex effects such as image shearing are not included in the model. The magnitude of expected error resulting from forgoing the nonlinear projection are expected to be less than a tenth of a pixel, as shown in Section 5.2. The residuals for the measured star position using the estimated parameter set are given by:

$$\epsilon_i = \vec{s}_p - \hat{s}_i, \tag{5.36}$$

where $\vec{s}_p$ is the position of the matching star found in the local catalog. To apply the LUMVE update, the Jacobian of Equation 5.35 with respect to the parameter set () must be derived. The partials are straightforward to obtain:

$$\boldsymbol{H}_i = \begin{bmatrix} \frac{\partial \hat{\alpha}_i}{\partial \hat{\theta}} & \frac{\partial \hat{\alpha}_i}{\partial \hat{\alpha}_0} & \frac{\partial \hat{\alpha}_i}{\partial \hat{\delta}_0} \\ \frac{\partial \hat{\delta}_i}{\partial \hat{\theta}} & \frac{\partial \hat{\delta}_i}{\partial \hat{\alpha}_0} & \frac{\partial \hat{\delta}_i}{\partial \hat{\delta}_0} \end{bmatrix} \tag{5.37}$$

$$\begin{aligned}
\frac{\partial \hat{\alpha}_i}{\partial \hat{\theta}} &= -\tau\Big(\sin(\hat{\theta})x_c + \cos(\hat{\theta})y_c\Big) \\
\frac{\partial \hat{\alpha}_i}{\partial \hat{\alpha}_0} &= 1 \\
\frac{\partial \hat{\alpha}_i}{\partial \hat{\delta}_0} &= 0
\end{aligned} \tag{5.38}$$

$$\begin{aligned}
\frac{\partial \hat{\delta}_i}{\partial \hat{\theta}} &= \tau\Big(\cos(\hat{\theta})x_c - \sin(\hat{\theta})y_c\Big) \\
\frac{\partial \hat{\delta}_i}{\partial \hat{\alpha}_0} &= 0 \\
\frac{\partial \hat{\delta}_i}{\partial \hat{\delta}_0} &= 1
\end{aligned} \tag{5.39}$$

Now, the LUMVE solution can be applied to update the parameter set. Taking the same value for measurement covariance as the previous section ($\boldsymbol{R}$), the update for the parameter set is:

$$\delta\hat{x} = (\boldsymbol{H}^T\boldsymbol{H})^{-1}\boldsymbol{H}^T\vec{\epsilon} \tag{5.40}$$

$$\vec{\epsilon} = \begin{bmatrix} \epsilon_1 \\ \epsilon_2 \\ \vdots \\ \epsilon_{N_{match}} \end{bmatrix} \qquad \boldsymbol{H}_i = \begin{bmatrix} \boldsymbol{H}_1 \\ \boldsymbol{H}_2 \\ \vdots \\ \boldsymbol{H}_{N_{match}} \end{bmatrix}, \tag{5.41}$$

where N_{match} is the number of observed stars identified in the local catalog. This procedure is conducted iteratively until a sufficiently small update step is produced. The procedure can be initialized with the pointing direction and the relatively stable field rotation value produced from previous observations.

A few important notes pertaining to the application of this algorithm remain. Firstly, the catalog matches must be unique. If the local catalog does not contain an observed star, or the pattern set produced closely mirrors that of another star, it is possible that a false positive match is produced for one star while a true positive match is produced for another. If this is the case, there does not exist a solution that can produce acceptable error, because the map is not one-to-one. If this is the

case, the match with a larger mode is selected and the false positive is scrapped, as the identification step has provided more confidence in this match. Secondly, the match threshold that specifies the minimum possible value of the mode for a positive identification can be modified based on the frequency of false positives. Lastly, the measurement covariance $\boldsymbol{R}$ depends on several factors, including: observed star magnitude, atmospheric conditions, and noise levels due to background light sources on a given night. A nominal value used for most observations is $\boldsymbol{R}_{i,j} = (2.5)^2\delta_{ij}$ arcseconds^2. This equates to a positional error of approximately 3.45 pixels in any one direction. This value may be modified based on any number of criteria to improve performance.

Once the optimal parameter set has been determined, the transformation between pixel coordinates and astronomical topocentric coordinates can be performed for all pixel values contained in the field. This means the RSO centroids found in the image processing steps can be positioned with a certainty.

5.5 Existing Tools for Plate Solving

There exist several commercially available tools to conduct plate solving procedure. One such tool is Astrometry.net, which provides an open source platform for astronometric data [18]. The most accessible mode of operation allows users to upload images and receive the astronometric information through the API. The code can also be run locally using a Linux, unix, or Mac machine, or on a windows machine using cygwin. Once the code is correctly configured on the local device, images can be processed locally. Using the image as an input leaves the image processing up to Astrometry.net, which for the satellite tracking mode used in this study is problematic. The system was not developed for tracking satellites, and does not provide consistent results when all of the stars in frame are streaked. For this reason, the FITS binary table input mode is used. This option allows the user to conduct the image processing step, and provide the star pixel locations in an array as an input.

The image processing step developed for this study provides the COL of all stars in frame, which can be used as the input for the Astrometry.net plate solver. To use this option the pixel dimensions of the CCD (4096×4096) are also required as an input. The output of this procedure is the same as the plate solving method developed in this chapter: a transformation from pixel coordinates to topocentric astronomical coordinates.

6. RESULTS FROM THE PROCESSING PIPELINE

The prior chapters have rigorously defined methods by which astronomical observations can be made, star and satellite pixel coordinates can be extracted from observations, and the extracted positions in the frame can be transformed to astronomical coordinates. A classical method for angles-only initial orbit determination, as well the nonlinear least squares batch processor for orbit improvement have been presented in the background material. All of these procedures can now be combined to make the data-processing pipeline for the Purdue Optical Ground Station. This data processing pipeline takes in a series of FITS files containing the observation and associated metadata. The desired output is the state estimate and associated statistical information for the target RSO at the time of the first observation. The flowchart given in Figure 6.1 shows the steps contained in the processing pipeline, referenced as they have been defined in the previous chapters.

The data extraction step is conducted sequentially until the entire batch of observations has been processed. This sequence starts with the image processing step provided in Chapter 4. The procedure categorizes and positions all image objects in the frame. These positions are then passed to the astrometry and plate solving step defined in Chapter 5. This procedure produces an accurate transformation from pixel coordinates to topocentric astronomical coordinates. The astronomical coordinates and time of the observation can then be stored for use in the orbit determination step. Once all of the observations have been processed, a set of measurements and the time they are made can be passed to the orbit determination step. It is assumed that a minimum of 3 observations have been successfully processed. The Laplace initial orbit determination method is used with the first, middle and final observation. This estimate is then back propagated to the initial time to produce the initial orbit estimate. This is then improved with the nonlinear leas squares batch proces-

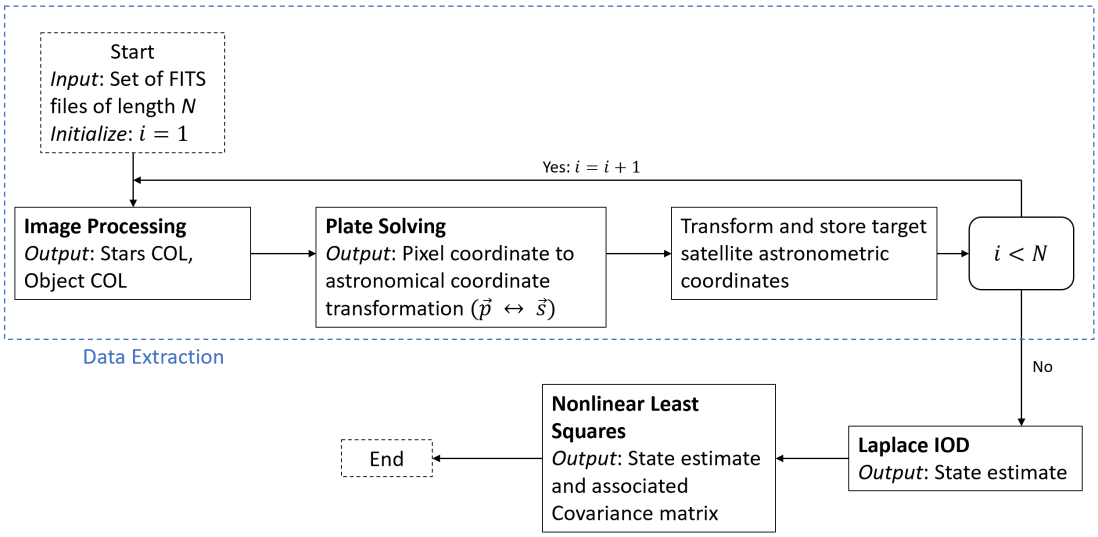

Figure 6.1.. Flowchart of the steps for processing a batch of observations used to conduct the orbit determination procedure.

sor. The orbit determination step is demonstrated using simulated measurements in Section 2.6.

Results from the processing pipeline are presented in the following for two observation series: one of the GPS satellite Navstar 76 and one of the geostationary object from the simulated example, Amazonas3. A GPS satellite has been selected as a means of assessing the accuracy of the processing pipeline, because reliable ephemeris data is available for all active GPS satellites. A GEO object has been selected because the high population of debris objects in this regime has caused it to become an area of interest.

6.1 GPS Satellite: Navstar 76

Navstar 76 is an operational satellite in the GPS constellation. The satellite can also be found as any of the following:

- Space Vehicle Number (SVN) 70

- Satellite Catalog Number: 41328U
- International Designator: 16007A

Currently, Navstar 76 is broadcasting Pseudorandom Noise Code (PRN) 32 [41]. The GPS constellation is composed of 6 orbital planes, equally spaced in 60° intervals of right ascension of the ascending node. The core constellation provides 4 slots in each orbital plane, making a total of 24 operational GPS satellites at any given time to provide full coverage. Normally more than the minimum required number of 24 operational satellites are in service at a time.

GPS satellite ephemerides are published by the International GNSS Service (IGS) daily. Broadcast ephemeris data that is accurate to roughly 100 cm is published in real-time, while more accurate data is published at increasing degrees of latency. The finalized solution is published 12-18 days after the date of observation and provides position accuracy of approximately 2.5 cm [42]. The position of all operational satellites by PRN is provided for a full day in intervals of 15 minutes in ECEF coordinates. The position at the specified time interval can be coordinated to ECI using Equation 2.13. There is a problem with the application of the GPS ephemeris: the epoch of each entry in the GPS ephemeris is not likely to overlap with observation schedules. Moreover, satellite velocity information is not provided in the ephemeris, which means that there is not enough information to propagate the satellite state. To make use of the IGS ephemerides, a method of producing accurate positions at a specified reference time is required. To this end, a means of acquiring velocity information at the ephemeris time is sought.

The problem posed here is essentially a two point boundary value problem. A start point, an end point, and the time of flight between the two points is know, but the initial state defining a trajectory that meets these criteria is not. A numerical method of approximating the initial velocity required to produce this path is known as a fixed point, fixed time targeter [21]. The procedure requires a fixed initial position ($\vec{r}_0$), a fixed final position ($\vec{r}_d$) (or target), and a fixed time of flight (t_f). A guess of

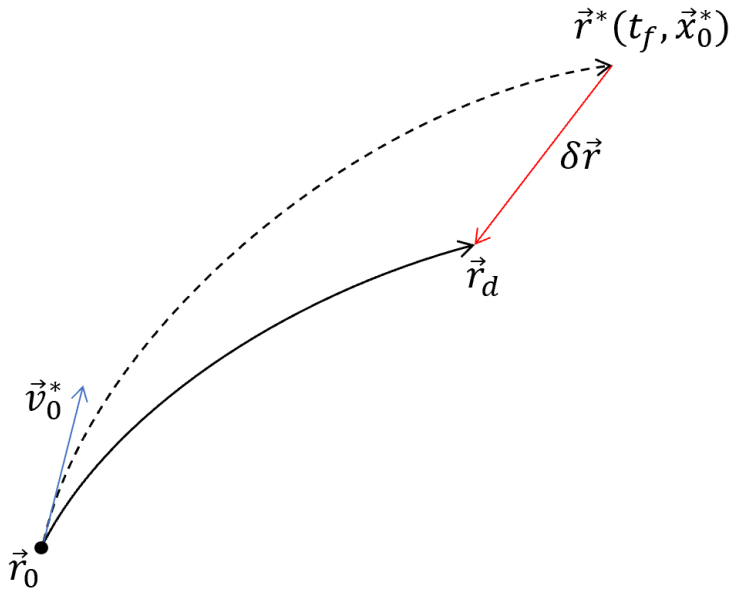

Figure 6.2.. Two dimensional depiction of the fixed point, fixed time targeter problem. The initial point $\vec{r}_0$ is known. An initial velocity $\vec{v}_0$ that produces a final position of $\vec{r}_d$ after a specified time of flight t_f is sought. The procedure updates the dotted reference trajectory iteratively until $\delta\vec{r}$ is sufficiently small.

the initial velocity is provided, and an iterative corrector is applied until an initial velocity is produced that will hit the target at the given final time within a specified tolerance. The free variables are given as:

$$\vec{X} = \begin{bmatrix} \dot{x}_0 \\ \dot{y}_0 \\ \dot{z}_0 \end{bmatrix}, \tag{6.1}$$

where $\vec{X}$ are the variables that the targeter is trying to be optimized; not to be mistaken as the state vector $\vec{x}$. The constraint equation to be minimized is given as:

$$\vec{F} = \begin{bmatrix} x_d - x^* \\ y_d - y^* \\ z_d - z^* \end{bmatrix} \longrightarrow \begin{bmatrix} 0 \\ 0 \\ 0 \end{bmatrix}, \tag{6.2}$$

where (x^*, y^*, z^*) is the final position on the reference trajectory produced by propagating the initial reference state ($\vec{x}_0^* = [\vec{r}_0 \ \vec{v}_0^*]$). This makes it clear that the free variables (initial velocity) directly affect the resultant value of $\vec{F}$. The value of $\vec{F}$ for $\vec{v}_0^*$ in the vicinity of $\vec{v}_d$ can be approximated via first-order Taylor-series.

$$\vec{F}(\vec{X}) \approx \vec{F}(\vec{X}^*) + \nabla\vec{F}(\vec{X}^*)(\vec{X} - \vec{X}^*) \tag{6.3}$$

Because this is a linear approximation of the deviation applied to a nonlinear dynamic system, the procedure to produce $\vec{F}(\vec{X}) = \vec{0}$ must be conducted iteratively. The update equation is produced by rearranging the Taylor series approximation to target a constraint equation that produces zero error. This gives the update equation in its general form:

$$\vec{X}_{j+1} = \vec{X}_j - \left(\nabla\vec{F}(\vec{X}_j)\right)^{-1}\vec{F}(\vec{X}_j). \tag{6.4}$$

For the problem of the fixed-point, fixed-time targeter, the constraint equation Jacobian is given as:

$$\nabla\vec{F}(\vec{X}_j) = \frac{\partial\vec{r}}{\partial\vec{v}_0}. \tag{6.5}$$

This 3×3 matrix is the upper right portion of the state-transition matrix $\mathbf{\Phi}$. The state transition matrix can be computed along with the reference trajectory, which is governed by the following:

$$\dot{\vec{x}} = \boldsymbol{A}(t)\vec{x} \tag{6.6}$$

$$\mathbf{\Phi}(t, t_0) = \begin{bmatrix} \frac{\partial\vec{r}}{\partial\vec{r}_0} & \frac{\partial\vec{r}}{\partial\vec{v}_0} \\ \frac{\partial\vec{v}}{\partial\vec{r}_0} & \frac{\partial\vec{v}}{\partial\vec{v}_0} \end{bmatrix} \tag{6.7}$$

$$\dot{\mathbf{\Phi}}(t, t_0) = \boldsymbol{A}(t)\mathbf{\Phi}(t, t_0). \tag{6.8}$$

This produces the following for the update equation:

$$\begin{bmatrix} \dot{x}_0 \\ \dot{y}_0 \\ \dot{z}_0 \end{bmatrix}_{j+1} = \begin{bmatrix} \dot{x}_0 \\ \dot{y}_0 \\ \dot{z}_0 \end{bmatrix}_j - \left(\frac{\partial\vec{r}}{\partial\vec{v}_0}\right)_j^{-1} \begin{bmatrix} x_d - x(t_f) \\ y_d - y(t_f) \\ z_d - z(t_f) \end{bmatrix}_j, \tag{6.9}$$

which is computed until $\vec{F}_j$ meets the specified tolerance.

This procedure is applied to every point in the ephemeris, starting with the first entry. This provides a velocity approximation for every point in the ephemeris excluding the final one, as it does not have a future point to target. This is not a problem, as it will be shown that the observations do not occur near this time, so a velocity is not needed. The velocity guess used to initialize the targeter at each attempt is provided using the norm of the position assuming the object is in a circular orbit to provide a magnitude. It is directed to be in plane with the current and next position and orthogonal with the radial unit vector. The nominal GPS orbit is circular, so this proves to be a sufficiently good initialization, as all targeting attempts meet the specified tolerance of 1×10^{-10} km in under 5 iterations. Although the specified tolerance is low, the satellite state is propagated using two-body motion, which is not completely representative. Over the 15 minute time intervals between ephemeris entries, it is expected that the error in position will be greater than 2.5 cm, but still orders of magnitude less than that of the TLE propagation.

```
0 NAVSTAR 76 (USA 266)
1 41328U 16007A   20060.41526436 +.00000026 +00000-0 +00000-0 0  9999
2 41328 054.8223 180.7614 0037743 218.8265 140.8919 02.00561808029763
```

Figure 6.3.. TLE for Navstar 76 at a reference epoch of approximately 11 minutes before the initial observation.

In addition to the IGS ephemerides, the TLE for Navstar 76 is also available and is provided in Figure 6.3. The TLE provides all the information necessary to propagate from the reference epoch to a specified time. The accuracy of a TLE can vary widely by object, and no statistical information is provided [10]. To quantify the accuracy of the TLE, the satellite state has been propagated to all of the times provided in the IGS ephemeris. As stated, the IGS ephemeris entries are accurate to within 2.5 cm, so deviations larger than this can be attributed to TLE error. Clearly, the deviations in TLE propagated position from the provided IGS ephemeris position

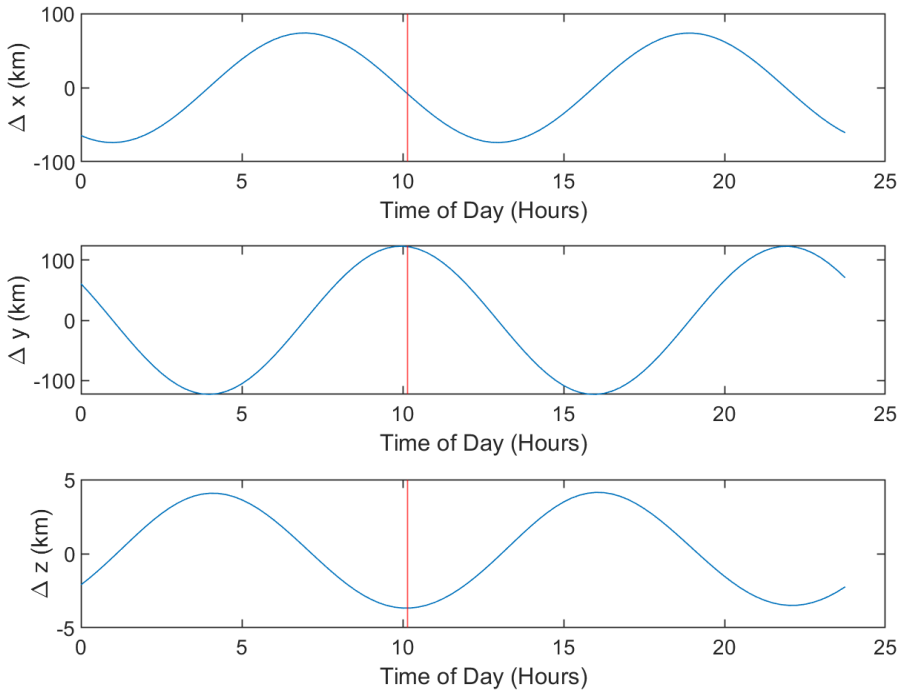

Figure 6.4.. Deviation of TLE propagation from GPS ephemeris data over the full day February 29, 2020. The component-wise deviation in position is shown in 15 minute intervals. The maximum deviation is found to be approximately 123 km and occurs at 10:00. The time of first observation is shown as the red vertical line, and happens to be near the time of maximum deviation.

can be attributed to TLE error, as the deviations are expressed in km. This validates the need for more reliable SSA information. Most satellites do not have ephemeris data accurate to the level of GNSS applications; and without statistical information provided in the TLE accuracy of the resultant solution cannot be assessed. To follow, the accuracy of the solution produced by the processing pipeline will be compared to that of the solution provided by the TLE.

An observation series was conducted in the early morning hours of February 29, 2020 for roughly 1 hour and 8 minutes, producing a total of 300 observations. Observation conditions throughout the series prove to be difficult for the plate solving

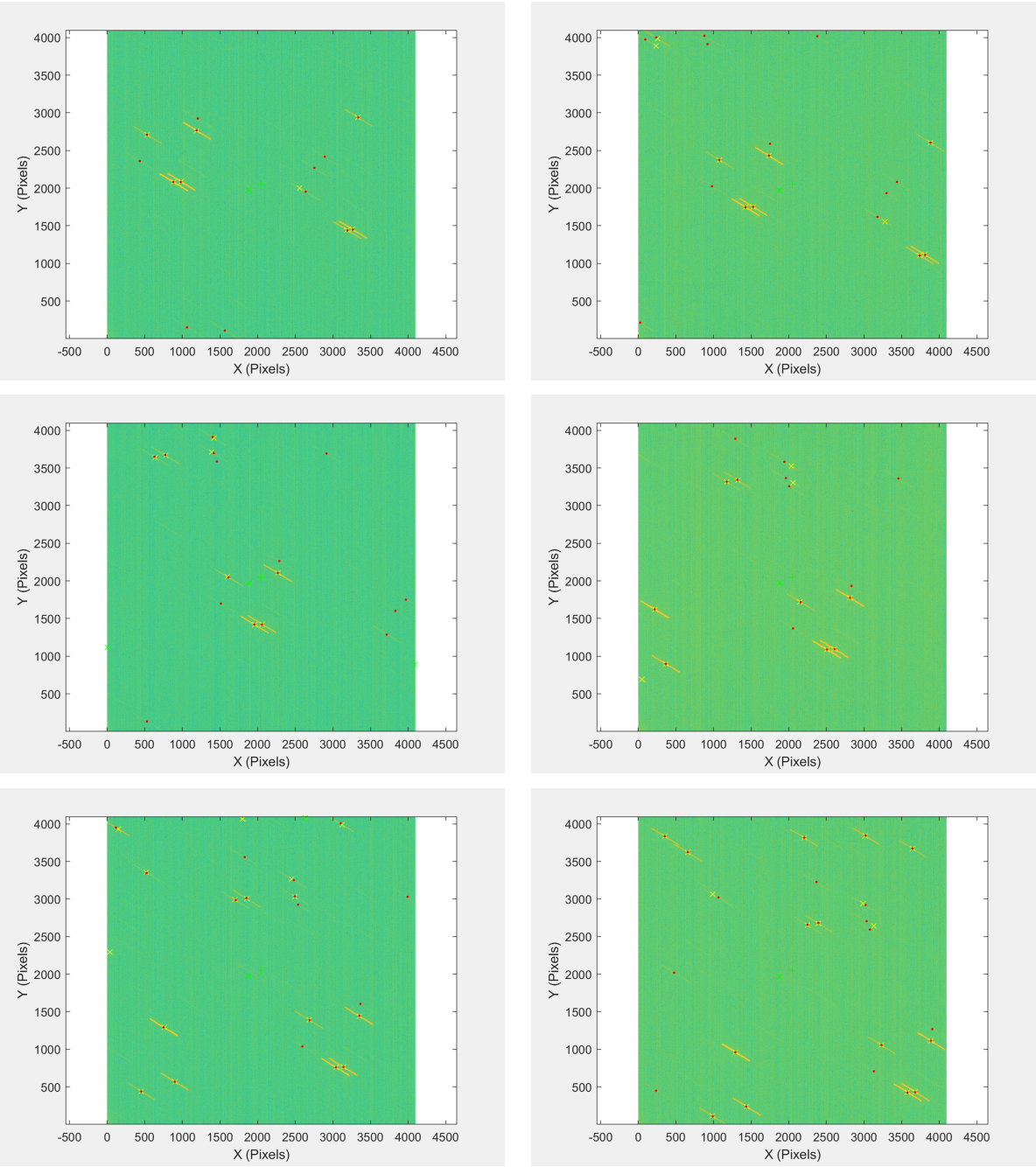

Figure 6.5.. Six selected resolved observation from the observation series of Navstar 76. In each image, yellow ×'s indicate observed stars, green ×'s indicate observed objects, red dots indicate catalog stars transformed to pixel coordinates, and the green + is the center of the frame.

procedure, as few stars were captured in frame, and the portion of the sky being viewed does not contain many catalog entries. The observations were visually curated prior to analysis, producing a set of 93 potentially solvable images. Out of the 93 observations fed into the system 37 produced adequate results (just under 40%). In more favorable observation scenarios the plate solving procedure has a much higher rate of success, as will be shown in the following section.

To compare the results from the processing pipeline to the IGS ephemeris and TLE solutions, they are each propagated to the time of the extracted measurements. In the case of the IGS ephemeris, the entry with time nearest to that of the measurement is used to produce what will be used as the "true" state. The states produced by the TLE and IGS ephemeris propagation can be used to generate topocentric right ascension and declination using Equation 2.41.

The extracted measurements are plotted as a function of observation time in Figure 6.6. The expected measurements resulting from the TLE and IGS propagation are also plotted as a function of observation time. The measured right ascension follows the IGS ephemeris curve closely, while the TLE right ascension shows a clear offset. In the case of declination, the inverse is observed as the TLE follows closely, but the measured declination is offset. The statistics of the deviations from the IGS measurements are provided in Table 6.1. This offset can be seen in the rows corresponding to the measured declination and TLE right ascension, as the mean and max deviation are of a similar value. Although the offset in measured declination is linear, it is larger than expected. The source of this observed offset is currently unknown, but the suspected source is the stellar aberration correction in the Tycho-2 catalog. Aberration is an effect produced as light travels from a emission source to a moving observer. The motion of the Earth about the sun produces a periodic effect, which is corrected in star catalogs to make them independent of reference epoch. While the star catalogs are aberration-free, the IGS ephemeris and TLE are not.

The angular measurements can now be used to conduct the orbit determination procedure as it was presented in Section 2.6. Figure 6.7 shows the resulting solu-

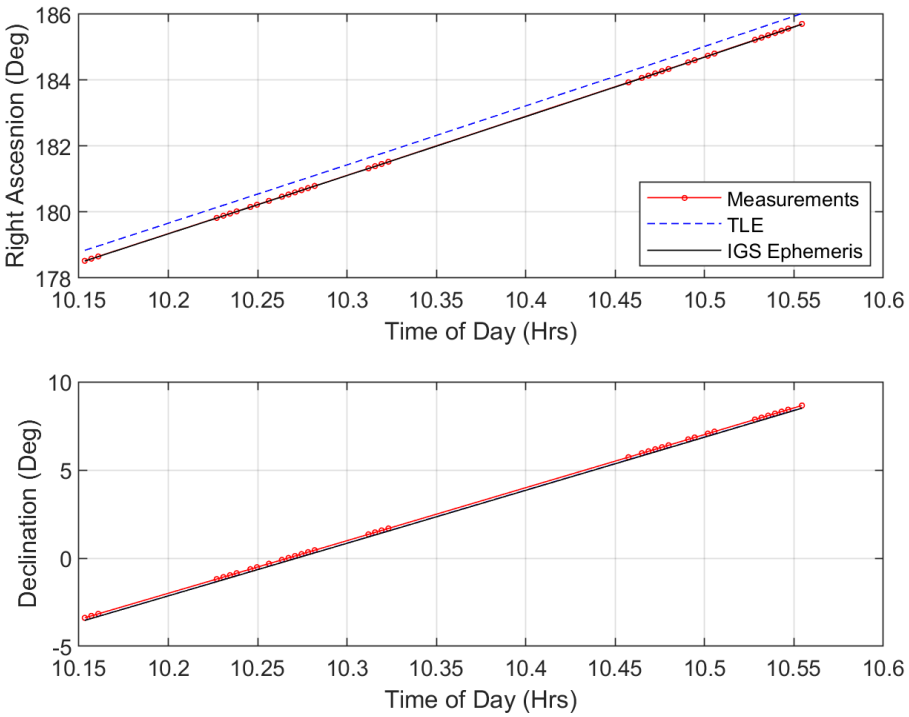

Figure 6.6.. Angular measurements extracted from the observation series plotted against observation time, given in UTC. Additionally the measurements generated using the propagated TLE and IGS ephemeris data are provided.

tion propagated for a full period along with the IGS ephemeris. The positions at times of observation are also indicated for both the IOD and improved solution. The initial state estimate resulting from the IOD and the improvement are presented alongside the ephemeris and TLE propagated states in Table 6.2. From the table and Figure 6.7, it is clear that the least squares batch processor has improved the state estimate significantly when compared to the IOD solution. The component-wise deviation from the IGS ephemeris propagated state is presented in Table 6.3. The TLE position deviation along the y axis is large, and representative of the large offset in right ascension seen in Figure 6.6. The processing pipeline position estimate in the z direction shows a large deviation resulting from the declination offset seen in

Table 6.1.. Deviations of the measurements extracted from the observation series and TLE generated measurements from the true measurements generated using the IGS ephemeris. All angular values are reported in arcminutes.

		Mean	**Standard Deviation**	**Max**
Observed	$\Delta\alpha$	0.515221	0.129766	0.767652
Measurements	$\Delta\delta$	9.08297	0.078904	9.23161
TLE	$\Delta\alpha$	19.4902	0.055182	19.5752
Measurements	$\Delta\delta$	0.677378	0.128037	0.85287

Figure 6.6. The position estimate produced by the processing pipeline provides an overall deviation that is about 48% the size of the overall TLE position deviation. The velocity deviation in the TLE is seen to be marginally better, as the overall TLE velocity deviation is 91% the size of the processing pipeline result.

Table 6.2.. Initial state of Navstar 76 provided by the propagated ephemeris and TLE, as well as the estimate provided by the processing pipeline.

	x (km)	y (km)	z (km)	$\dot{x}$ (km/s)	$\dot{y}$ (km/s)	$\dot{z}$ (km/s)
IGS Ephemeris	-26503.7	-1721.9	2117.77	0.387586	-2.21035	3.14301
TLE	-26495.2	-1844.47	2121.45	0.398262	-2.20843	3.14299
Measurement IOD	-27349.6	-1700.76	2143.13	0.373981	-2.27662	3.25946
Measurement Orbit Improvement	-26490.6	-1724.69	2175.49	0.399151	-2.20945	3.14036

In addition to a state estimate, the processing pipeline produces a state estimate covariance matrix. This provides the user with the statistical information needed to asses the quality of the estimate. If the state is normally distributed, the user can be

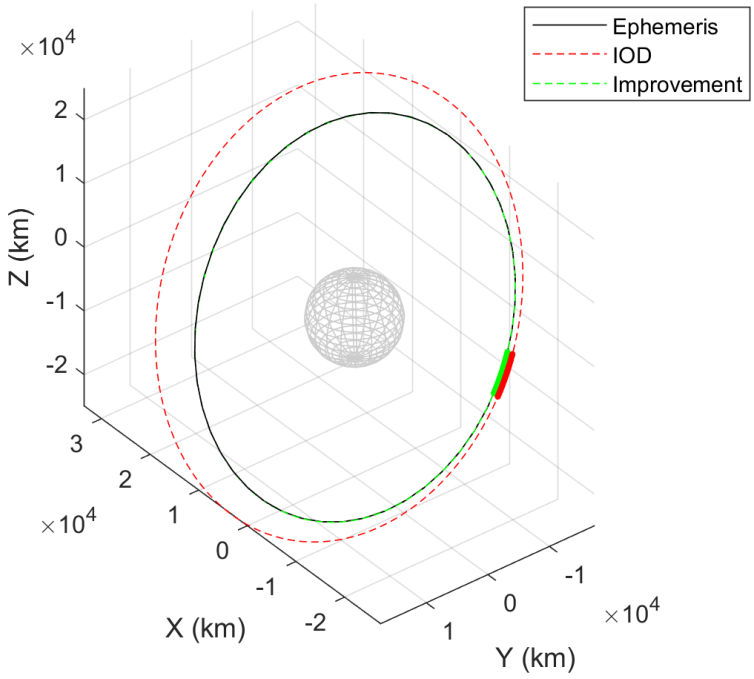

Figure 6.7.. The orbit produced using the observations made at the POGS is plotted with the IGS ephemeris. The thicker portion of the orbits indicate the position during the time of observation.

Table 6.3.. Deviation of initial state estimate from the IGS ephemeris. Component-wise deviations presented for the propagated TLE and the state estimate produced by the processing pipeline.

	Δx (km)	Δy (km)	Δz (km)	$\Delta \dot{x}$ (m/s)	$\Delta \dot{y}$ (m/s)	$\Delta \dot{z}$ (m/s)
TLE	-8.46205	122.571	-3.67409	-10.6765	-1.91417	0.0138567
Measurement IOD	845.924	-21.1418	-25.3572	13.6044	66.2751	-116.457
Measurement Orbit Improvement	-13.0441	2.78376	-57.7145	-11.5648	-0.892829	2.64507

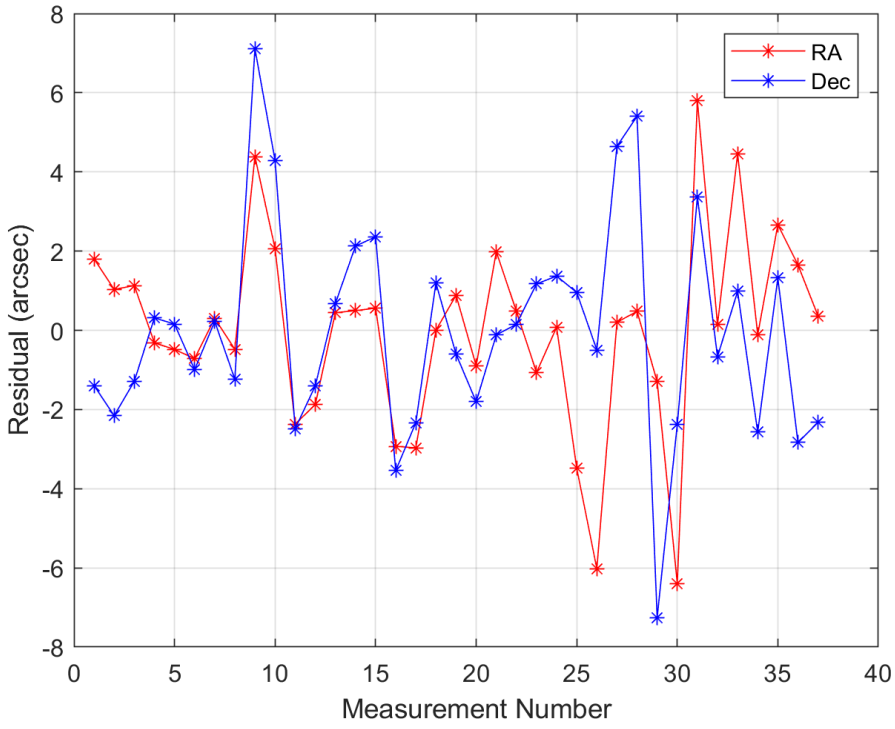

Figure 6.8.. Residuals produced by the final iteration of the least squares procedure. The proposed trajectory is in agreement with the measurements at the arcsecond level.

Table 6.4.. Component-wise deviation of the processing pipeline state estimate from the IGS ephemeris state, as well as the 3σ bounds produced using the covariance matrix output by the orbit improvement step.

	x (km)	y (km)	z (km)	$\dot{x}$ (m/s)	$\dot{y}$ (m/s)	$\dot{z}$ (m/s)
$\Delta\vec{x}_i$	-13.0441	2.78376	-57.7145	-11.5648	-0.892829	2.64507
$3\sigma_i$	450.857	11.4763	26.493	9.46411	37.5682	63.9817

99.7% certain that the true state falls within the region surrounding their estimate defined by the 3σ bounds. As shown, the deviation of all estimated states from the true initial state are contained in the associated 3σ bounds, excluding the z position

estimate and x velocity estimate. The z position falling outside of the 3σ bound is to be expected considering the offset in declination shown in Figure 6.6. The orbit improvement step is able to find a solution that is correlated with the measurements provided from the data extraction step, which is why the 3σ bound is reasonably low. The issue with this is that the declination measurements are offset from the ephemeris generated measurements by approximately 0.15 degrees at each point. The range of the satellite can be computed at the initial time of observation using the ephemeris data, which provides $\rho \approx 21690.218$ km. This means the expected error in z position due to the linear offset in the measured declination is:

$$\tan(\Delta\delta') = \frac{d}{\rho}$$
$$d \approx (21690.218)\tan(0.15^\circ) = 56.8km.$$

This value covers most of the observed error in z position shown in Table 6.4. The source of this linear offset in declination and whether or not the offset is repeatable and stable is currently unknown and requires that more observation series of satellites with precise ephemerides be processed.

The x velocity falling outside the bound is likely the result of the targeting procedure. The deviation is not far outside of the 3σ bound, and is in good agreement with the TLE velocity. The velocity approximation produced by the targeter is taken as the truth, but does have some nonzero error. It is expected that this is still the most representative of the satellites actual velocity, but the error that is present may be sufficiently large to have pushed the estimate outside of the 3σ bound.

Overall, the evidence available suggests that the state estimate provided by the processing pipeline for Navstar 76 produces accurate results. The position estimate when compared to the IGS ephemeris data is more accurate than propagated TLE positions, despite observed deviations in measured declination. The velocity estimate produced by the processing pipeline is marginally worse than that of the propagated TLE; although more accurate estimates of a true velocity are desired before definitive conclusions can be drawn. Further investigation needs to be conducted on the source

of the offset in measured declination. Although the solution produced by the orbit determination step was in fact closer to the IGS ephemeris position, the observed offset in declination is undesirably large.

6.2 Geostationary Satellite: Amazonas 3

Amazonas 3 is an operational communications satellite in the 61° W orbital position of GEO. The satellite can be found under the catalog number 39078U, or the international designator 13006A, as shown in the TLE below. Unlike the GPS satellite observed in the previous section, there does not exist publicly available ephemeris data that provides positions to a high degree of accuracy. Fortunately for operational objects in geostationary orbit, stringent station-keeping requirements exist, which are defined by the Federal Communications Commission (FCC). The contract outlining the operation of Amazonas 3 allows for a maximum longitudinal (East-West) tolerance of $\pm 0.05^\circ$ from its nominal position at 61° W. An additional inclination (North-South) tolerance of $\pm 0.07^\circ$ is provided. Moving forward, the nominal circular orbit with sidereal period equal to that of the Earth and zero inclination will be used as the truth model, as the satellite is known to be within a specified boundary of this location. The instantaneous truth state can be determined by converting the nominal ECEF position and velocity to ECI using Equation 2.13. To be precise, the nominal state at a given time in ECI is provided by the following:

$$\vec{r}_{ECEF} = r_{GEO} \begin{bmatrix} \cos(-61^\circ) \\ \sin(-61^\circ) \\ 0 \end{bmatrix} \tag{6.10}$$

$$\vec{v}_{ECEF} = \sqrt{\frac{\mu}{r_{GEO}}} \left(\frac{\hat{z} \times \vec{r}_{ECEF}}{r_{GEO}} \right) \tag{6.11}$$

$$\vec{r}_{ECI} = \Big(\mathbf{\Pi}(t) \mathbf{\Theta}(t) \boldsymbol{N}(t) \boldsymbol{P}(t) \Big)^{-1} \vec{r}_{ECEF} \tag{6.12}$$

$$\vec{v}_{ECI} = \Big(\mathbf{\Pi}(t) \mathbf{\Theta}(t) \boldsymbol{N}(t) \boldsymbol{P}(t) \Big)^{-1} \vec{v}_{ECEF}. \tag{6.13}$$

```
0 AMAZONAS 3
1 39078U 13006A   20032.25138253 -.00000275 +00000-0 +00000-0 0  9998
2 39078 000.0534 254.3900 0003248 026.0204 240.0023 01.00274011021544
```

Figure 6.9.. TLE for Amazonas 3 at a reference epoch of approximately 4 hours after the initial observation.

On the night of January 31, 2020 an observation series was conducted over the span of 5 hours and 25 minutes containing 1999 observations. A total of 174 sequential observations were taken from this observation series for processing.

The plate solving procedure for this image set is conducted using both the software developed for this study, as well as the local Astrometry.net software. Of the 174 images processed, the software developed here was able to solve 170 of the 174 images, producing a 97.7% rate of success. The local version of Astrometry.net was able to solve 90 of the 174 images, producing a 51.7% rate of success. This higher rate of success provided by the in-house plate solver allows for users to acquire more object measurements from an observation series, as far fewer need to be thrown out. Figure 6.10 shows six solved images using the plate solver developed for this study. The figures are arranged in sequential order going left to right, top to bottom. The star field is visibly more dense when compared to the observations shown in Figure 6.10. Four satellites are present in the observations, one of which is not picked up by the image processing step in this particular set of observations. The resultant extracted measurements correspond to the object that is circled in green.

The measurements provided by the data extraction step using both plate solvers are plotted with the measurements generated from the TLE in Figure 6.11. The right ascension and declination produced using the two plate solvers appear to be in agreement over the observation period. A visible offset in measured right ascension and TLE generated right ascension can be observed, much like in the case of the GPS observations shown in Figure 6.6. The deviations of the extracted measurements and the TLE generated measurements from the measurements generated using the

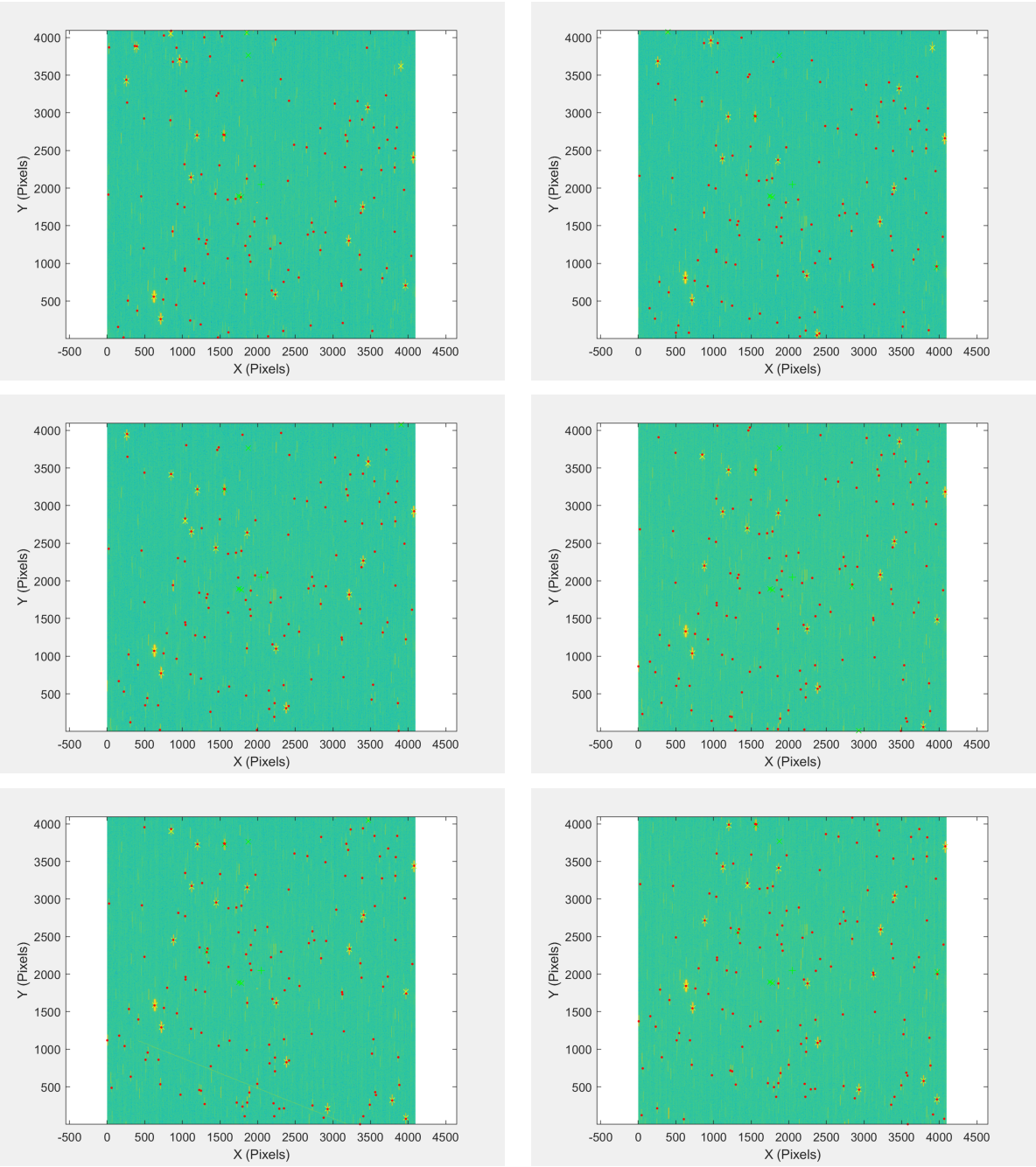

Figure 6.10.. Six observations solved by the in-house plate solver developed for this study. In each image, yellow ×'s indicate observed stars, green ×'s indicate observed objects, red dots indicate catalog stars transformed to pixel coordinates, and the green + is the center of the frame.

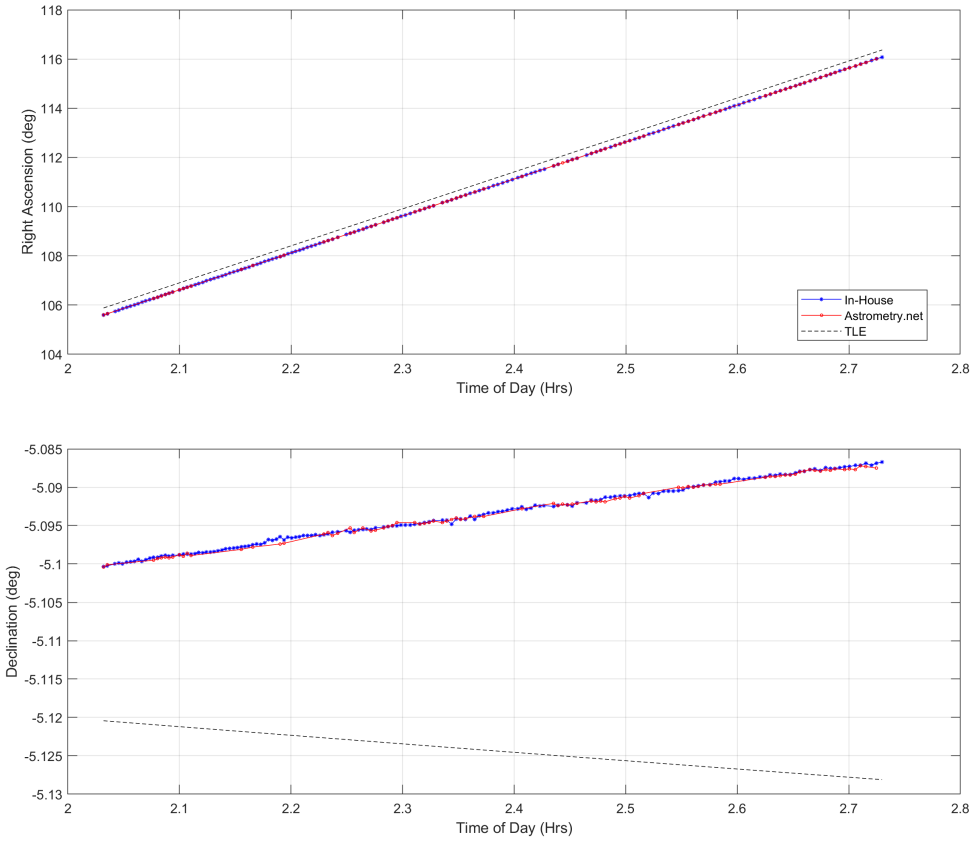

Figure 6.11.. Measurements of object topocentric right ascension and declination plotted against observation time in UTC. The measurements acquired from the processing pipeline using both the in-house plate solver developed for this work as well as the local Astrometry.net plate solver are shown. Additionally, the measurements generated using the TLE are provided.

satellite nominal position are provided in Table 6.5. The processing pipeline using the in-house plate solver out performs both the Astrometry.net plate solver and the TLE propagated solution in both right ascension and declination mean error. Note that the declination error observed when using the in-house plate solver is significantly smaller than the case of the GPS observation series. There are a few key differences between the observation series that may lend insight as to the source of the observed offset. The first is that the observed declination in the GEO observation scenario is

Table 6.5.. Deviations of the measurements extracted using both plate solvers in the processing pipeline and the TLE generated measurements from the measurements generated using the satellite nominal position. All angular values are presented in arcminutes.

		Mean	**Standard Deviation**	**Max**
In-House	$\Delta\alpha$	-0.0916408	0.144529	0.368481
Plate Solver	$\Delta\delta$	-1.29918	0.0955968	1.47532
Astrometry.net	$\Delta\alpha$	-0.120512	0.236333	0.617743
Plate Solver	$\Delta\delta$	-1.32942	0.0946456	1.50428
TLE	$\Delta\alpha$	17.0746	0.126733	17.2794
	$\Delta\delta$	-3.12318	0.467858	3.94851

relatively constant, while the observed declination rate in the GPS example is large. This is because the GPS nominal orbit is inclined 60 degrees. The second is that the tracking rate in the GPS observation scenario is larger, which may introduce unexpected error. Lastly, the relative velocity of the GPS satellite compared to the observer is significantly larger, which would make the effect of aberration larger. More observations need to be conducted to definitively determine the source of the observed declination offset.

The angular measurements can now be used to conduct the orbit determination procedure. Figure 6.12 shows the propagated initial state estimate for one full period. The top figure shows the solution found using the in-house plate solver and the bottom shows the solution found using the Astrometry.net solver. Both orbits are plotted with the propagated TLE. The component-wise initial state estimate for both plate solvers is shown in Table 6.6. As was shown in the previous section, the propagated TLE can be an unreliable source of state information, and thus is not used as a true state value by which the processing pipeline results can be evaluated through comparison. An alternative is to compare these values to the known nominal orbit for the satellite.

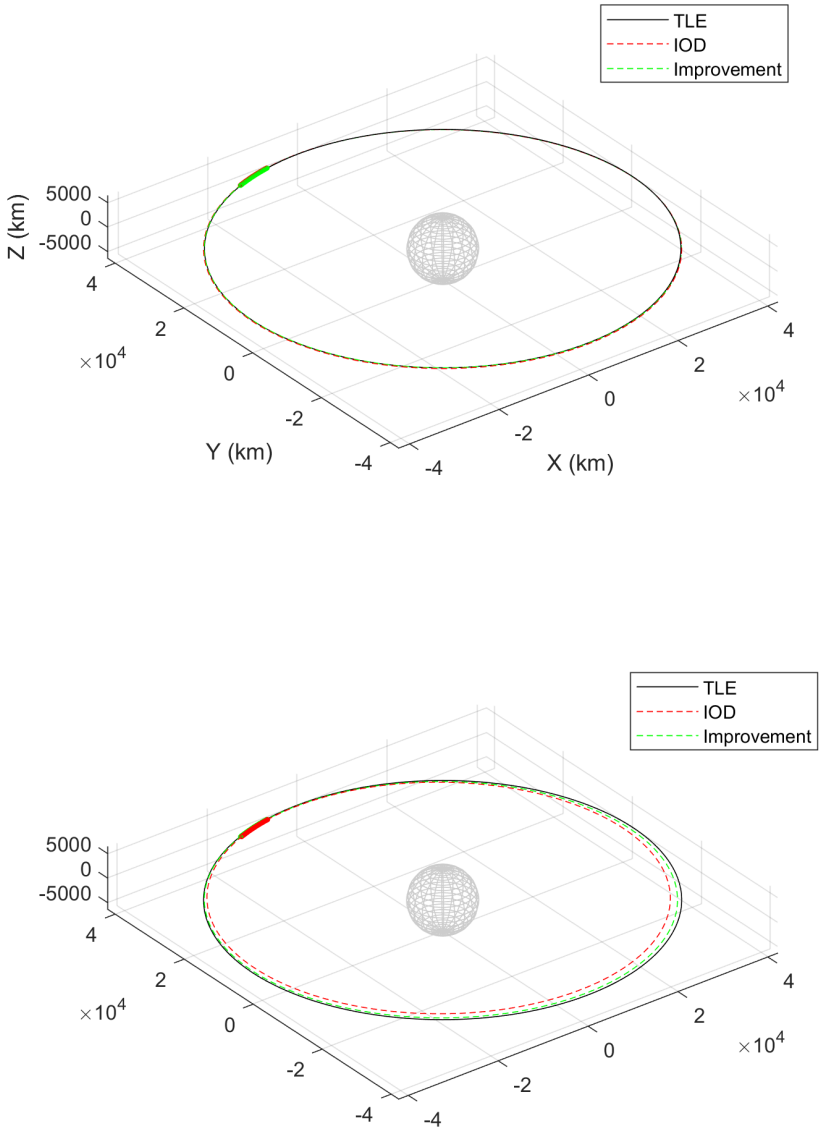

Figure 6.12.. The orbits produced using observations of Amazonas 3 are plotted with the propagated TLE. The top figure is uses observations processed using the in-house plate solver, while the bottom uses the Astrometry.net plate solver. The thicker portion of each orbit indicates the position during the observation series.

Table 6.6.. Initial state estimate produced by the processing pipeline and TLE propagation, as well as the nominal state at the time time of initial observation. Orbit solutions are produced using both plate solvers.

		x (km)	y (km)	z (km)	$\dot{x}$ (km/s)	$\dot{y}$ (km/s)	$\dot{z}$ (km/s)
Nominal		-7308.9	41525.7	14.4108	-3.02812	-0.532978	0.00581127
TLE		-7504.17	41504.4	-15.1711	-3.0247	-0.546873	-0.00155604
In-House Plate Solver	Measurement IOD	-7341.98	41587.1	10.7138	-3.0302	-0.52549	0.00286404
	Measurement Orbit Improvement	-7317.5	41551.1	-0.880242	-3.02828	-0.532351	0.00417386
Astrometry.net Plate Solver	Measurement IOD	-7259.86	41266.8	40.3895	-2.99849	-0.532226	0.0048189
	Measurement Orbit Improvement	-7282.82	41425.6	10.537	-3.02122	-0.52347	0.00386863

The nominal state and TLE propagated state and nominal state are both provided in Table 6.6.

Table 6.7.. Component-wise 3σ bounds produced using the state estimate covariance matrix from the orbit improvement step. The results from both plate solvers are presented. The deviation from nominal state at the time of observation is also provided.

		x (km)	y (km)	z (km)	$\dot{x}$ (m/s)	$\dot{y}$ (m/s)	$\dot{z}$ (m/s)
TLE	$\Delta\vec{x}_i$	195.27	21.3236	29.5819	-3.41656	13.895	7.3673
In-House	$\Delta\vec{x}_i$	8.59561	-25.4231	15.2911	0.167702	-0.627478	1.6374
Plate Solver	$3\sigma_i$	65.6475	234.915	21.548	14.8939	12.024	0.335523
Astrometry.net	$\Delta\vec{x}_i$	-26.0805	100.127	3.8738	-6.89658	-9.50799	1.94264
Plate Solver	$3\sigma_i$	87.0186	311.35	28.4995	19.6812	16.0882	0.441475

The component-wise deviation from the nominal trajectory and 3σ bounds provided by the orbit improvement step are given in Table 6.7. The deviations provided

by the in-house solver are smaller than those of the Astrometry.net solver for all components excluding z position. Accordingly, the 3σ bounds for the Astrometry.net are larger, expressing less certainty in the estimated state. The certainty in the solution produced using the Astrometry.net plate solver is lower than that of the in-house plate solver for two reasons. The first is that Astrometry.net was not able to solve as many images, and as a result the solution includes less measurements. The inclusion of additional precise measurements allows the least squares procedure to become more confident in the estimate. This was demonstrated in the simulated observation scenario in Section 2.6. The second reason is that the measurements that were produced by the Astrometry.net plate solver were noisier. The residuals produced after 10 iterations of the nonlinear least squares procedure are shown in Figures 6.13 and 6.14. Both were run for the same number of iterations, and the residuals produced by the Astrometry.net measurements were significantly larger. This is indicative of the fact that the measurements provided are not as well fit to the two-body propagation solution.

The deviations from the nominal trajectory produced by the processing pipeline using the in-house plate solver are significantly smaller than those produced by the propagated TLE. The overall position deviation produced by the processing pipeline estimate is approximately 30.887 km, while the overall position deviation produced by the propagated TLE is approximately 198.65 km. This makes the position deviation produced by the processing pipeline 15.5% the scale of the TLE overall position deviation. This is also true for the overall velocity deviations, as the overall deviation produced by the processing pipeline is 1.7615 m/s compared to the TLE deviation of 16.094 m/s. The deviation produced by the processing pipeline is 10.9% the size of the propagated TLE velocity deviation. As stated in the beginning of the section, the satellite is not actually in the nominal position, but conducts station keeping maneuvers to ensure it maintains a state withing the proximity of the nominal position.

To provide additional insight, the estimated states from the processing pipeline and TLE propagated state can be expressed in the same terms as the nominal ori-

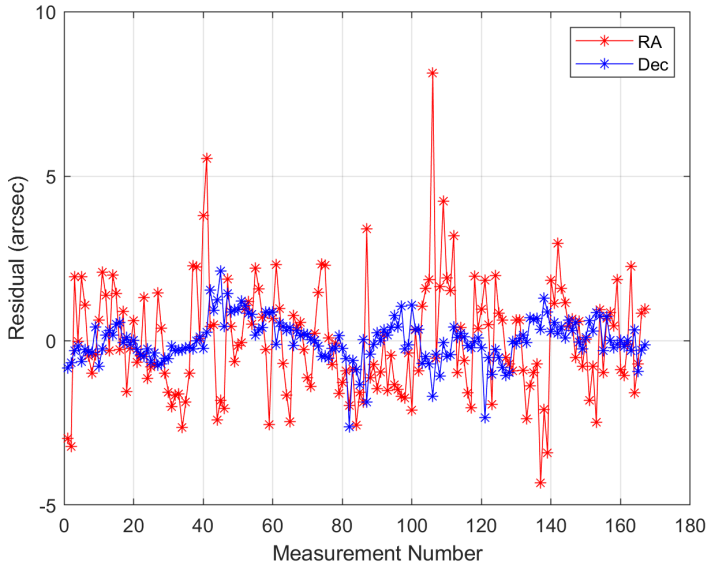

Figure 6.13.. Residuals after 10 iterations of nonlinear least squares orbit improvement using measurements from the in-house plate solver.

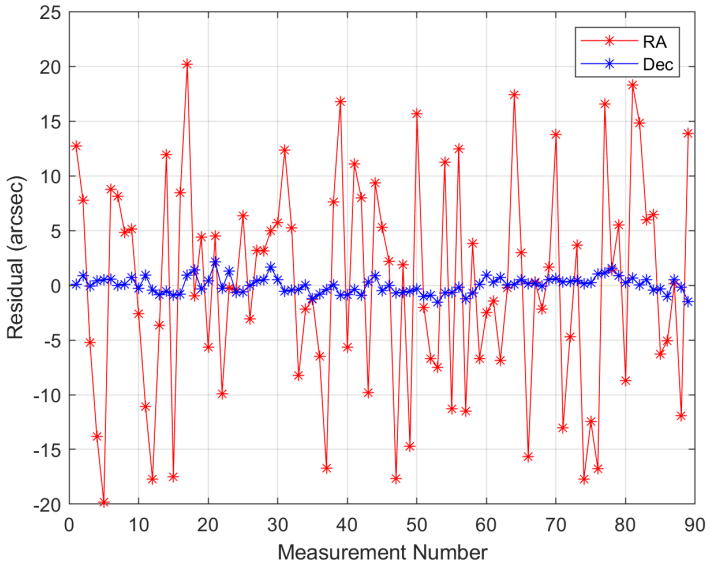

Figure 6.14.. Residuals after 10 iterations of nonlinear least squares orbit improvement using measurements from the Astrometry.net plate solver.

entation. Given some state estimate ($\hat{x} = [\hat{r}\ \ \hat{v}]$), the orbital inclination (i) and longitudinal orientation (λ) can be computed:

$$\vec{h} = \Big(\boldsymbol{\Pi}(t)\boldsymbol{\Theta}(t)\boldsymbol{N}(t)\boldsymbol{P}(t)\Big)\Big(\hat{r} \times \hat{v}\Big) \tag{6.14}$$

$$i = \cos^{-1}\left(\frac{h_z}{|\vec{h}|}\right) \tag{6.15}$$

$$\hat{r}_{ECEF} = \Big(\boldsymbol{\Pi}(t)\boldsymbol{\Theta}(t)\boldsymbol{N}(t)\boldsymbol{P}(t)\Big)\hat{r} \tag{6.16}$$

$$= |\hat{r}| \begin{bmatrix} \cos(\lambda)\cos(\varphi) \\ \sin(\lambda)\cos(\varphi) \\ \sin(\varphi) \end{bmatrix} \tag{6.17}$$

where $\vec{h}$ is the specific angular momentum vector transformed into ECEF, and φ is the latitude orientation of the satellite. The reason $\vec{h}$ is converted to ECEF is to ensure that the inclination is measured with respect to the apparent equator, and not the mean equator. Additionally the orbital period and eccentricity can be calculated using some of the basic developments from Chapter 2.

Table 6.8.. Orbital period, eccentricity, inclination, and longitudinal orientation provided by the TLE propagated state and processing pipeline results. Nominal values for Amazonas 3 are provided for comparison.

		Longitude (deg W)	Inclination (deg)	Period (Hrs)	Eccentricity
Nominal		61	0	23.9344	0
TLE		60.7338	0.143113	23.9353	0.000288323
In-House Plate Solver	Measurement IOD	60.9702	0.0552043	24.0652	0.00367094
	Measurement Orbit Improvement	60.9945	0.0369205	23.9808	0.000731222
Astrometry.net Plate Solver	Measurement IOD	61.0046	0.0397391	22.8449	0.0251454
	Measurement Orbit Improvement	61.0114	0.0364158	23.5664	0.00828557

Table 6.9.. Offset of estimated period, eccentricity, inclination, and longitude orientation from nominal values for the propagated TLE and processing pipeline result.

		Longitude Deviation (arcmin)	Inclination Deviation (arcmin)	Period Deviation (minutes)	Eccentricity Deviation
TLE		-15.9717	8.58676	0.050799	0.000288
In-House Plate Solver	Measurement IOD	-1.78509	3.31226	7.84786	0.003671
	Measurement Orbit Improvement	-0.32834	2.21523	2.78072	0.000731
Astrometry.net Plate Solver	Measurement IOD	0.277438	2.38434	-65.3716	0.025145
	Measurement Orbit Improvement	0.681363	2.18495	-22.0839	0.008286

Table 6.8 shows the nominal parameters of interest for Amazonas 3, as well as the values computed using the TLE propagated state and the state estimate produced by the processing pipeline. The offset from nominal for each of these parameters is presented in Table 6.9. For both plate solvers, the parameters produced by the orbit improvement step are closer to the nominal values than the IOD solution, with the exception of longitude in the Astrometry.net improvement. For all parameters, the in-house plate solver out performs the result produced using the Astrometry.net solver, excluding inclination which is only marginally further off nominal. The processing pipeline produces a result with less deviation from the nominal longitudinal position and inclination than that of the TLE propagated solution. The longitudinal position is dependent on right ascension, and it is not surprising that the offset in predicted longitude using the TLE (0.2662°) is very close to the observed offset in right ascension measurements in Figure 6.11. This would indicate that the solution for right ascension produced by the processing pipeline for this set of observations is more accurate than the TLE result. The results in longitudinal (East-West) and inclination (North-South) deviation are less than the tolerance indicated by the FCC guidelines for

satellite operation in this GEO slot. The deviations produced by the TLE solution are both larger. If the Amazonas 3 satellite is adhering to the station-keeping guidelines outlined by the FCC, than the TLE solution cannot be accurate, while the processing pipeline solution is acceptable.

The period produced by the TLE solution is accurate to within a few seconds of the expected GEO period, while the solution produced by the processing pipeline is approximately 2 minutes and 47 seconds off. Period is a function of semi-major axis, which is dependent on the range estimate produced by the processing pipeline. Acquiring an accurate range estimate is one of the major challenges when working with optical observations, as range is not directly observed as it is with radar. The line of sight produced using the initial position estimate provided by the processing pipeline is given as:

$$\hat{l}_0 = \begin{bmatrix} -0.26778 & 0.95937 & -0.08890 \end{bmatrix}^T. \tag{6.18}$$

The line of sight is directed predominantly along the y-axis. The 3σ bounds provided in Table 6.7 show that the position uncertainty is stretched along the y-axis. This shows that the bulk of position uncertainty is contained along the range direction, which directly translates into uncertainty in semi-major axis: the dependent variable for orbital period. For this reason, the small relative error in period produced by the processing pipeline is reflected in the provided covariance matrix. The representative 3σ bounds can be expected to shrink with the inclusion of more precise measurements. Provided the deviations remain in the 3σ bounds, an improved estimate of orbital period can likely be produced with the inclusion of additional measurements.

Overall, the results produced by the processing pipeline when using the in-house plate solver instead of the Astrometry.net plate solver are superior. The in-house plate solver has a higher rate of success and all available evidence suggests that the measurements produced are of improved accuracy. The propagated TLE state and processing pipeline results have been compared to the nominal Amazonas 3 orbit as a means of assessment. The station-keeping criteria provided by the FCC provide a tolerance for longitudinal position and inclination. The estimated state provided by

the processing pipeline is significantly closer to the nominal state of the satellite at the time of initial observation than the propagated TLE state is. Additionally, the propagated TLE state has been shown to produce a value of longitude and inclination that would exceed the associated tolerances. All the available evidence indicates that the estimated state and associated 3σ bounds produced by the processing pipeline provide a better solution than that of the propagated TLE. It is expected that the discrepancy in orbital period produced by the processing pipeline would be improved with the inclusion of additional measurements. This requires additional images be processed before a definitive statement can be made.

7. CONCLUSIONS AND FUTURE WORK

7.1 Conclusions

For Space Situational Awareness it is integral to have independent reliable information. Ground based sensors can be employed to provide this information; however, these require proper processing procedure followed by an orbit determination in order to be made useful for SSA. The developments presented herein have all contributed to the primary goal of this research: to develop a functioning platform to provide accurate satellite tracking information for the purpose of SSA.

The first step in the processing pipeline is is image processing of raw images acquired from the Purdue Optical Ground Station. The background level of these images approximated and used to find pixels that exceed a determined threshold. The object identification step is then run to find close cells of pixels that meet the specified object criteria. Once this is complete the objects can be positioned in the frame and classified as stars or candidate satellites. This information is handed off to the second step of the processing pipeline: plate solving. This step uses observed star positions measured in pixel coordinates to determine the optimal transformation from pixel coordinates to astronomical coordinates. This is done by pattern matching with a star catalog of known accuracy. Once the transformation parameters are determined, the astronomical coordinate of any pixel location can be found. In this way, astronometric measurements of the resident space objects in frame can be acquired. In addition to the software developed for this purpose, a commercially available alternative, Astrometry.net, has been implemented for comparison. These two steps in series are called the data extraction step, which is run for a large batch of images to provide measurements over the observation series. Once an observation series has been processed the final step of orbit determination and improvement can be con-

ducted. This procedure implements the classical Laplace initial orbit determination method followed by the nonlinear least squares improvement. A minimum of three sets of angular measurements are required to conduct this step; ideally more can be provided. This procedure provides the state estimate and associated state estimate covariance matrix of the observed resident space object at the time of initial observation. The performance of this procedure has been demonstrated on two different simulated observation scenarios in the background material.

In order to rigorously assess the performance of the developed procedure, two different test scenarios have been used with observations of two different satellites. The first is a GPS satellite: Navstar 76, selected due to the availability of accurate IGS ephemeris data which is used to evaluate the quality of the determined solution. A total of 300 observations of Navstar 76 were made; a total of 93 of which were used put through the processing pipeline. Out of the 93 images a total of 37 were successfully solved, producing a success rate of approximately 39.8%. This set of images proved to be difficult for the data extraction step due to a relatively low amount of observed bright stars, which resulted in a reduced rate of success for the plate solver. The measurements produced by the data extraction step were compared to measurements generated using the Navstar 76 propagated TLE as well as the IGS ephemeris. The mean deviation of the processing pipeline measurements were found to be approximately 0.515 arcminutes in right ascension and 9.083 arcminutes in declination. The source of this significant and unexpected offset in declination is currently unknown, but a few important observations can be made. The GPS satellites in MEO move at a higher orbital velocity than satellites in GEO, resulting in a higher tracking rate. Because of the orbits 60° inclination, the declination tracking rate is significantly higher than that of GEO observations. It is suspected that the primary source in declination offset is the stellar aberration correction in the star catalog. Because of the high relative velocity in the z-direction, it is expected that the effect on declination would be larger. Further observations need to be conducted before a definitive cause for this offset can be determined. These measurements are

used to provide an orbit solution for the Navstar 76 satellite. The processing pipeline produces a better estimate of satellite position at the time of observation, but the propagated TLE produces a marginally better estimate of satellite velocity.

The second observation series conducted observed the Amazonas 3 satellite, which is in a 61° west geostationary orbit. A total of 174 observations were processed by the data extraction step. For this observation series, both the in-house plate solver and the Astrometry.net plate solver were used. The in-house plate solver provided a 97.7% rate of success for data extraction, while the Astrometry.net plate solver provided a 51.7% rate of success for data extraction. The observation conditions in this observation series were far more favorable for the processing pipeline, as there were several observed bright stars in each image. The measurements extracted were compared to the TLE generated measurements, as well as measurements generated using the satellites nominal position. The in-house plate solver produced measurements with smaller mean deviation than the Astrometry.net plate solver. The processing pipeline produced significantly better results in right ascension and declination than the propagated TLE. These measurements are used in the orbit determination step to produce the estimated object state at the time of initial observation. The processing pipeline using the in-house plate solver produced the solution with the smallest deviations from the nominal position. This inclination and longitudinal position of the state estimate at the time of observation is computed for the TLE solution and both processing pipeline solutions. The solutions produced using either plate solver provide an object position that is within the specified longitudinal and inclination station keeping tolerance defined by the FCC, while the TLE solution does not. Assuming that the satellite is operating according to its contractual obligations, the results produced by the processing pipeline are more accurate.

7.2 Future Work

All of this considered, there is future work that needs to be conducted to produce a truly professional grade data processing pipeline. Primarily, the source of observed declination offset must be determined. Currently, the source and repeatability of this offset is unknown. More observations must be processed before this can be thoroughly assessed. Once this is corrected, a rigorous assessment of the image processing capability would be advantageous. Namely, quantification of the minimum detectable SNR for the image processing step and the resultant expected covariance in centroid position as a function of the determined SNR. These would provide additional insight in both the plate solving procedure and the orbit determination step and would be expected to improve overall system performance. Once these additions are incorporated, thorough observation campaigns of satellites with accurate ephemeris information (such as the GPS satellite used in this work) can be conducted to benchmark the system capability. Lastly, it is the ultimate goal to be able to use this system to track objects of interest to the SSA community. Many of these objects exhibit behavior that can be difficult to model due to the affects of non-conservative perturbations such as solar radiation pressure. Finding a way to incorporate these perturbations into the models being used here is a long term goal that would make the observation and orbit determination of objects that exhibit more complex motion possible.

REFERENCES

[1] J. A. Kennewell and B. Vo. An overview of space situational awareness. In *Proceedings of the 16th International Conference on Information Fusion*, pages 1029–1036, 2013.

[2] Joint Chiefs of Staff. Joint publication 3-14: Space operations, 2018.

[3] United States Strategic Command. Space-Track [Online]. Available: https://www.space-track.org.

[4] Carolin Frueh. *AAE 590 Space Traffic Management [Course Script]*. School of Aeronautics and Astronautics, Purdue University, 2018.

[5] European Space Agency. Space Debris by the Numbers [Online]. Available: https://www.esa.int/Safety_Security/Space_Debris/Space_debris_by_the_numbers.

[6] B Bastida Virgili, JC Dolado, HG Lewis, J Radtke, H Krag, B Revelin, C Cazaux, Camilla Colombo, R Crowther, and M Metz. Risk to space sustainability from large constellations of satellites. *Acta Astronautica*, 126:154–162, 2016.

[7] Jonas Radtke, Christopher Kebschull, and Enrico Stoll. Interactions of the space debris environment with mega constellations—using the example of the oneweb constellation. *Acta Astronautica*, 131:55–68, 2017.

[8] James G Miller. A new sensor allocation algorithm for the space surveillance network. *Military Operations Research*, 12:57–70, 2007.

[9] Bryan D Little and Carolin E Frueh. Space situational awareness sensor tasking: Comparison of machine learning with classical optimization methods. *Journal of Guidance, Control, and Dynamics*, 43(2):262–273, 2020.

[10] Carolin Früh and Thomas Schildknecht. Accuracy of two-line-element data forgeostationary and high-eccentricity orbits. *Journal of Guidance, Control, and Dynamics*, 35(5):1483–1491, 2012.

[11] Max Born and Emil Wolf. *Principles of Optics*. Cambridge University Press, 7th (expanded) edition, 1999.

[12] Steve B Howell. *Handbook of CCD astronomy*. Cambridge University Press, 2nd edition, 2006.

[13] Francois Sanson and Carolin Frueh. Quantifying uncertainties in signal position in non-resolved object images: Application to space object observation. *Advances in Space Research*, 63(8):2436–2454, 2019.

[14] Francois Sanson and Carolin Frueh. Noise quantification in optical observations of resident space objects for probability of detection and likelihood. In *AAS/AIAA Astrodynamic Specialist Conference, Vail, CO*, pages 15–634, 2015.

[15] Jan A Siminski, Oliver Montenbruck, Hauke Fiedler, and Thomas Schildknecht. Short-arc tracklet association for geostationary objects. *Advances in space research*, 53(8):1184–1194, 2014.

[16] T Schildknecht, U Hugentobler, A Verdun, and G Beutler. CCD Algorithms for Space Debris Detection. *ESA Study Final Report*, 1995.

[17] Igor Molotov, Vladimir Agapov, V Titenko, Z Khutorovsky, Yu Burtsev, I Guseva, V Rumyantsev, M Ibrahimov, G Kornienko, A Erofeeva, et al. International scientific optical network for space debris research. *Advances in Space Research*, 41(7):1022–1028, 2008.

[18] Dustin Lang, David W Hogg, Keir Mierle, Michael Blanton, and Sam Roweis. Astrometry.net: Blind astrometric calibration of arbitrary astronomical images. *The Astronomical Journal*, 139(5):1782, 2010.

[19] Richard H Battin. *An Introduction to the Mathematics and Methods of Astrodynamics, Revised Edition*. American Institute of Aeronautics and Astronautics, 1999.

[20] Roger R Bate, Donald D Mueller, Jerry E White, and William W Saylor. *Fundamentals of Astrodynamics*. Courier Dover Publications, 1973.

[21] Kathleen Howell. *AAE 632 Advanced Orbital Mechanics [Course Script]*. School of Aeronautics and Astronautics, Purdue University, 2019.

[22] Oliver Montenbruck and Eberhard Gill. *Satellite Orbits: Models, Methods, and Applications*. Springer-Verlag Berlin Heidelberg, 2000.

[23] Chopo Ma and Martine Feissel. *Definition and realization of the International Celestial Reference System by VLBI astrometry of extragalactic objects*. Central Bureau of IERS, Observatoire de Paris, 1997.

[24] Claude Boucher, Zuheir Altamimi, Patrick Sillard, and Martine Feissel-Vernier. *The ITRF2000*, volume 31. 2004.

[25] JH. Lieske, T. Lederle, W. Fricke, and B. Morando. Expressions for the Precession Quantities Based upon the IAU (1976) System of Astronomical Constants. *Astronomy and Astrophysics*, 58:1–16, 1977.

[26] PK Seidelmann. 1980 IAU theory of Nutation: The Final Report of the IAU Working Group on Nutation. *Celestial Mechanics*, 27(1):79–106, 1982.

[27] John L. Crassidis and John L. Junkins. *Optimal Estimation of Dynamic Systems*. Chapman & Hall/CRC, 2nd edition, 2011.

[28] Bob Schutz, Byron Tapley, and George H Born. *Statistical Orbit Determination*. Elsevier, 2004.

[29] David Vallado, Paul Crawford, Ricahrd Hujsak, and S Kelso. Revisiting spacetrack report #3. In *American Institute of Aeronautics and Astronautics. AIAA Conference Papers*, 2006.

[30] Carolin Früh and Moriba K Jah. Coupled orbit–attitude motion of high area-to-mass ratio (HAMR) objects including efficient self-shadowing. *Acta Astronautica*, 95(1):227–241, 2014.

[31] Tom Kelecy and Moriba Jah. Analysis of orbit prediction sensitivity to thermal emissions acceleration modeling for high area-to-mass ratio (HAMR) objects (preprint). Technical report, 2009.

[32] Siwei Fan and Carolin Frueh. A direct light curve inversion scheme in the presence of measurement noise. *The Journal of the Astronautical Sciences*, pages 1–22, 2019.

[33] Joanna C Hinks, Richard Linares, and John L Crassidis. Attitude observability from light curve measurements. In *AIAA Guidance, Navigation, and Control (GNC) Conference*, page 5005, 2013.

[34] Charles J Wetterer and Moriba Jah. Attitude determination from light curves. *Journal of Guidance, Control, and Dynamics*, 32(5):1648–1651, 2009.

[35] Carolin Früh. *Identification of Space Debris*. PhD thesis, Verlag nicht ermittelbar, 2011.

[36] Floor Van Leeuwen. The hipparcos mission. *Space Science Reviews*, 81(3-4):201–409, 1997.

[37] E Hog, Claus Fabricius, Valeri V Makarov, S Urban, T Corbin, G Wycoff, Ulrich Bastian, Peter Schwekendiek, and A Wicenec. The tycho-2 catalogue of the 2.5 million brightest stars. Technical report, Naval Observatory Washington DC, 2000.

[38] M. A. C. Perryman. *The Hipparcos and Tycho catalogues : Astrometric and Photometric Star Catalogues derived from the ESA Hipparcos Space Astrometry Mission*. ESA Publications Division, Noordwijk, Netherlands, 1997.

[39] Craig L Cole and John L Crassidis. Fast star-pattern recognition using planar triangles. *Journal of Guidance, Control, and Dynamics*, 29(1):64–71, 2006.

[40] Craig L Cole and John L Crassidis. Fast star-pattern recognition using spherical triangles. In *AIAA/AAS Astrodynamics Specialist Conference and Exhibit*, 2004.

[41] The Navigation Center of Excellence. GPS Constellation Status [Online]. Available: https://www.navcen.uscg.gov/?Do=constellationStatus.

[42] International GNSS Service. IGS Products: GPS Satellite Ephemerides / Satellite & Station Clocks [Online]. Available: http://www.igs.org/products.